UNIVERSITY OF CALIFORNIA,
IRVINE

Illuminating Chemical Reactions on the Nanoscale with Density Functional Theory, Enhanced Raman and IR Spectroscopies

DISSERTATION

submitted in partial satisfaction of the requirements
for the degree of

DOCTOR OF PHILOSOPHY

in Materials Science and Engineering

by

Chloe Elizabeth Groome

Dissertation Committee:
Professor Regina Ragan, Chair
Assistant Professor Stacy Copp
Assistant Professor Elizabeth Lee

2023

DEDICATION

This dissertation is dedicated to the memory of my parents, William and Dana Groome, who raised me with so much love and supported my scientific journey from the beginning.

There is so much I wish I could share with you both.

Rest in peace, together.

TABLE OF CONTENTS

LIST OF FIGURES

LIST OF TABLES

ACKNOWLEDGEMENTS

My deepest gratitude to my Ph.D. advisor, Professor Regina Ragan. You have supported me through incredible adversity these past few years and I genuinely would not be here without your guidance. I have learned so much from you.

I would also like to thank my thesis committee members, Professor Stacy Copp and Professor Elizabeth Lee. It has been a pleasure working with you both, especially as you've shaped the direction of my thesis work.

I am also grateful for the collaborations made possible by the UCI MRSEC, of which I am a Junior Research Fellow. It has been an incredible opportunity learning scanning probe spectroscopy and microscopy from my MRSEC co-advisor Professor Kumar Wickramasinghe as well as Professor Maxim Shcherbakov. Being able to seek advice from faculty across campus departments and even across the country in a casual setting is powerful. I'd like to thank my additional MRSEC co-advisor Professor Zhibin Guan, Professor Joe Patterson, Professor Sahar Sharifzadeh, Professor Ruqian Wu, and Professor Allon Hochbaum for their insights and collaborative spirits.

It has been a pleasure and the greatest morale booster to work with my colleagues in the Ragan Group, including Dr. Hong Wei, Peter Santiago, Hector Pascual, Judy Tran, Sebastian Marroquin, Dr. Will Thrift, Dr. Adrian Garcia, and Dr. Chen Wang. I'd also like to especially thank my undergraduate mentee, Huong Ngo, who with Dr. Chen Wang, Professor Ruqian Wu, and Dr. Jie Li made significant contributions to my first published manuscript.

I must thank the powerful forces that make the department run behind the scenes: Amy Ricks, Darryl Mack, Desiree Rios, and Viviana Saadalla.

I feel so lucky to have found such a supportive community in the Materials Science and Engineering Department at UC Irvine.

Across campus, I'd also like to thank Bri McWhorter and Sandra Tsing Loh, who both taught me how to communicate science with a balance of facts and humor. Additionally, I'd like to thank the Graduate Division Counselor, Phong Luong, for his indispensable advice and emotional support through some of the most challenging years of my life. I'm glad that I can finally come to you with good news.

I am so fortunate to have an amazing network of colleagues, family, and friends. To my partner of twelve years, Mark Rupasinghe, I cannot understate how your patient, kind, and infinite support has bolstered me. Your family has treated me like their own daughter and I hope I make them proud.

Lastly, I cannot dismiss the massive intellectual contributions and cuddles from my cat, Mr. Moby. He's the real brains behind all of this.

Chapter 1 of this dissertation is a reprint of the material as it appears in Groome, C.; Ngo, H.; Li, J.; Wang, C.S.; Wu, R.; Ragan, R. "Influence of Magnetic Moment on Single Atom Catalytic Activation Energy Barriers." *Catal. Lett.* **2022,** *152,* 1347-1357, used with permission from Springer Nature. The co-authors listed in this publication are my advisor, Professor Regina Ragan, my undergraduate, Huong Ngo, as well as our collaborators, Professor Ruqian Wu, Dr. Jie Li, and Dr. Chen Wang.

This work used the Extreme Science and Engineering Discovery Environment (XSEDE), which is supported by National Science Foundation Grant No. ACI-1548562. The XSEDE allocation account used for this research was TG-DMR180078. This research was partially supported by the National Science Foundation Materials Research Science and Engineering Center program through the UC Irvine Center for Complex and Active Materials (DMR-2011967). Additional support was provided by the National Science Foundation Graduate Research Fellowship under Grant No. DGE-1839285 and the XSEDE EMPOWER program.

Finally, I am sincerely grateful to the UC Irvine Graduate Division for the financial support provided by the Graduate Dean Recruitment Fellowship, the Nevin Graduate Endowment Fellowship, and the Graduate Division Completion Fellowship.

VITA

Chloe Elizabeth Groome

Education

University of California, Irvine
Ph.D. Materials Science and Engineering 2023
M.S. Materials Science and Engineering 2019

University of California, Los Angeles 2015
B.S. Physics

Research Experience

The Ragan Group at UC Irvine Mar. 2018 – Mar. 2023
Ph.D. Candidate, Advisor: Prof. Regina Ragan
Computational and experimental investigations on fundamental molecular-scale mechanisms for applications in biosensing and catalysis. Utilizing scanning probe and density functional theory techniques to measure and interpret effects of local electronic fields and magnetic moments on chemical reactions in confined, nanoscale geometries.

Lawrence Berkeley National Laboratory Aug. 2015 - Aug. 2016
Research Intern, Molecular Foundry, Mentor: Tracy Mattox
Jan. 2016 – Aug. 2016
Synthesized, characterized, and measured optical properties of lanthanum hexaboride nanoparticles for potential applications as an optically transparent and thermally insulating coating for windows.

Research Intern, National Center for Electron Microscopy, Mentor: Dr. Colin Ophus
Aug. 2015 – Dec. 2015
Implemented an image reconstruction algorithm for transmission electron microscopy tool users to access real-time information and experimental progress.

The Winslow Group at UCLA Feb. 2014 - Jul. 2015
Undergraduate Researcher, PI: Prof. Lindley Winslow
Characterized dark current performance of recovered photomultiplier tubes to assist with new laboratory particle detector. Built signal processing module to recover previously discarded particle detector data to accurately filter undesirable muon events.

UC Davis Micropower Circuits and Systems Group Jun. 2013 - Sep. 2013
Undergraduate Researcher, PI: Prof. Rajeevan Amirtharajah
Characterized spectral efficiency of photovoltaic cell prototypes developed for indoor energy harvesting.

Professional Experience

Intel Oct. 2016 – Sep. 2017
Emulation Test Engineer
Interfaced with and trained many teams within Visual Parallel and Computing Group to shift their workloads from manual to automated execution and further developed universal automation framework.

Northrop Grumman Jul. 2014 - Sep. 2014
College Intern Technical
Developed user-friendly program to create highly customizable 2-D metamaterial patterns for prototype fabrication.

Teaching Experience

MSE 165C Materials Kinetics and Phase Transformations Mar. 2022 – Jun. 2022
Teaching Assistant
Led weekly discussion sections and office hours as sole teaching assistant for undergraduate class of 45 students. Worked closely with course instructor to incorporate open-source computational modeling techniques into homework sets and course curriculum. Responsible for all grading, proctoring weekly quizzes as well as exams.

Guest Lecturer
"Pressure-Induced Phase Transitions in Iron"

ENGRMSE 205 Materials Physics Graduate Course May 2020
Guest Lecturer
"Introduction to Density Functional Theory"

CBEMS 141/241 Nanoscale Materials and Applications Combined Oct. 2019
Undergraduate/Graduate Course
Guest Lecturer
"Introduction to Density Functional Theory", "Applications and Limitations of Density Functional Theory", developed homework questions in collaboration with course instructor.

CBEMS 141/241 Nanoscale Materials and Applications Combined Apr. 2019
Undergraduate/Graduate Course
Guest Lecturer
"Introduction to Nanoscale Modeling"

ENGRMSE 205 Materials Physics Graduate Course Feb. 2019
Guest Lecturer
"Introduction to Tight Binding and Density Functional Theory"

Girls Who Code Oct. 2016 - Mar. 2017
Teacher
Taught and supported weekly after-school coding lessons through a national non-profit at a local public library for middle school aged girls.

Outreach and Leadership Experience

Materials Research Science and Engineering Center (MRSEC) Oct. 2021 – Jun. 2022
Summer Research Experience for Undergraduates (REU)
Undergraduate Student Mentor, Curriculum Development
Developed introductory computational materials science workshop series with hands-on exercises for summer REU students. Mentored female undergraduate student, teaching concepts of atomic force microscopy and spectroscopy over the 8-week program.

Competitive Edge Jul. 2020 – Oct. 2020
Peer Mentor, Writing Reviewer Jul. 2019 – Oct. 2019
Mentored an incoming first-year female graduate student, providing support and advice both before and after she begins the doctoral program. Providing in-depth feedback and critique for a half dozen engineering graduate students from under-represented backgrounds for technical writing grant applications. Both my mentee as well as several other students whose applications I helped prepare won the NSF GRFP or received Honorable Mention.

Brews and Brains Jul. 2019
Speaker
"Leaving Platinum Behind: A Path to Affordable Hydrogen Fuel Cells"
Delivered talk for public outreach event hosted at Crowne Plaza Hotel restaurant to share scientific research with a broad laymen audience.

The Loh Down on Science Apr. 2019 – Apr. 2020
Staff Writer
Summarized recent scientific discoveries with a humorous, light-hearted tone for the public through a nationally syndicated radio science program with over 4 million listeners.
(https://www.lohdownonscience.com/author/cgroome/)

The Ragan Group at UC Irvine Jan. 2019 – Jun. 2021
Undergraduate Student Mentor
Mentored two female STEM undergraduate students. Trained students in density functional theory to contribute to research and provided career development guidance.

UC Irvine Materials Science and Engineering Department Graduate Student Association Sep. 2017 – Sep. 2020
1st Year Graduate Student Representative, Faculty Representative, Vice President
Led and supported monthly hands-on STEM workshops for high school students at local public library funded by Ceramic and Glass Foundation grant. Voiced graduate student concerns at regular faculty meetings. Facilitated department undergraduate, graduate, and faculty recruitment.

Women in Physical Sciences at UCLA Apr. 2012 - Jun. 2015
Founding Member, President
Fostered positive relationships between physics department female undergraduate students and faculty by planning monthly networking lunches and spearheading inaugural physics department undergraduate research fair. As transitional head of Conference for Undergraduate Women in Physics (CUWiP) committee, fundraised $30,000 and created initial committee structure.

Awards and Honors

Graduate Division Completion Fellowship May 2022

National Science Foundation Extreme Science and Engineering Discovery Environment (NSF XSEDE) Startup Grant Aug. 2021
PI: Chloe Groome
"Combining Machine Learning and Ab Initio Molecular Modelling for A Next-Generation Sensing Platform for Bacterial Metabolomics"

Achievement Rewards for College Scientists (ARCS) Foundation Scholar Award	Oct. 2019
UC Irvine Graduate Student Research Symposium Presentation Winner—Biology, Chemistry, and Medicine	Apr. 2019
Loh Down on Science Writer's Fellowship	Mar. 2019
Nevin Graduate Endowment Fellowship	2020 - 2022
National Science Foundation Graduate Research Fellowships Program (NSF GRFP)	2017 - 2020
UC Irvine Graduate Dean's Recruitment Fellowship	Fall 2017
Society of Women Engineers at UCLA's Scholarship	May 2014

Publications

1. Groome, C.; Pascual, H.; Ragan, R. Illuminating Chemical Reactions in Confined Geometries of Plasmonic Gold Nanoparticles. *In preparation.*

2. Groome, C.; Ngo, H.; Li, J.; Wang, C.S.; Wu, R.; Ragan, R. Influence of Magnetic Moment on Single Atom Catalytic Activation Energy Barriers. *Catal. Lett.* 2022, *152,* 1347-1357.

3. Gabel, M.; O'Callahan, B.T.; Groome, C.; Wang, C.; Ragan, R.; Gu, Y.; El-Khoury, P.Z. Mapping Molecular Adsorption Configurations with <5 nm Spatial Resolution through Ambient Tip-Enhanced Raman Imaging. *J. Phys. Chem. Lett.* 2021, *12,* 3596-3590.

4. Thrift, W. J.; Ronaghi, S.; Samad, M.; Wei, H.; Nguyen, D. G.; Cabuslay, A. S.; Groome, C. E.; Santiago, P. J.; Baldi, P.; Hochbaum, A. I.; Ragan, R. Deep Learning Analysis of Vibrational Spectra of Bacterial Lysate for Rapid Antimicrobial Susceptibility Testing. *ACS Nano.* 2020, *14*, 11, 15336-15348.

5. Mattox, T. M.; Groome, C.; Doran, A.; Beavers, C. M.; Urban, J. J. Chloride influence on the formation of lanthanum hexaboride: An in-situ diffraction study. *Journal of Crystal Growth.* 2018, *486*, 60-65.

6. Mattox, T. M.; Groome, C.; Doran, A.; Beavers, C. M.; Urban, J. J. Anion-mediated negative thermal expansion in lanthanum hexaboride. *Solid State Communications.* 2017, *265,* 47-51.

7. Groome, C.; Roh, I; Mattox, T. M.; Urban, J. J. Effects of Size and Structural Defects on the Vibrational Properties of Lanthanum Hexaboride Nanocrystals. *ACS Omega.* 2017, *2,* 2248-2254.

Presentations

The American Chemical Society (ACS) Fall 2022 Sept. 2022
Speaker
"Tailoring Nanoparticle Surface Chemistry for Selective Interactions with Bacterial Metabolites"

ACS Colloids 2022 Jun. 2022
Speaker
"Tailoring Nanoparticle Surface Chemistry for Chemically Selective Plasmonic Nanogaps"

The Minerals, Metals & Materials Society (TMS) 2022 Annual Meeting Mar. 2022
Speaker
"The Influence of Magnetic Moment on Chemical Activity for Design of Hierarchical Electrochemical Systems"

Materials Research Society (MRS) 2021 Fall Meeting Dec. 2021
Speaker
"The Influence of Magnetic Moment on Chemical Activity for Design of 3D Electrochemical Systems"

MRS 2020 Spring Meeting Dec. 2020
Poster Presenter
Rescheduled due to COVID-19.
"First Principles Investigation of the Influence of Magnetic Moment on Single Atom Earth-Abundant Transition Metal Catalysts for Integrated 3D Graphene Structures"

Electronic Materials Conference (EMC) 2020 Meeting Jun. 2020
Speaker
"First Principles Investigation of the Influence of Magnetic Moment for Design of Integrated 3D Graphene Structures with Earth-Abundant Transition Metal Single Atom Catalysts"

UC Irvine Materials Science and Engineering Department Seminar Apr. 2020
Invited Speaker
"A Materials Discovery Approach to Single Atom Catalysis"

UC Irvine National Fuel Cell Research Center Electrochemistry Day May 2019
Poster Presenter
"Hierarchical Bicontinuous 3D Graphene Structures for Energy Systems"

UC Irvine Graduate Student Research Symposium Apr. 2019
Speaker
"Leaving Platinum Behind: A Path to Affordable Hydrogen Fuel Cells"
Won Biology, Chemistry, and Medicine category, judged by panel of faculty and industry representatives.

ABSTRACT OF THE DISSERTATION

Illuminating Chemical Reactions on the Nanoscale with Density Functional Theory, Enhanced Raman and IR Spectroscopies

by

Chloe Elizabeth Groome

Doctor of Philosophy in Materials Science and Engineering

University of California, Irvine, 2023

Professor Regina Ragan, Chair

Self-assembly typically utilizes thermodynamic driving forces to organize building blocks ranging from atoms to nanoparticles into static assemblies. Self-assembled structures often exhibit unique properties such as lowering catalytic energy barriers or tuning light-matter interactions. This requires understanding how to design and fabricate surfaces at atomic and molecular length scales where localized forces such as magnetic or electric fields drive complex chemical behavior. The characterization of nanoscale chemical behavior necessary for complete understanding of these processes is a significant challenge. In terms of catalysis, high throughput density functional theory modeling of a range of earth abundant transition metal atoms (V, Fe, Mo, Ta) supported on two types of graphene surface defects (bare, N-doped) demonstrate relatively lower activation energy barriers for systems with higher spin states at frontier orbitals near the Fermi energy; CO oxidation on Ta and V SAC have decreases in activation barrier energies of 27% and 44%, respectively. Effective Raman and infrared (IR) modeling approaches have been developed to interpret the effects of charge transfer and electric fields on chemical bonding and

molecular orientation in plasmonic nanogaps. Even non-plasmonic enhancement of electric fields on gold surfaces is shown to alter molecular orientation and selectively enhance resonance modes in vibrational force spectra, which correlates to IR spectroscopy. The insights provided by this work further elucidates nanoscale chemical reactions crucial for next generation catalytic design as well as fundamental understanding of dynamic chemical behavior during self-assembly processes.

INTRODUCTION

In the last few decades, innovations in experimental spectroscopic and microscopic techniques along with the meteoric increase in computing power have fueled research into the nanoscale regime. At these length scales, non-reactive metal clusters such as gold begin to exhibit plasmonic and catalytic behavior that is not present in the bulk[1–5]. Gold clusters with sub-nanometer gap spacings show greatly enhanced optical signals in the gap junction.[6] These clusters and atoms must be stabilized on engineered surfaces for their enhanced properties to be of practical use, due to the delicate dependence of nanocluster oligomer gap spacing for plasmon resonance[7–10] and preventing the aggregation of single metal atoms for efficient catalysis[11–16]. Molecular interactions with these engineered nanostructured surfaces have shown promise in applications as wide as single atom catalysis[17–19], biosensing[20–23], and optoelectronics[24–28]. Understanding the energy transfer processes between molecules and nanostructures that give rise to desirable macroscale surface properties is crucial both to optimize performance and further develop fundamental understanding. We will use experimental and computational techniques in concert to investigate energy transfer processes between molecules and nanostructured surfaces and dynamic chemical behavior. Briefly, these include 1) direct electronic/spin transfer between single metal atoms and nitrogen functional groups on defected graphene surfaces for catalysis, 2) energy transfer between cross-linking molecules and plasmonic hotspots of colloidally assembled gold nanoantenna surfaces for biosensing, and 3) non-resonant near field optical hotspots of gold tip-substrate junctions, which will all be discussed in further detail.

To begin, we will discuss the first project centering on single atom catalysis. Currently, the expense of platinum catalysts represents a major economic roadblock to the adoption of hydrogen fuel cell technology for personal automobiles[29–31]. The Pt metal loading for an H_2/O_2 fuel cell is typically 10 times higher than the amount present in a catalytic converter in a typical car that runs on fossil fuels[11]. Single atom catalysis has been heavily studied to minimize the amount of catalyst material while simultaneously maximizing catalytic performance. Only surface atoms significantly contribute to catalysis, thus single atom catalysis is the most efficient possible use of catalyst material[11,32,33]. Single atom Pt increased catalytic mass activity by more than 5 times compared to Pt clusters and 30 times more compared to state-of-the-art Pt/C catalysts for the hydrogen evolution reaction[34]. Indeed, single transition metal atoms often have dramatically different reactivities compared to bulk metal surfaces[35]--gold in bulk metal is very unreactive, while single gold atoms have been demonstrated to be catalytically active[36]. Similarly, single atoms of iron, cobalt, and nickel have matched or exceeded the performance of state-of-the-art Pt/C catalysts, with more positive onset potentials and higher current densities[12,13,37]. As we demonstrated in our previous work for Pt[14], to prevent aggregation and hence degradation of their catalytic performance, it is necessary to stabilize single metal atoms on defected surfaces[15,38–42]. Defected graphene surfaces have been broadly studied as a support for single atom catalysis[12–14,32,34,37,43,44]. Recent work has demonstrated the ability to produce high surface area graphene on porous 3-dimensional scaffolds, ideal as a catalytic support[45]. Tailoring the surface defect with non-carbonaceous functional groups can further enhance catalytic activity of the coordinated single metal atom by altering the electronic and spin transfer of the stabilized single atom[16,46–51]. Our work focuses on the

pyridinic N functional group, which is characterized as having two C bonds and one non-bonding electron pair. Pyridinic N is a p-type doping site[52,53] and can be selectively grown on graphene via CVD[54]. This electronegative defect will cause coordinated metal adatoms to be positively charged and induce additional local magnetic behavior from unpaired electrons, which has been suggested to be relevant for catalysis[55]. To this end, we investigate the electronic and spin transfer of single atoms of a broader range of elements (V, Fe, Mo, and Ta) coordinated to bare C and pyridinic N functional groups with density functional theory. We have already determined that spin plays a direct role in catalysis for these elements and anticipate additional work expanding the number of pyridinic N functional groups to further isolate the effect of spin. Preliminary results of this project will be discussed further.

Surface Enhanced Raman Scattering (SERS) can achieve up to billion-fold increases in Raman signal intensity by coupling with the optically excited conduction electrons (plasmons) of metallic nanostructures[5]. The extremely low limits of detection that SERS is capable of makes SERS an ideal sensing technique for biomedical applications[4,56–58], which has been demonstrated for the detection and classification of RNA[59,60], bacteria and viruses[21,61,62], as well as cancerous cells[20,63,64]. Diagnostic tools based on SERS need the ability to distinguish multiple analytes in complex biological samples. Recent work analyzing the vibrational modes of cobalt-tetraphenylporphyrin (Co-TPP) with Tip Enhanced Raman Scattering (TERS) demonstrated the sensitivity of Raman spectral features on the molecular orientation of Co-TPP in the nanogap, the local geometry of the nanogap itself, and the dominance of quadrupolar scattering in extreme confinement of the nanogap[65,66]. All of these factors have significant effects on the tensorial electric fields of the

nanogap that ultimately determine Raman spectra. By mapping how various crosslinking molecules in plasmonic nanogaps perturb these complicated confined electric fields, we can develop multiplexed SERS sensors for multianalyte media. We have previously demonstrated a SERS substrate with consistent enhancement factors of 10^9 over large mm^2 areas[8]. This biosensor was fabricated by crosslinking gold nanoparticles into 2-dimensional arrays of gold nanoantenna oligomers with consistent nanogap spacings <1 nm thanks to an anhydride crosslinking molecule. The anhydride crosslinker chemistry bridging the hotspot between these gold oligomers can be further modified to have different functional groups to attract specific analytes[10,67–69]. By combining SERS substrates with different crosslinkers with sensitivity to unique analytes, our SERS platform will be capable of multiplexed sensing of realistic biological samples. Varying the nanogap chemistry and investigating the changes on the nanogap tensorial electric fields will provide deeper insight into Raman spectral features.

Outside of sensing applications enabled by SERS, the manipulation of optical signals far below limits of diffraction made possible by nanoscale and even sub-nanoscale confined geometries has been of (ironically) enormous interest for optoelectronic applications,[70] photocatalysis,[71,72] and fundamental studies of light-matter interactions. Efforts to probe chemical behavior spectroscopically in such regions are challenging due to the sensitivity between molecular orientation, charge transfer, and electromagnetic fields in confined geometries leading to complex variations in vibrational spectroscopic signals.[65] Synergistic experimental and first principles computational approaches are necessary to provide understanding of the dynamic responses of chemical reactions in confined geometries. We intend to investigate the effects of charge transfer, electromagnetic fields, and molecular

orientation with photo-induced force microscopy (PiFM) along with density functional theory (DFT). This recently developed atomic force microscopy technique detects mechanical deflections arising from dipole-dipole interactions between an optically driven molecule and its mirror image dipole in the gold coated AFM tip.[73] At the junction of the Au tip and the Au sample surface, electromagnetic fields are enhanced by factors between 50 and 130 due to the lightning rod effect and multireflection process, neither of which are plasmonic in nature.[74,75] By utilizing both near-field excitation and near-field detection, PiFM is not susceptible to far-field background.[76] Additionally, PiFM is capable of simultaneously measuring topography and chemical signals with a spatial resolution below 6 nm on time scales of seconds[77] and interfacial detection of self-assembled monolayers on gold surfaces.[75] We will demonstrate experimental PiFM measurements compared with density functional theory modeling of benzenedithiol (BDT) attached to a gold surface to ascertain the influence of molecular orientation and the local electromagnetic environment on PiFM force spectra.

REFERENCES

(1) Liu, Z.-P.; Hu, P.; Alavi, A. Catalytic Role of Gold in Gold-Based Catalysts: A Density Functional Theory Study on the CO Oxidation on Gold. *J. Am. Chem. Soc.* **2002**, *124* (49), 14770–14779. https://doi.org/10.1021/ja0205885.

(2) Ma, Z.; Dai, S. Design of Novel Structured Gold Nanocatalysts. *ACS Catal.* **2011**, *1* (7), 805–818. https://doi.org/10.1021/cs200100w.

(3) Chen, M. S.; Goodman, D. W. The Structure of Catalytically Active Gold on Titania. *Science* **2004**, *306* (5694), 252–255. https://doi.org/10.1126/science.1102420.

(4) Schlücker, S. SERS Microscopy: Nanoparticle Probes and Biomedical Applications. *ChemPhysChem* **2009**, *10* (9–10), 1344–1354. https://doi.org/10.1002/cphc.200900119.

(5) Nam, J.-M.; Oh, J.-W.; Lee, H.; Suh, Y. D. Plasmonic Nanogap-Enhanced Raman Scattering with Nanoparticles. *Acc. Chem. Res.* **2016**, *49* (12), 2746–2755. https://doi.org/10.1021/acs.accounts.6b00409.

(6) Esteban, R.; Borisov, A. G.; Nordlander, P.; Aizpurua, J. Bridging Quantum and Classical Plasmonics with a Quantum-Corrected Model. *Nat Commun* **2012**, *3* (1), 825. https://doi.org/10.1038/ncomms1806.

(7) Lee, H.; Nam, S. H.; Jung, Y. J.; Park, S.; Kim, J.-M.; Suh, Y. D.; Lim, D.-K. DNA-Mediated Control of Au Shell Nanostructure and Controlled Intra-Nanogap for a Highly Sensitive and Broad Plasmonic Response Range. *J. Mater. Chem. C* **2015**, *3* (41), 10728–10733. https://doi.org/10.1039/C5TC01915J.

(8) Thrift, W. J.; Nguyen, C. Q.; Darvishzadeh-Varcheie, M.; Zare, S.; Sharac, N.; Sanderson, R. N.; Dupper, T. J.; Hochbaum, A. I.; Capolino, F.; Abdolhosseini Qomi, M. J.; Ragan, R. Driving Chemical Reactions in Plasmonic Nanogaps with Electrohydrodynamic Flow. *ACS Nano* **2017**, *11* (11), 11317–11329. https://doi.org/10.1021/acsnano.7b05815.

(9) Lim, D.-K.; Jeon, K.-S.; Hwang, J.-H.; Kim, H.; Kwon, S.; Suh, Y. D.; Nam, J.-M. Highly Uniform and Reproducible Surface-Enhanced Raman Scattering from DNA-Tailorable Nanoparticles with 1-Nm Interior Gap. *Nature Nanotech* **2011**, *6* (7), 452–460. https://doi.org/10.1038/nnano.2011.79.

(10) Guarrotxena, N.; Ren, Y.; Mikhailovsky, A. Raman Response of Dithiolated Nanoparticle Linkers. *Langmuir* **2011**, *27* (1), 347–351. https://doi.org/10.1021/la103114b.

(11) Rivera-Cárcamo, C.; Serp, P. Single Atom Catalysts on Carbon-Based Materials. *ChemCatChem* **2018**, *10* (22), 5058–5091. https://doi.org/10.1002/cctc.201801174.

(12) Chen, Y.; Ji, S.; Wang, Y.; Dong, J.; Chen, W.; Li, Z.; Shen, R.; Zheng, L.; Zhuang, Z.; Wang, D.; Li, Y. Isolated Single Iron Atoms Anchored on N-Doped Porous Carbon as an Efficient Electrocatalyst for the Oxygen Reduction Reaction. *Angewandte Chemie International Edition* **2017**, *56* (24), 6937–6941. https://doi.org/10.1002/anie.201702473.

(13) Yin, P.; Yao, T.; Wu, Y.; Zheng, L.; Lin, Y.; Liu, W.; Ju, H.; Zhu, J.; Hong, X.; Deng, Z.; Zhou, G.; Wei, S.; Li, Y. Single Cobalt Atoms with Precise N-Coordination as Superior Oxygen Reduction Reaction Catalysts. *Angewandte Chemie International Edition* **2016**, *55* (36), 10800–10805. https://doi.org/10.1002/anie.201604802.

(14) Wang, C. S.; Wang, H.; Wu, R.; Ragan, R. Evaluating the Stability of Single-Atom Catalysts with High Chemical Activity. *J. Phys. Chem. C* **2018**, *122* (38), 21919–21926. https://doi.org/10.1021/acs.jpcc.8b06621.

(15) Ghosh, D.; K. Pati, S. Trapping of Gaseous Pollutants on Defective N-Doped Graphene. *Physical Chemistry Chemical Physics* **2017**, *19* (1), 636–643. https://doi.org/10.1039/C6CP06247D.

(16) Robertson, A. W.; Montanari, B.; He, K.; Kim, J.; Allen, C. S.; Wu, Y. A.; Olivier, J.; Neethling, J.; Harrison, N.; Kirkland, A. I.; Warner, J. H. Dynamics of Single Fe Atoms in Graphene Vacancies. *Nano Lett.* **2013**, *13* (4), 1468–1475. https://doi.org/10.1021/nl304495v.

(17) Wang, A.; Li, J.; Zhang, T. Heterogeneous Single-Atom Catalysis. *Nat Rev Chem* **2018**, *2* (6), 65–81. https://doi.org/10.1038/s41570-018-0010-1.

(18) Kim, Y.-T.; Ohshima, K.; Higashimine, K.; Uruga, T.; Takata, M.; Suematsu, H.; Mitani, T. Fine Size Control of Platinum on Carbon Nanotubes: From Single Atoms to Clusters. *Angewandte Chemie* **2006**, *118* (3), 421–425. https://doi.org/10.1002/ange.200501792.

(19) Li, J.-C.; Yang, Z.-Q.; Tang, D.-M.; Zhang, L.; Hou, P.-X.; Zhao, S.-Y.; Liu, C.; Cheng, M.; Li, G.-X.; Zhang, F.; Cheng, H.-M. N-Doped Carbon Nanotubes Containing a High Concentration of Single Iron Atoms for Efficient Oxygen Reduction. *NPG Asia Materials* **2018**, *10* (1), e461. https://doi.org/10.1038/am.2017.212.

(20) Zhu, J.; Zhou, J.; Guo, J.; Cai, W.; Liu, B.; Wang, Z.; Sun, Z. Surface-Enhanced Raman Spectroscopy Investigation on Human Breast Cancer Cells. *Chemistry Central Journal* **2013**, *7* (1), 37. https://doi.org/10.1186/1752-153X-7-37.

(21) Shanmukh, S.; Jones, L.; Driskell, J.; Zhao, Y.; Dluhy, R.; Tripp, R. A. Rapid and Sensitive Detection of Respiratory Virus Molecular Signatures Using a Silver Nanorod Array SERS Substrate. *Nano Lett.* **2006**, *6* (11), 2630–2636. https://doi.org/10.1021/nl061666f.

(22) Nguyen, C. Q.; Thrift, W. J.; Bhattacharjee, A.; Ranjbar, S.; Gallagher, T.; Darvishzadeh-Varcheie, M.; Sanderson, R. N.; Capolino, F.; Whiteson, K.; Baldi, P.; Hochbaum, A. I.; Ragan, R. Longitudinal Monitoring of Biofilm Formation via Robust Surface-Enhanced Raman Scattering Quantification of Pseudomonas Aeruginosa-Produced Metabolites. *ACS Appl. Mater. Interfaces* **2018**, *10* (15), 12364–12373. https://doi.org/10.1021/acsami.7b18592.

(23) Thrift, W. J.; Cabuslay, A.; Laird, A. B.; Ranjbar, S.; Hochbaum, A. I.; Ragan, R. Surface-Enhanced Raman Scattering-Based Odor Compass: Locating Multiple Chemical Sources and Pathogens. *ACS Sens.* **2019**, *4* (9), 2311–2319. https://doi.org/10.1021/acssensors.9b00809.

(24) Darvishzadeh-Varcheie, M.; Thrift, W. J.; Kamandi, M.; Ragan, R.; Capolino, F. Two-Scale Structure for Giant Field Enhancement: Combination of Rayleigh Anomaly and Colloidal Plasmonic Resonance. *Phys. Rev. Applied* **2019**, *11* (5), 054057. https://doi.org/10.1103/PhysRevApplied.11.054057.

(25) Eizner, E.; Avayu, O.; Ditcovski, R.; Ellenbogen, T. Aluminum Nanoantenna Complexes for Strong Coupling between Excitons and Localized Surface Plasmons. *Nano Lett.* **2015**, *15* (9), 6215–6221. https://doi.org/10.1021/acs.nanolett.5b02584.

(26) Kang, E. S. H.; Shiran Chaharsoughi, M.; Rossi, S.; Jonsson, M. P. Hybrid Plasmonic Metasurfaces. *Journal of Applied Physics* **2019**, *126* (14), 140901. https://doi.org/10.1063/1.5116885.

(27) Sorger, V. J.; Oulton, R. F.; Ma, R.-M.; Zhang, X. Toward Integrated Plasmonic Circuits. *MRS Bulletin* **2012**, *37* (8), 728–738. https://doi.org/10.1557/mrs.2012.170.

(28) Kang, E. S. H.; Chen, S.; Sardar, S.; Tordera, D.; Armakavicius, N.; Darakchieva, V.; Shegai, T.; Jonsson, M. P. Strong Plasmon–Exciton Coupling with Directional Absorption Features in Optically Thin Hybrid Nanohole Metasurfaces. *ACS Photonics* **2018**, *5* (10), 4046–4055. https://doi.org/10.1021/acsphotonics.8b00679.

(29) Bai, J.; Zhu, Q.; Lv, Z.; Dong, H.; Yu, J.; Dong, L. Nitrogen-Doped Graphene as Catalysts and Catalyst Supports for Oxygen Reduction in Both Acidic and Alkaline Solutions. *International Journal of Hydrogen Energy* **2013**, *38* (3), 1413–1418. https://doi.org/10.1016/j.ijhydene.2012.11.039.

(30) Qu, L.; Liu, Y.; Baek, J.-B.; Dai, L. Nitrogen-Doped Graphene as Efficient Metal-Free Electrocatalyst for Oxygen Reduction in Fuel Cells. *ACS Nano* **2010**, *4* (3), 1321–1326. https://doi.org/10.1021/nn901850u.

(31) Gasteiger, H. A.; Kocha, S. S.; Sompalli, B.; Wagner, F. T. Activity Benchmarks and Requirements for Pt, Pt-Alloy, and Non-Pt Oxygen Reduction Catalysts for PEMFCs. *Applied Catalysis B: Environmental* **2005**, *56* (1), 9–35. https://doi.org/10.1016/j.apcatb.2004.06.021.

(32) Tang, Y.; Zhou, J.; Shen, Z.; Chen, W.; Li, C.; Dai, X. High Catalytic Activity for CO Oxidation on Single Fe Atom Stabilized in Graphene Vacancies. *RSC Advances* **2016**, *6* (96), 93985–93996. https://doi.org/10.1039/C6RA14476D.

(33) Yoo, E.; Okata, T.; Akita, T.; Kohyama, M.; Nakamura, J.; Honma, I. Enhanced Electrocatalytic Activity of Pt Subnanoclusters on Graphene Nanosheet Surface. *Nano Lett.* **2009**, *9* (6), 2255–2259. https://doi.org/10.1021/nl900397t.

(34) Cheng, N.; Stambula, S.; Wang, D.; Banis, M. N.; Liu, J.; Riese, A.; Xiao, B.; Li, R.; Sham, T.-K.; Liu, L.-M.; Botton, G. A.; Sun, X. Platinum Single-Atom and Cluster Catalysis of the Hydrogen Evolution Reaction. *Nat Commun* **2016**, *7*. https://doi.org/10.1038/ncomms13638.

(35) Wang, Y.; Mao, J.; Meng, X.; Yu, L.; Deng, D.; Bao, X. Catalysis with Two-Dimensional Materials Confining Single Atoms: Concept, Design, and Applications. *Chem. Rev.* **2018**. https://doi.org/10.1021/acs.chemrev.8b00501.

(36) Lu, Y.-H.; Zhou, M.; Zhang, C.; Feng, Y.-P. Metal-Embedded Graphene: A Possible Catalyst with High Activity. *J. Phys. Chem. C* **2009**, *113* (47), 20156–20160. https://doi.org/10.1021/jp908829m.

(37) Qiu, H.-J.; Ito, Y.; Cong, W.; Tan, Y.; Liu, P.; Hirata, A.; Fujita, T.; Tang, Z.; Chen, M. Nanoporous Graphene with Single-Atom Nickel Dopants: An Efficient and Stable Catalyst for Electrochemical Hydrogen Production. *Angewandte Chemie International Edition* **2015**, *54* (47), 14031–14035. https://doi.org/10.1002/anie.201507381.

(38) Georgakilas, V.; Otyepka, M.; Bourlinos, A. B.; Chandra, V.; Kim, N.; Kemp, K. C.; Hobza, P.; Zboril, R.; Kim, K. S. Functionalization of Graphene: Covalent and Non-Covalent Approaches, Derivatives and Applications. *Chem. Rev.* **2012**, *112* (11), 6156–6214. https://doi.org/10.1021/cr3000412.

(39) Tang, Y.; Yang, Z.; Dai, X. Trapping of Metal Atoms in the Defects on Graphene. *The Journal of Chemical Physics* **2011**, *135* (22), 224704. https://doi.org/10.1063/1.3666849.

(40) Zhang, Y.-H.; Chen, Y.-B.; Zhou, K.-G.; Liu, C.-H.; Zeng, J.; Zhang, H.-L.; Peng, Y. Improving Gas Sensing Properties of Graphene by Introducing Dopants and Defects: A First-Principles Study. *Nanotechnology* **2009**, *20* (18), 185504. https://doi.org/10.1088/0957-4484/20/18/185504.

(41) Dutta, D.; Wood, B. C.; Bhide, S. Y.; Ayappa, K. G.; Narasimhan, S. Enhanced Gas Adsorption on Graphitic Substrates via Defects and Local Curvature: A Density Functional Theory Study. *J. Phys. Chem. C* **2014**, *118* (15), 7741–7750. https://doi.org/10.1021/jp411338a.

(42) Nakada, K.; Ishii, A. Migration of Adatom Adsorption on Graphene Using DFT Calculation. *Solid State Communications* **2011**, *151* (1), 13–16. https://doi.org/10.1016/j.ssc.2010.10.036.

(43) Esrafili, M. D.; Heydari, S. CO Oxidation Catalyzed by a Single Ti Atom Supported on Divacancy Defective Graphene: A Dispersion-Corrected DFT Study. *ChemistrySelect* **2018**, *3* (16), 4471–4479. https://doi.org/10.1002/slct.201800573.

(44) Yang, M.; Wang, L.; Li, M.; Hou, T.; Li, Y. Structural Stability and O2 Dissociation on Nitrogen-Doped Graphene with Transition Metal Atoms Embedded: A First-Principles Study. *AIP Advances* **2015**, *5* (6), 067136. https://doi.org/10.1063/1.4922841.

(45) E. Garcia, A.; Santillan Wang, C.; N. Sanderson, R.; M. McDevitt, K.; Zhang, Y.; Valdevit, L.; R. Mumm, D.; Mohraz, A.; Ragan, R. Scalable Synthesis of Gyroid-Inspired Freestanding Three-Dimensional Graphene Architectures. *Nanoscale Advances* **2019**, *1* (10), 3870–3882. https://doi.org/10.1039/C9NA00358D.

(46) Srivastava, M. K.; Wang, Y.; Kemper, A. F.; Cheng, H.-P. Density Functional Study of Gold and Iron Clusters on Perfect and Defected Graphene. *Phys. Rev. B* **2012**, *85* (16), 165444. https://doi.org/10.1103/PhysRevB.85.165444.

(47) Sun, M.; Tang, W.; Ren, Q.; Zhao, Y.; Wang, S.; Yu, J.; Du, Y.; Hao, Y. Electronic and Magnetic Behaviors of Graphene with 5d Series Transition Metal Atom Substitutions: A

First-Principles Study. *Physica E: Low-dimensional Systems and Nanostructures* **2016**, *80*, 142–148. https://doi.org/10.1016/j.physe.2016.01.026.

(48) Krasheninnikov, A. V.; Lehtinen, P. O.; Foster, A. S.; Pyykkö, P.; Nieminen, R. M. Embedding Transition-Metal Atoms in Graphene: Structure, Bonding, and Magnetism. *Phys. Rev. Lett.* **2009**, *102* (12), 126807. https://doi.org/10.1103/PhysRevLett.102.126807.

(49) Sun, M.; Ren, Q.; Zhao, Y.; Chou, J.-P.; Yu, J.; Tang, W. Electronic and Magnetic Properties of 4d Series Transition Metal Substituted Graphene: A First-Principles Study. *Carbon* **2017**, *120*, 265–273. https://doi.org/10.1016/j.carbon.2017.04.060.

(50) Markevich, A. V.; Baldoni, M.; Warner, J. H.; Kirkland, A. I.; Besley, E. Dynamic Behavior of Single Fe Atoms Embedded in Graphene. *J. Phys. Chem. C* **2016**, *120* (38), 21998–22003. https://doi.org/10.1021/acs.jpcc.6b06554.

(51) Bangert, U.; Zan, R. Electronic Functionalisation of Graphene via External Doping and Dosing. *International Materials Reviews* **2015**, *60* (3), 133–149. https://doi.org/10.1179/1743280414Y.0000000047.

(52) Joucken, F.; Tison, Y.; Lagoute, J.; Dumont, J.; Cabosart, D.; Zheng, B.; Repain, V.; Chacon, C.; Girard, Y.; Botello-Méndez, A. R.; Rousset, S.; Sporken, R.; Charlier, J.-C.; Henrard, L. Localized State and Charge Transfer in Nitrogen-Doped Graphene. *Phys. Rev. B* **2012**, *85* (16), 161408. https://doi.org/10.1103/PhysRevB.85.161408.

(53) Tison, Y.; Lagoute, J.; Repain, V.; Chacon, C.; Girard, Y.; Rousset, S.; Joucken, F.; Sharma, D.; Henrard, L.; Amara, H.; Ghedjatti, A.; Ducastelle, F. Electronic Interaction between Nitrogen Atoms in Doped Graphene. *ACS Nano* **2015**, *9* (1), 670–678. https://doi.org/10.1021/nn506074u.

(54) Ma, C.; Liao, Q.; Sun, H.; Lei, S.; Zheng, Y.; Yin, R.; Zhao, A.; Li, Q.; Wang, B. Tuning the Doping Types in Graphene Sheets by N Monoelement. *Nano Lett.* **2018**, *18* (1), 386–394. https://doi.org/10.1021/acs.nanolett.7b04249.

(55) Zhang, L.; Xia, Z. Mechanisms of Oxygen Reduction Reaction on Nitrogen-Doped Graphene for Fuel Cells. *J. Phys. Chem. C* **2011**, *115* (22), 11170–11176. https://doi.org/10.1021/jp201991j.

(56) Wang, Y.; Yan, B.; Chen, L. SERS Tags: Novel Optical Nanoprobes for Bioanalysis. *Chem. Rev.* **2013**, *113* (3), 1391–1428. https://doi.org/10.1021/cr300120g.

(57) Lane, L. A.; Qian, X.; Nie, S. SERS Nanoparticles in Medicine: From Label-Free Detection to Spectroscopic Tagging. *Chem. Rev.* **2015**, *115* (19), 10489–10529. https://doi.org/10.1021/acs.chemrev.5b00265.

(58) Pilot, R.; Signorini, R.; Durante, C.; Orian, L.; Bhamidipati, M.; Fabris, L. A Review on Surface-Enhanced Raman Scattering. *Biosensors (Basel)* **2019**, *9* (2). https://doi.org/10.3390/bios9020057.

(59) Driskell, J. D.; Seto, A. G.; Jones, L. P.; Jokela, S.; Dluhy, R. A.; Zhao, Y.-P.; Tripp, R. A. Rapid MicroRNA (MiRNA) Detection and Classification via Surface-Enhanced Raman Spectroscopy (SERS). *Biosensors and Bioelectronics* **2008**, *24* (4), 917–922. https://doi.org/10.1016/j.bios.2008.07.060.

(60) Morla-Folch, J.; Xie, H.; Alvarez-Puebla, R. A.; Guerrini, L. Fast Optical Chemical and Structural Classification of RNA. *ACS Nano* **2016**, *10* (2), 2834–2842. https://doi.org/10.1021/acsnano.5b07966.

(61) Efrima, S.; Bronk, B. V. Silver Colloids Impregnating or Coating Bacteria. *J. Phys. Chem. B* **1998**, *102* (31), 5947–5950. https://doi.org/10.1021/jp9813903.

(62) Walter, A.; März, A.; Schumacher, W.; Rösch, P.; Popp, J. Towards a Fast, High Specific and Reliable Discrimination of Bacteria on Strain Level by Means of SERS in a Microfluidic Device. *Lab Chip* **2011**, *11* (6), 1013–1021. https://doi.org/10.1039/C0LC00536C.

(63) Chen, Y.; Chen, G.; Zheng, X.; He, C.; Feng, S.; Chen, Y.; Lin, X.; Chen, R.; Zeng, H. Discrimination of Gastric Cancer from Normal by Serum RNA Based on Surface-Enhanced Raman Spectroscopy (SERS) and Multivariate Analysis. *Medical Physics* **2012**, *39* (9), 5664–5668. https://doi.org/10.1118/1.4747269.

(64) Feng, S.; Chen, R.; Lin, J.; Pan, J.; Wu, Y.; Li, Y.; Chen, J.; Zeng, H. Gastric Cancer Detection Based on Blood Plasma Surface-Enhanced Raman Spectroscopy Excited by Polarized Laser Light. *Biosensors and Bioelectronics* **2011**, *26* (7), 3167–3174. https://doi.org/10.1016/j.bios.2010.12.020.

(65) Lee, J.; Crampton, K. T.; Tallarida, N.; Apkarian, V. A. Visualizing Vibrational Normal Modes of a Single Molecule with Atomically Confined Light. *Nature* **2019**, *568* (7750), 78–82. https://doi.org/10.1038/s41586-019-1059-9.

(66) Lee, J.; Tallarida, N.; Chen, X.; Liu, P.; Jensen, L.; Apkarian, V. A. Tip-Enhanced Raman Spectromicroscopy of Co(II)-Tetraphenylporphyrin on Au(111): Toward the Chemists' Microscope. *ACS Nano* **2017**, *11* (11), 11466–11474. https://doi.org/10.1021/acsnano.7b06183.

(67) Guarrotxena, N.; Bazan, G. C. Antitags: SERS-Encoded Nanoparticle Assemblies That Enable Single-Spot Multiplex Protein Detection. *Advanced Materials* **2014**, *26* (12), 1941–1946. https://doi.org/10.1002/adma.201304107.

(68) Wang, Y.; Wang, Y.; Wang, W.; Sun, K.; Chen, L. Reporter-Embedded SERS Tags from Gold Nanorod Seeds: Selective Immobilization of Reporter Molecules at the Tip of Nanorods. *ACS Appl. Mater. Interfaces* **2016**, *8* (41), 28105–28115. https://doi.org/10.1021/acsami.6b04216.

(69) Le Ru, E. C.; Grand, J.; Sow, I.; Somerville, W. R. C.; Etchegoin, P. G.; Treguer-Delapierre, M.; Charron, G.; Félidj, N.; Lévi, G.; Aubard, J. A Scheme for Detecting Every

Single Target Molecule with Surface-Enhanced Raman Spectroscopy. *Nano Lett.* **2011**, *11* (11), 5013–5019. https://doi.org/10.1021/nl2030344.

(70) Eppenberger, M.; Messner, A.; Bitachon, B. I.; Heni, W.; Blatter, T.; Habegger, P.; Destraz, M.; De Leo, E.; Meier, N.; Del Medico, N.; Hoessbacher, C.; Baeuerle, B.; Leuthold, J. Resonant Plasmonic Micro-Racetrack Modulators with High Bandwidth and High Temperature Tolerance. *Nat. Photon.* **2023**, 1–8. https://doi.org/10.1038/s41566-023-01161-9.

(71) Hu, H.; Weber, T.; Bienek, O.; Wester, A.; Hüttenhofer, L.; Sharp, I. D.; Maier, S. A.; Tittl, A.; Cortés, E. Catalytic Metasurfaces Empowered by Bound States in the Continuum. *ACS Nano* **2022**, *16* (8), 13057–13068. https://doi.org/10.1021/acsnano.2c05680.

(72) Kim, M.; Lin, M.; Son, J.; Xu, H.; Nam, J.-M. Hot-Electron-Mediated Photochemical Reactions: Principles, Recent Advances, and Challenges. *Adv. Opt. Mater.* **2017**, *5* (15), 1700004. https://doi.org/10.1002/adom.201700004.

(73) Rajapaksa, I.; Uenal, K.; Wickramasinghe, H. K. Image Force Microscopy of Molecular Resonance: A Microscope Principle. *Appl. Phys. Lett.* **2010**, *97* (7), 073121. https://doi.org/10.1063/1.3480608.

(74) Roth, R. M.; Panoiu, N. C.; Adams, M. M.; Osgood, R. M.; Neacsu, C. C.; Raschke, M. B. Resonant-Plasmon Field Enhancement from Asymmetrically Illuminated Conical Metallic-Probe Tips. *Opt. Express, OE* **2006**, *14* (7), 2921–2931. https://doi.org/10.1364/OE.14.002921.

(75) Li, J.; Jahng, J.; Pang, J.; Morrison, W.; Li, J.; Lee, E. S.; Xu, J.-J.; Chen, H.-Y.; Xia, X.-H. Tip-Enhanced Infrared Imaging with Sub-10 Nm Resolution and Hypersensitivity. *J. Phys. Chem. Lett.* **2020**, *11* (5), 1697–1701. https://doi.org/10.1021/acs.jpclett.0c00129.

(76) Nowak, D.; Morrison, W.; Wickramasinghe, H. K.; Jahng, J.; Potma, E.; Wan, L.; Ruiz, R.; Albrecht, T. R.; Schmidt, K.; Frommer, J.; Sanders, D. P.; Park, S. Nanoscale Chemical Imaging by Photoinduced Force Microscopy. *Sci. Adv.* **2016**, *2* (3), e1501571. https://doi.org/10.1126/sciadv.1501571.

(77) Almajhadi, M. A.; Uddin, S. M. A.; Wickramasinghe, H. K. Observation of Nanoscale Opto-Mechanical Molecular Damping as the Origin of Spectroscopic Contrast in Photo Induced Force Microscopy. *Nat Commun* **2020**, *11* (1), 5691. https://doi.org/10.1038/s41467-020-19067-3.

CHAPTER 1: INFLUENCE OF MAGNETIC MOMENT ON SINGLE ATOM CATALYTIC ACTIVATION ENERGY BARRIERS

1.1 Introduction

Single atom catalysis is widely studied to minimize the amount of catalyst material while simultaneously maximizing performance. Consider that the expense and scarcity of platinum group metal (PGM) catalysts represents a major economic and manufacturing roadblock to the adoption of fuel cell electric vehicles.[1–3] The PGM loading for a hydrogen fuel cell is typically 10 times higher than the amount present in a catalytic converter. Pt single atom catalysts (SAC) have exhibited increased catalytic mass activity by approximately 37 times when compared to state-of-the-art Pt/C catalysts for the hydrogen evolution reaction.[4] As only surface atoms significantly contribute to performance, SAC is the most efficient possible use of chemically active material[5,6] and hence of enormous economic relevance to a wide range of industrial applications.

Yet the term single atom catalysis may be misleading, because the molecular coordination of a SAC is of crucial consequence to stability and chemical activity.[7–9] Both the presence of coordinating ligands and the support material have been shown to strongly influence catalytic activation energy barriers.[10–13] Many investigations have focused on the role of the relationship between electronic charge transfer and catalytic energy barriers.[12,14–18] Recent work has shown that magnetic moment also plays a role in the catalytic reactivity of O2, which is unusually stable with a triplet ground state.[19] Distinguishing the effects of spin state from more traditionally investigated mechanisms such as charge transfer requires understanding the spin polarized density of states of SAC

environments, which is most readily accessible with a first principles approach. While advances in electron microscopy imaging and spectroscopy through techniques such as monochromated scanning transmission electron microscopy coupled with electron energy loss spectroscopy (STEM-EELS)[20] and electron magnetic circular dichroism (EMCD)[21,22] may enable the correlation of not only local electronic but also magnetic structure with atomic structure, the huge range of stabilizing surface defects and transition metal SAC candidates presents a challenge in terms of throughput. Hence, we present a computational materials discovery approach to identify especially promising SAC candidates. Specifically, we investigate SAC composed of transition metals on two structurally similar graphene defect moieties. The single vacancy has a significant localized magnetic moment, while the pyridinic N defect moiety does not. Our ability to produce high surface area, porous 3-dimensional bicontinuous turbostratic graphene scaffolds, with morphology that facilitates efficient mass transfer as well as simultaneous high electrical conductivity that is important for a catalytic support[23–26] further motivates identification of earth abundant transition metals and fundamental mechanisms in order to inform the design of molecular dopants and adatoms on graphene that optimize catalytic activity.

Chemical reactions undergoing spin inversion have been considered to be spin forbidden or too slow to be practical.[27] Recently, first principles calculations on O_2 dissociation facilitated by gold and silver clusters demonstrated that spin-crossing is more likely when spin states are close in energy. Specifically, clusters with odd and hence, unpaired electrons, exhibited energy barriers that were lower than systems with even number of electrons and this was attributed to spin-crossed pathways.[28] The effect of spin-dependent chemical pathways for transition metal SAC supported on graphene defects has

been examined only recently. Orellana examined spin-constrained, non-equilibrium chemical pathways of O_2 dissociation on transition metal SAC supported on a double vacancy N doped graphene defect and found small energy differences (below 0.1 eV) at points along these pathways increase the probability of spin-crossing during the reaction, enabling lower reaction barriers over spin-conserved reactions.[29] Our work expands this perspective to examine the magnetic moment of the surface defect and the TM and how this affect bonding energy. We then investigate the chemical activity during CO oxidation of four earth abundant TM atoms (V, Fe, Mo, Ta) coordinated with two graphene defect moieties using density functional theory (DFT). Single vacancy and pyridinic N-doped single vacancy defects are two structurally similar graphene defect moieties that have similar charge transfer to metal adatoms but differing magnetic moments. CO oxidation is examined as it has many relevant industrial uses, including catalytic converters in vehicles, smoke stack emission control, and respiration filters.[30]

Climbing image-nudged elastic band (CI-NEB) calculations of activation energy barriers of CO oxidation on all transition metal SAC in relaxed geometries on both defect moieties show all barrier energies on N-doped single vacancy defects were 0.8 eV or less. There were significant decreases in activation barrier energies for V and Ta, no difference in the case of Fe, and a slight increase for Mo when the N dopant was present. Hence, the common understanding of pyridinic N dopants improving catalytic behavior is simplistic. Due to the similar charge transfer calculated for both defect moieties, changes in activation barrier energy values were correlated with differences in bonding arrangements and local magnetic moment. A closer inspection of the density of states of the chemical pathways calculated via CI-NEB shows that lower activation energy barriers are associated with

larger spin state asymmetry near the Fermi level in all cases, and in several cases the change in electronic charge transfer and bonding geometry was similar. Thus, spin state asymmetry provides new avenues for tailoring the molecular environment of promising support structures for SAC and guides choices for further experimental analysis, opening up additional lower energy chemical pathways for catalysis.

1.2 Calculation Details

Spin-polarized density functional theory calculations were implemented with the Vienna *ab initio* simulation package (VASP)[31,32] using the projector augmented wave (PAW) pseudopotentials[33,34] and the generalized gradient approximation of the Perdew, Burke, and Ernzerhof (PBE) exchange-correlation functional,[35] PBE incorporating a Hubbard correction term[36] to account for d electron self-interaction effects (PBE+U), as well as the strongly constrained and appropriately normed (SCAN) meta-generalized gradient approximation (meta-GGA) functional.[37] A Hubbard U of 2.0 eV and an on-site exchange constant of J of 0 eV were applied to the single Ta atom.[38] As the first meta-GGA, SCAN includes the gradient of the kinetic energy density, which satisfies 17 known possible exact constraints and can accurately captures intermediate range weak interactions in non-bonded systems and rare-gas atoms due to appropriate norming.[37] SCAN can often meet or even exceed the performance of more expensive hybrid calculations such as HSE06 (which were computationally intractable for the size of this system, with over 70 atoms) for many material properties.[37,39]

Binding energies, bond lengths, charge transfer, and magnetic moments were calculated for a Ta adatom bound to either a bare single vacancy (N0) or pyridinic N doped single vacancy (N1) graphene substrate with PBE, PBE+U, and SCAN, results listed in Table 1.1. All three functionals capture similar shifts in the Ta binding energy, charge transfer, and magnetic moments across to the N0 and N1 defect moieties. However, the binding energies calculated by PBE are significantly closer in value to those calculated by SCAN than PBE+U. Additionally, the magnetic moments calculated by PBE are overall closer to the SCAN values than those calculated with PBE+U.

Table 1.1. Binding energies, nearest neighbor (NN) bonding lengths, z heights above graphene sheet, net electron transfer from Ta to surrounding graphene substrate, local magnetic moment of Ta, total spin state of Ta adatom bound to graphene substrate with pyridinic N defect calculated with PBE, PBE+U, and SCAN DFT functionals

Defect Moiety	**Functional**	**E_B [eV]**	**$d_{(TM-NN)}$ [Å]**	**Δz [Å]**	**[e^-]**	**[μ_B]**	**[μ_{B-tot}]**
Ta/N0	**PBE**	9.61	1.97	1.88	1.49	0.39	0.80
	PBE+U	8.16	1.99	1.91	1.48	0.55	0.95
	SCAN	10.65	1.94	1.76	1.58	0.39	0.83
Ta/N1	**PBE**	7.44	1.99	1.87	1.45	0.85	1.82
	PBE+U	6.33	1.96	1.87	1.47	0.92	1.84
	SCAN	8.14	1.93	1.87	1.50	0.88	1.84

To further verify the choice of the PBE functional, the total density of states (DOS) for Ta/N0 was calculated with PBE, PBE+U, and SCAN and plotted in Figure 1.1. The PBE and

SCAN DOS plots both show a single spin down peak near the Fermi energy, while the PBE+U DOS shows two small spin down peaks. The DOS calculated with PBE is a closer match to the SCAN DOS than PBE+U. Overall, comparison of the functionals demonstrate that PBE most accurately captured structural, electronic, and magnetic properties of interest for a single Ta atom secured to both graphene surface defect moieties investigated in this work.

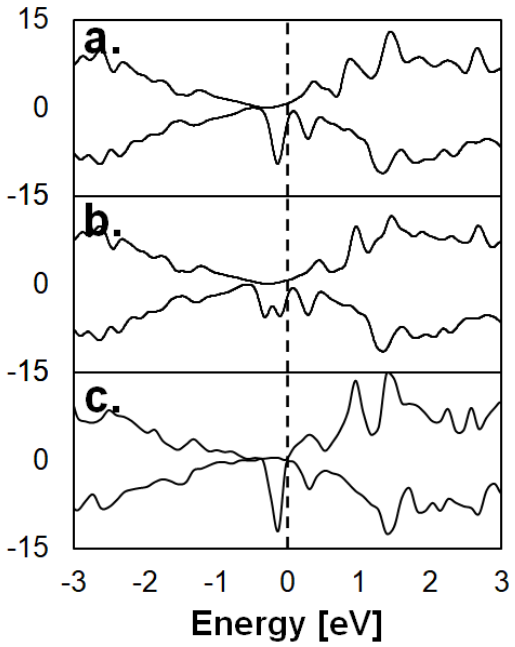

Figure 1.1. Spin polarized total density of states calculated with a) PBE, b) PBE + U, and c) SCAN levels of theory for single atom Ta anchored to a graphene substrate with a pyridinic N doped single vacancy. The Fermi energy is highlighted with a vertical dashed line and set to 0 eV. All positive values correspond to spin up and all negative values are spin down.

The pseudopotential of each transition metal was chosen to represent the largest number of valence electrons for increased accuracy, while still utilizing the frozen core electron approximation for increased computational efficiency. In all calculations, the electron wave functions were expanded with a plane wave cut-off of 400 eV. The graphene

substrates consist of a 6×6 repeating graphene unit cell with a vacuum spacing of 25 Å between repeating images in the z direction. The large unit cell size and vacuum spacing were chosen to minimize spurious interactions between adsorbed adatoms due to the periodic boundary conditions.

For structural relaxations, reciprocal space was sampled with a 5×5×1 gamma centered Monkhorst-Pack grid[40] and a Gaussian smearing of 0.01 eV. Standard convergence testing was performed with the reported cut-off and k point values chosen based on total energy values changing by less than 1 meV. The entire substrate was allowed to relax until the Hellmann-Feynman forces fell beneath 0.025 eV/ Å. The cohesive binding energies (E_B) for each transition metal adatom were calculated via

$$E_B = E_{G\text{-}TM} - E_G - E_{TM} \quad (1)$$

E_G represents the energy of the bare graphene substrate, E_{TM} the energy of the isolated transition metal atom, and $E_{G\text{-}TM}$ the total energy of the transition metal adatom adsorbed to the graphene substrate, each of which have been allowed to relax in identical hexagonal unit cells (14.7 × 14.7 × 25 Å). Charge density difference plots are defined by the following equation

$$\Delta n(r) = n_{G\text{-}TM} - n_G - n_{TM} \quad (2)$$

where n_G represents the charge density of the optimized bare graphene substrate, n_{TM} the charge density of the optimized transition metal adatom, and $n_{G\text{-}TM}$ the charge density of the optimized total system of the transition metal adsorbed adatom to the graphene substrate.

Density of states calculations were performed with 9×9×1 k points and a broader Gaussian smearing of 0.1 eV for visualization. Charge transfer and transition state analysis were carried out with tools from the VASP Transition State Theory (VTST) package. Specifically, charge transfer was calculated with the Bader charge analysis method,[41] as implemented by Henkelman et al.[42] Initial transition states along the minimum energy pathway were identified with the climbing image nudged elastic band method[43] and then further refined with the dimer method.[44] These two methods were also used to investigate spin-constrained reaction pathways of CO oxidation with the spin state specified using the NUPDOWN tag.

1.3 Results and Discussion

1.3.1 Magnetic Properties of Graphene Defects

The two common defect moieties in graphene that are investigated in this work have similar charge transfer to TM and differing magnetic moment,[45,46] as well as reported differences in activity of supported single atom catalysts such as Pt[44] and Fe.[16] These surfaces allow us to examine correlations between magnetic moment and reaction energy barriers. The first defect moiety is the single vacancy (N0) defect; the absence of the single carbon atom in the graphene lattice gives rise to a significant magnetic moment, with a calculated total value of 1.36 μ_B, in agreement with previous reports.[48,49] The magnetization is mostly localized to a neighboring C atom from the vacancy (Figure 1.1, a). The second defect also consists of a single C vacancy with a neighboring N-dopant in a pyridinic configuration (N1). Pyridinic N is a p-type doping site on graphene[50,51]

characterized as having two C bonds and known to contribute one electron to the delocalized graphene π orbitals. The additional electron contributed by the pyridinic N-dopant extinguishes the magnetic moment of the N1 defect moiety (Figure 1.1, b). Additionally, the distance between the two remaining C nearest neighbor atoms shortens from 1.98 Å to 1.79 Å, forming a shorter bond with no magnetic moment.

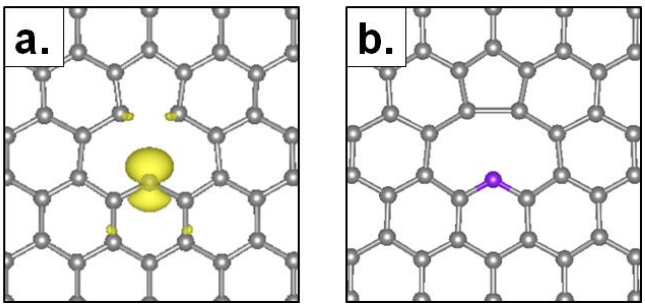

Figure 1.2. Optimized geometry and magnetization density of a) undoped single C vacancy (N0) and b) single C vacancy with pyridinic N dopant (N1) on graphene surfaces. Grey atoms represent C while the purple atom is N. Isosurfaces drawn at a value of 0.01 e/ Å^3 to facilitate comparison with the literature.[48,52] N0 defect moiety has a total magnetic moment of 1.36 μ_B while N1 defect moiety has no magnetic moment.

Binding energies for all four transition metal (TM) atoms (V, Fe, Mo, Ta) on both defects in relaxed geometries are calculated and the electronic and magnetic properties are compared; binding energies, bond lengths, Bader charge transfer, and magnetic moments are summarized in Table 1.2. Pristine graphene is not analyzed, as both our previous work[17] and many examples in the literature have demonstrated that pristine graphene has unsuitably low adsorption and diffusion barrier energies to support single molecules or atoms.[45,53,54]

Table 1.2. Calculated binding energies of TM SAC, TM adatom to nearest neighbor (NN) bonding lengths, z heights above graphene sheet, net electron transfer from TM to surrounding graphene substrate, local magnetic moment of TM, total spin state of system

Defect Moiety		**E_B [eV]**	**$d_{(TM-NN)}$ [Å]**	**Δz [Å]**	**[e^-]**	**[μ_B]**	**[μ_{B-tot}]**
V	**N0**	7.82	1.88	1.63	1.28	1.01	1.01
	N1	6.22	1.89	1.65	1.28	1.61	1.96
Fe	**N0**	7.52	1.76	1.40	0.71	0	0
	N1	5.71	1.76	1.35	0.78	0.63	0.99
Mo	**N0**	7.81	1.95	1.84	1.12	1.53	1.99
	N1	5.46	1.96	1.84	1.11	1.97	2.71
Ta	**N0**	9.61	1.97	1.88	1.49	0.39	0.80
	N1	7.44	1.99	1.87	1.45	0.85	1.82

Previous work on N defect moieties supported on graphene surfaces has associated enhanced catalytic activity due to the N dopants altering O_2 binding energies with values approaching that of O_2 on Pt surfaces.[29,47,55] However, the underlying mechanisms of this shift in binding energy is not completely understood. Here, the addition of the pyridinic N dopant in the N1 defect moiety consistently decreases the binding energy of the TM adatoms by an average value of 1.98 eV. The binding energy is plotted as a function of the

charge transfer between the TM adatom and the surrounding defect, as calculated with Bader charge analysis, and is shown in Figure 1.3, a. There is remarkably little difference in the charge transferred between each TM atom when comparing N0 to N1. For example, charge density difference plots of Ta/N0 and Ta/N1, shown, in Figures 1.3 b and 1.3 c, respectively, electronic charge is transferred from the adsorbed metal adatom to the surrounding graphene substrate and the two surfaces exhibit only minor differences in isosurface symmetry. All metal adatoms investigated become cationic independent of defect moiety. In contrast to the charge transfer, the binding energy and local magnetic moment of the TM adatom both vary on the two defects as observed in Figure 1.3 d. Plots of the total magnetic moment illustrate the strong localization of the magnetic moment while also illustrating the increase in magnetization from the N0 to the N1 defect moiety, and is shown for the case of Ta in Figure 1.3 e and Figure 1.3 f, respectively.

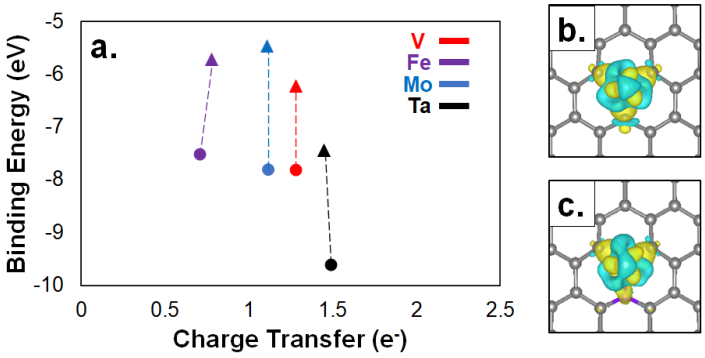

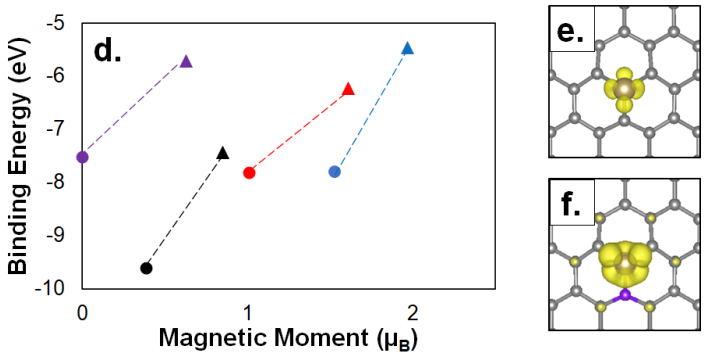

Figure 1.3. The local a) charge transfer and d) magnetic moment plotted against the binding energy of the TM to N0 (circles) and N1 (triangles) defect moieties. Dashed lines are provided as guides for the eye. Charge density difference Δn(r) of b) Ta/N0 and c) Ta/N1. All isosurfaces are drawn at levels of 0.01 e/Å^3. Yellow (blue) isosurfaces correspond to an increase (decrease) in charge density. Magnetization density isosurfaces of e) Ta/N0 and f) Ta/N1. Yellow isosurfaces correspond to spin up electron density. Grey and purple spheres correspond to carbon and nitrogen atoms, respectively.

Charge density difference and magnetization plots for all TM atoms can be found in Figure 1.4 below. With the adsorption of a TM atom the total magnetization of the N1 system increases by an average of 0.92 μ_B, approaching the value of one additional unpaired electron. Thus, these graphene defect moieties allow one to assess the effect of magnetic moment nearly independent from charge transfer. Furthermore, the bonding geometry of metal adatoms on both defect moieties does not significantly change as shown in Table 1.2. The trend of defects with higher magnetic moments inducing stronger binding energies was also identified for Fe and other TM on similar N-doped graphene defects.[29,46] Kattel et al. found that when the final coordinated TM SAC exhibited a magnetic moment, the binding energy became weaker,[56] similar to our results for TM/N1, which have higher magnetic moments in the final state geometry and weaker binding energies. Considering that previous work has correlated the binding energy of O_2 with enhanced catalytic activity,

this suggests that tuning the magnetic moment of an impurity on a defect site provides an additional knob to optimize catalytic performance.

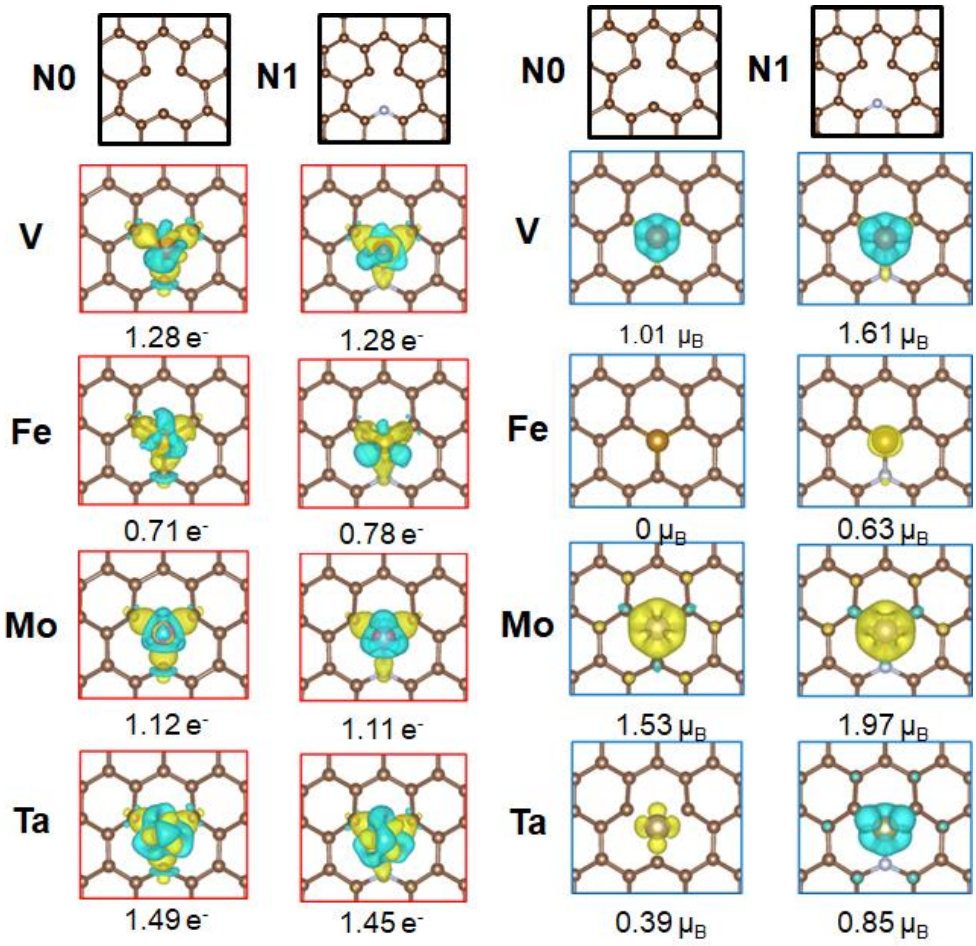

Figure 1.4. Charge density difference (red boxes) with net charge transfer labelled below. Positive values indicate charge transferred to the defect. Magnetization density (blue boxes) with net magnetic moment of metal adatoms. Each adatom is adsorbed on either single vacancy (N0) or pyridinic N-doped single vacancy (N1) defect moieties on graphene substrates. All isosurfaces are drawn at levels of 0.01 e/ Å^3. Yellow (blue) isosurfaces correspond to an increase (decrease) in charge density or spin up (down) charge.

1.3.2 Effect of Magnetic Moment on Gas Adsorption and CO Oxidation

The binding energies of CO, CO_2, and O_2 molecules, involved in CO oxidation, were calculated for both N0 and N1 SAC systems to assess resistance to CO poisoning and elucidate chemical pathways. The binding energy of CO_2 is weak and in some cases positive; the values are shown in Table 1.3. O_2 is always adsorbed more strongly than CO, which is favorable to mitigate CO poisoning of the catalyst[57] on all metal adatoms investigated on both defect moieties. All gas molecule magnetic moment values are tabulated in Table 1.3 as well.

Table 1.3. The proximity of nearest TM d orbital states to the Fermi energy of the TM SAC without gas adsorbates (denoted by $|E_F$ - d orbitals$|$). Binding energies and local magnetic moments of carbon monoxide, oxygen, and carbon dioxide molecules on single metal adatoms on N0 and N1, i.e single vacancy and pyridinic N defects on graphene substrates, respectively

		CO		**O_2**		**CO_2**	
	$\|E_F$ - d orbitals$\|$	**E_B [eV]**	**[μ_B]**	**E_B [eV]**	**[μ_B]**	**E_B [eV]**	**[μ_B]**
V/N0	medium	-0.98	0.11	-3.2	0	-0.11	0
V/N1	small	-1.35	0.17	-2.44	0	-0.49	0
Fe/N0	small	-1.46	0	-2.14	0.62	---	0
Fe/N1	medium	-1.71	0	-2.42	0.43	---	0
Mo/N0	medium	-0.74	0	-3.16	0	---	0
Mo/N1	high	-1.84	0	-3.78	0.15	-0.4	0
Ta/N0	high	-1.2	0.09	-3.75	0	-0.1	0
Ta/N1	high	-1.8	0	-5.07	0	-0.49	0

Figure 1.5a plots the binding energy trends for O_2 and CO and illustrates that gas molecules generally adsorb more strongly to TM SAC coordinated to N1, all of which were

shown to have higher magnetic moments compared to N0 (Table 1.2). This is consistent with data shown in Figure 1.3d where bare N0 has a higher magnetic moment and consequently higher E_B to SAC than bare N1. One notable exception is O_2-V, where the magnetic moment on the O_2-V system is calculated as zero on both defect types. Interestingly, a shift from side-on (Figure 1.5b) for the N0 defect to end-on (Figure 1.5c) for the N1 defect bonding geometry is observed. Here we postulate that the additional unpaired electron contributed by the N1 defect favors the end-on configuration for O_2-V to obtain a ground state with no magnetic moment and lower system energy. Bonding geometry changes have been associated with minimizing magnetic moment to lower system energy in a few other studies.[29,58] This result would explain the weaker binding energy for O_2-V on N1, as the end-on geometry appears to minimize the additional magnetic moment imparted by the N dopant.

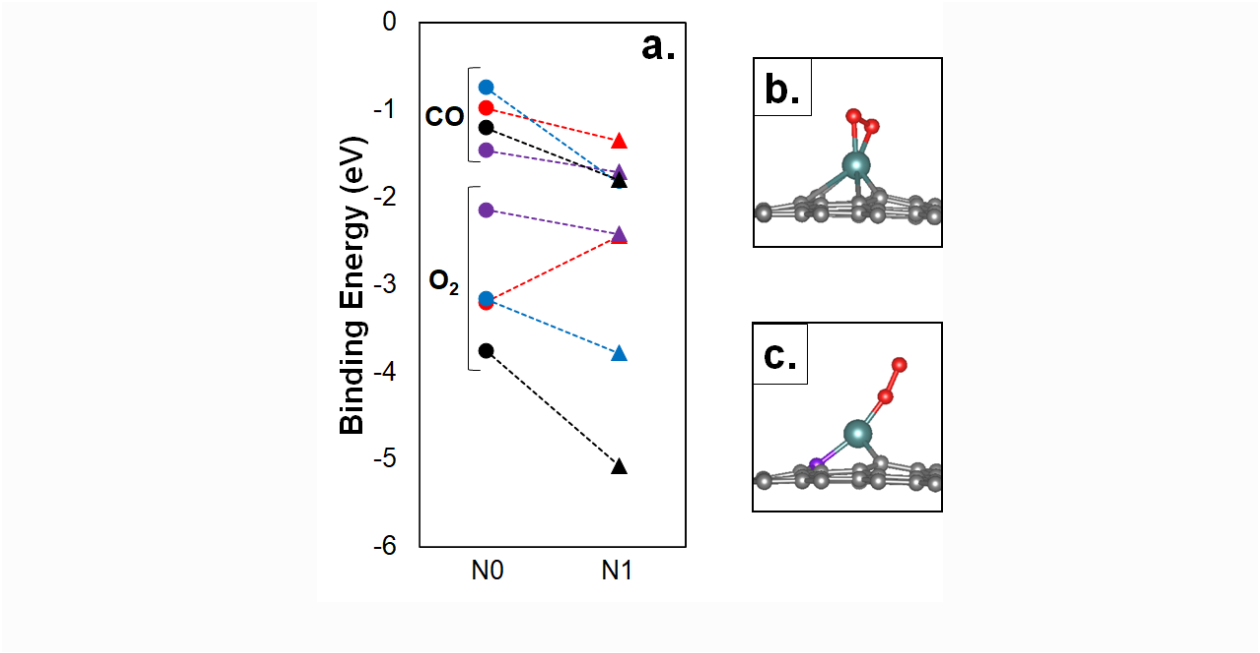

Figure 1.5. a) The binding energy of CO and O_2 adsorbed to each TM on N0 (circles) and N1 (triangles) defect moieties for Fe (purple), V (red), Mo (blue), and Ta (black). Relaxed bonding geometry of O_2 adsorbed to b) V/N0, note the side-on configuration of the linear O_2 molecule, c) V/N1 where the O_2 molecule adsorbs in an end-on configuration. Grey, purple, red, and green spheres correspond to carbon, nitrogen, oxygen, and vanadium atoms, respectively.

The total density of states (DOS) for each TM SAC was also calculated and shown in Figure 1.6. Correlation between gas molecule binding energy with proximity of d-orbitals to the Fermi level was not observed by comparing DOS in Figure 1.6 and calculated binding energy of gas molecules. For example, the DOS of Fe/N0 and V/N1 would predict higher gas binding energies than Fe/N1 and V/N0, respectively, by this criterion. However, both O_2 and CO have higher binding energies on Fe/N1 versus Fe/N0 as shown in Figure 1.5. Similarly, the CO binding energy increases on V/N1 with respect to V/N0, while on the other hand, the O_2 binding energy is much weaker on V/N1. In line with previous work that correlates the binding energy of O_2 to catalytic performance,[47,59,60] we are motivated to examine more closely the effect of binding energy and magnetic moment on CO oxidation barrier energy.

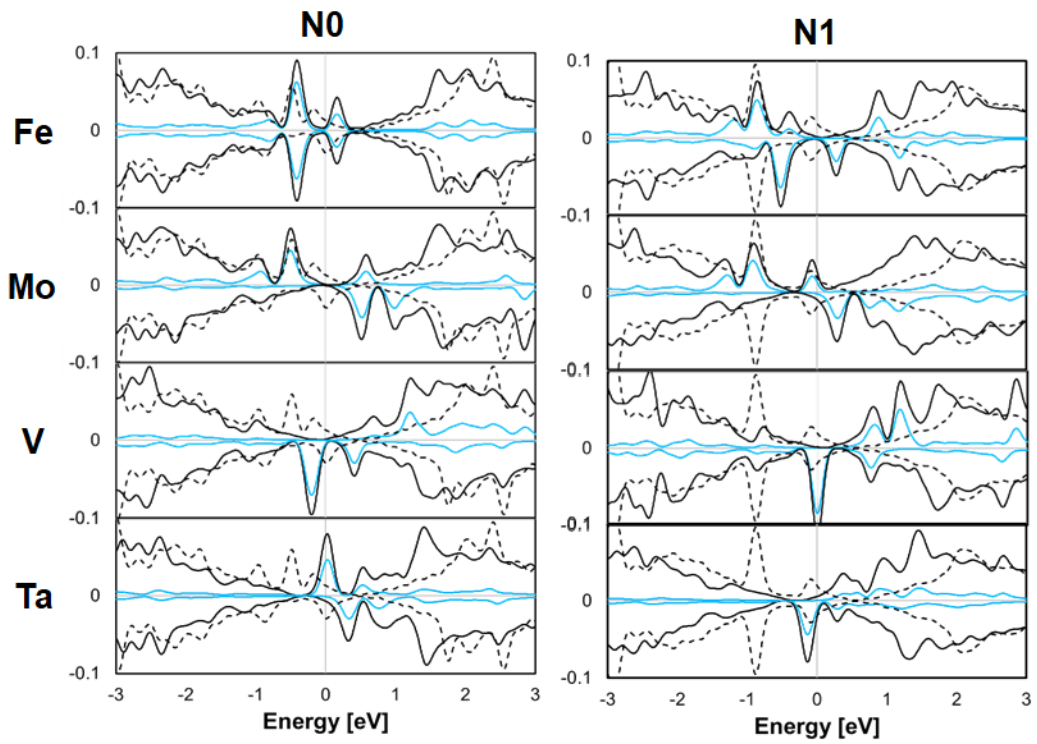

Figure 1.6. Spin polarized density of states for TM SAC. Black dashed curve shows total density of states of pristine defected graphene surface. Black solid curve shows the total density of states of TM SAC supported on each graphene defect moiety. Blue solid curve shows adsorbed transition metal adatom d orbitals. The Fermi levels have been set to 0 eV, indicated with a vertical grey line. All positive values correspond to spin up and all negative values are spin down.

The relatively weaker binding energy of CO versus O_2 in Figure 1.5a suggest that the modified Eley-Rideal reaction[18,61] pathway (wherein CO reacts with adsorbed O_2 to form CO_2 and O) is most appropriate for this system, rather than the Langmuir-Hinshelwood reaction mechanism. Fe/N0 has previously been found to proceed via the modified Eley-Rideal pathway as well.[62] The climbing image nudged elastic band (CI-NEB) method was used to model the modified Eley-Rideal reaction path and calculate the barrier energies without constraining the spin state, typically done in prior studies, for each combination of a TM-SAC and the graphene defect moieties investigated. Previous work investigating spin-

constrained reaction pathways revealed that these pathways are close in energy for TM SACs on graphene defects, increasing the likelihood of spin inversion events between reaction steps that benefit catalytic activity,[29,63] making spin unrestricted calculations more appropriate for these systems.

The calculated barrier energies between the initial state (IS) and transition state (TS), listed in Table 1.4, were under 1 eV and impressively, all barrier energies for N1 were less than 0.8 eV. Generally, reactions below 0.8 eV are considered feasible at room temperature.[64] The energy barrier calculated for Fe/N0 is in agreement with previous reports.[62,63] For all TM SAC on N1, the addition of a pyridinic N dopant appears to favor the formation of a COOO intermediate[65–67] at the transition state, with the exception of Ta. On N0, Fe SAC also forms a similar intermediate and all others do not. Interestingly, as observed in Table 1.1, the Fe SAC barrier energies are the same on both defect moieties despite N doped defects often being attributed to increasing catalytic activity for both Fe[47] and Pt[68] SAC. Overall, for all SAC on N1 and N0 defect moieties, there is no clear trend of the relationship with defect moiety and energy barrier. V and Ta both demonstrated significant decreases in activation barrier energies, Fe had no change, and Mo showed a slight increase in value on N1 with respect to N0. Insight of physical mechanisms behind these trends can be obtained by examining the spin polarized projected density of states (PDOS) of the transition states, shown in Figures 1.7-1.9. We find that the magnetic state of atomic and molecular orbitals near the Fermi level exhibits common features, i.e., asymmetry of spin states, for systems with lowest activation energy barriers. Each TM SAC will be discussed in the following section in turn.

Table 1.4. Activation Barrier Energies of CO Oxidation on Different Defect Moieties

	V	**Fe**	**Mo**	**Ta**
N0	0.98	0.74	0.76	0.91
N1	0.55	0.74	0.83	0.66

The relaxed geometries and energy levels for CO oxidation on Mo on the two defect types are illustrated in Figure 1.7a. The barrier energy is approximately 9% higher on N1 with respect to N0, where values are shown in Table 1.1. We systematically examine physical mechanisms, starting with geometry, charge transfer and induced magnetic moment as past studies clearly indicate geometry and charge transfer play a role and we seek to find cases where only magnetic moment changes. The geometry of O_2 is the same, side-on, for both moieties, illustrated by the insets of Figure 1.7a. Additionally, charge transfer and even magnetic moment of O_2 on Mo/N0 and Mo/N1 TS are very similar, values are shown in Table 1.2. The main observable difference is the PDOS. In Figure 1.7c, Mo/N1 shows spin state asymmetry in the O_2 peaks near the Fermi level, however the spin state splitting of these peaks is more pronounced for Mo/N0 (Figure 1.7b). Additionally, near the Fermi level (within 1 eV), Mo/N1 shows greater overlap between CO, O_2, and Mo 4d orbital peaks, however Mo/N0 retains a slightly lower energy barrier, emphasizing the unique effect of spin split orbitals on reactivity. Spin state splitting of the orbital peaks with the greatest proximity to the Fermi level was also present in the DOS of the best performing Au SAC analyzed in a previous theoretical work.[69] Furthermore, the PDOS of O_2-Fe on both defect moieties, shown in Figure 1.6, has the same CO oxidation energy barrier for both Fe/N0 and Fe/N1. This can be understood by considering the similar level of spin state asymmetry near the Fermi level on both defects. Even though there is greater charge

transfer to O_2 adsorbed to Fe/N1, and a greater local magnetic moment for O_2 adsorbed to Fe/N0, the energy barrier values most closely correlate to the behavior of the spin split orbitals near the Fermi level in the PDOS.

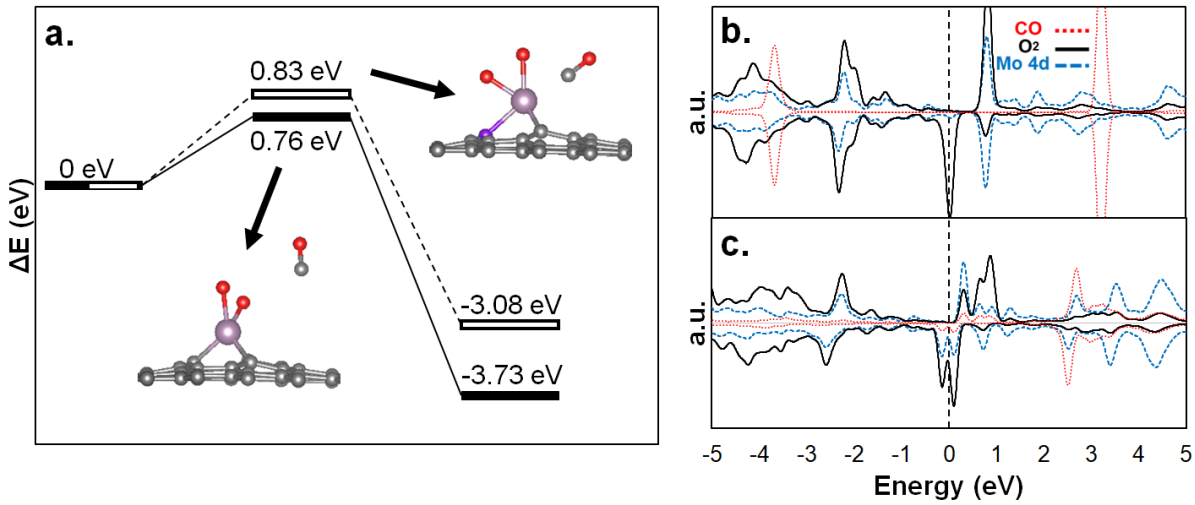

Figure 1.7. a) Energy levels of the initial state (IS), transition state (TS), and final state (FS) for N0 (solid black) and N1 (hollow bar). Insets show relaxed geometry for TS of O_2-Mo/N0 and O_2-Mo/N1. Grey, purple, red, and light purple spheres correspond to C, N, O, and Mo atoms, respectively. Spin polarized projected density of states (PDOS) for TS of b) O_2-Mo/N0 and c) O_2-Mo/N1 with Fermi energy highlighted with a vertical dashed line. Blue dashed curve shows local PDOS of adsorbed TM adatom d orbitals. Red dotted and black solid curves show local PDOS for CO and O_2 molecules, respectively. All positive values correspond to spin up and all negative values are spin down.

The chemical activity of Ta SAC for CO oxidation showed a significant improvement on N1 in terms of lower barrier energy compared to Ta/N0, with an activation energy barrier of 0.66 eV compared to 0.91 eV as shown in Figure 1.8a. The electronic charge transfer to O_2, shown in Table 1.3, for Ta/N0 and Ta/N1 was remarkably similar. Furthermore, the geometric structures of O_2 on the Ta/N0 and Ta/N1 TS observed in the insets of Figure 1.8a both exhibit a side-on bonding configuration (see also Table 1.2). In

contrast to the similar charge transfer and geometry between Ta defect moieties, there is a clear difference in the PDOS of Ta/N0 compared to Ta/N1. The symmetry of the PDOS of Ta/N0, in Figure 1.8b, has no discernable magnetic moment and shows a higher number of states very close to the Fermi level (within 1 eV). Additionally, both the PDOS of Ta/N0 and Ta/N1 have similar densities of Ta 5d orbitals near the Fermi level. However, the PDOS for the Ta/N1 TS (Figure 1.8c) shows a large spin state asymmetry near the Fermi level for the adsorbed O_2 molecule. Thus, spin state asymmetry appears to destabilize the O_2 bond, increasing reactivity and lowering the barrier energy for CO oxidation on Ta/N1 by 27%.

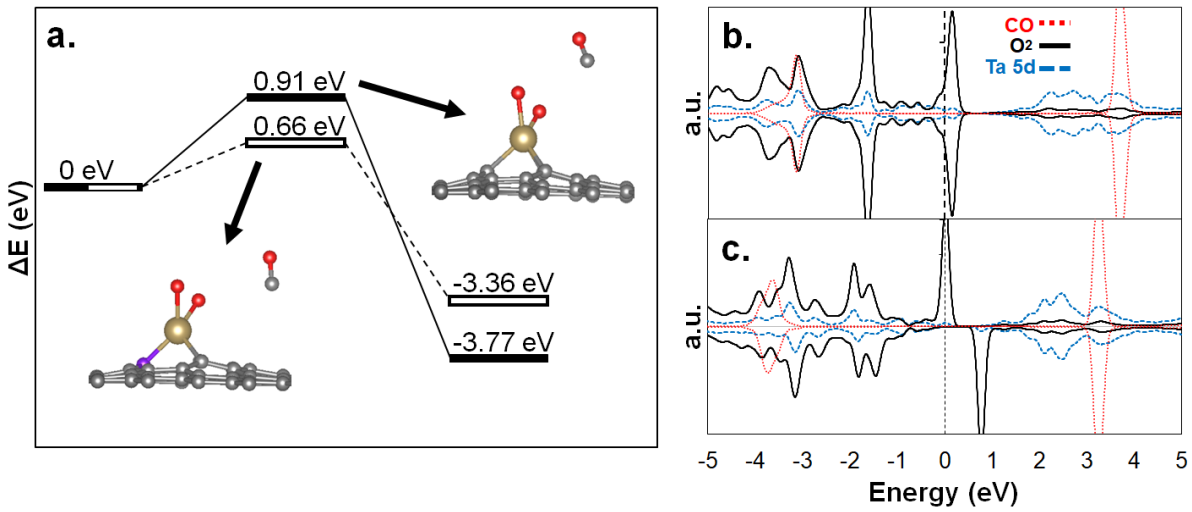

Figure 1.8. a) Energy levels of the initial state (IS), transition state (TS), and final state (FS) for N0 (solid black) and N1 (hollow bar). Insets show relaxed geometry for TS of O_2-Ta/N0 and O_2-Ta/N1. Grey, purple, red, and yellow spheres correspond to C, N, O, and Ta atoms, respectively. Spin polarized density of states for TS of b) O_2-Ta/N0 and c) O_2-Ta/N1. Blue dashed curve shows local PDOS of adsorbed TM adatom d orbitals. Red dotted and black solid curves show local PDOS for CO and O_2 molecules, respectively. The Fermi levels have been set to 0 eV, indicated with a vertical dashed black line. All positive values correspond to spin up and all negative values are spin down.

The initial, transition, and final states of CO oxidation on Ta/N0 produced with NEB calculations had zero magnetic moment. This motivated additional NEB calculations to

compare the activation barrier energies of spin-constrained reaction pathways having differing spin states. By constraining the magnetic moment of the CO oxidation reaction facilitated by Ta/N0 to be either 1 (doublet) or 3 (quartet) states, we found significantly lower energy barriers compared to the non-magnetic spin state, shown in Table 1.5. The energy barriers of the doublet and quartet spin states were found to be quite similar with less than 0.05 eV of difference. Since mainly the frontier orbital affects bonding, magnetic moment alone does not explain differences in chemical activity. Higher spin states may consist of unpaired electrons in both the frontier as well as orbitals further away from the Fermi energy, thus they are expected to have similar energy barriers when the spin asymmetry near the Fermi energy is similar.

Table 1.5: Activation Barrier Energies of Spin-Constrained CO Oxidation on Ta/N0

Defect Moiety		**E_A [eV]**
Ta/N0	**m = 0**	0.91
	m = 1	0.36
	m = 3	0.32

Lastly, we consider the impressive improvement between V/N0 and V/N1, a decrease in activation energy barrier of 44%, comparable to CO oxidation on a Pt surface.[70] The adsorbing O_2 molecule undergoes a shift in geometry, from side-on to end-on absorption for the N0 and N1 molecular environments, respectively, as discussed previously and which can be seen in the insets of Figure 1.9a. This shift is not thought to

result in a beneficial steric advantage. Despite the increased proximity of the end-on O_2 molecule to the reacting physisorbed CO molecule, previous work has found that a similar end-on O_2 adsorbed on Au SAC displayed significantly higher activation energy barriers for CO oxidation than side-on.[69] The increased magnetic moment conferred by the N1 defect moiety could also be responsible for the change in O_2 adsorption geometry from side-on to end-on, which agrees with a finding demonstrated by Orellana for a similar system.[29] Rather than steric advantage explaining the lower energy barrier for V/N1, there is a strong spin state asymmetry in the V peaks near the Fermi level, larger in energy separation and magnitude as compared to the TS for V/N0 (Figure 1.9b). This effect could explain why the activation energy barrier for V/N1 is 44% lower than V/N0, despite V/N0 having more charge transfer to O_2 shown in Table 1.4. Thus spin state asymmetry appears to lower the barrier energies for CO oxidation for all systems.

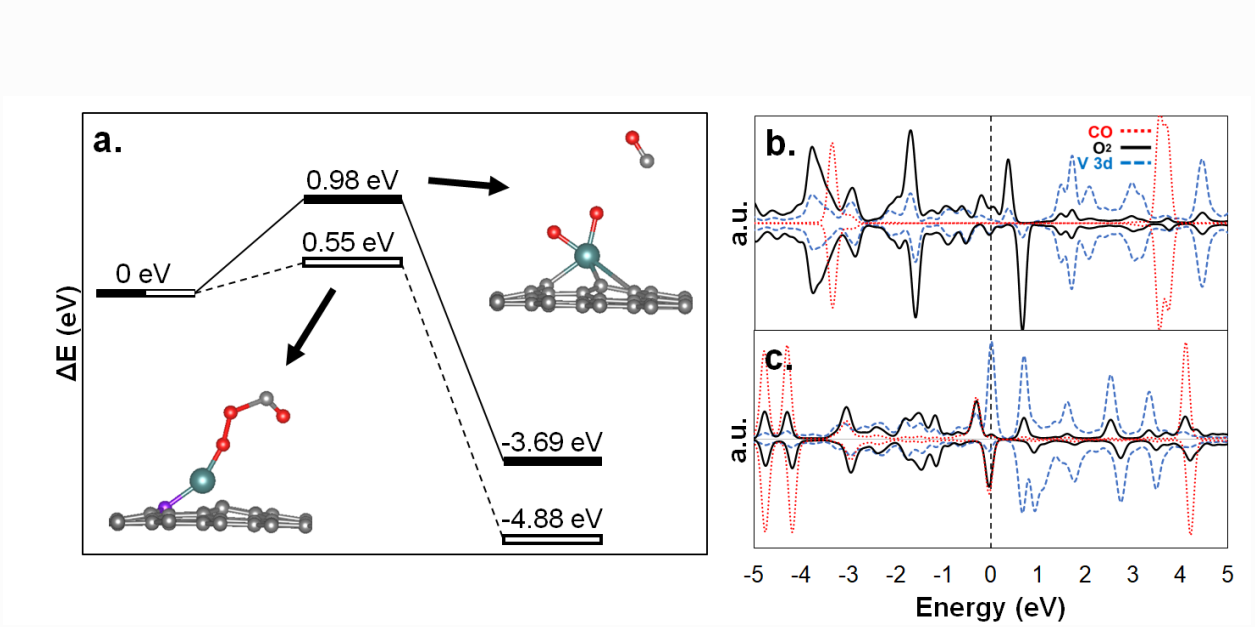

Figure 1.9. a) Energy levels of the initial state (IS), transition state (TS), and final state (FS) for N0 (solid black) and N1 (hollow bar). Insets show relaxed geometry for TS of O_2-V/N0 and O_2-V/N1. Grey, purple, red, and green spheres correspond to C, N, O, and V atoms, respectively.

Spin polarized density of states for TS of b) O_2-V/N0 and c) O_2-V/N1. Blue dashed curve shows local PDOS of adsorbed TM adatom d orbitals. Red dotted and black solid curves show local PDOS for CO and O_2 molecules, respectively. The Fermi levels have been set to 0 eV, indicated with a vertical dashed black line. All positive values correspond to spin up and all negative values are spin down.

1.4 Conclusion

Through first principles calculations, the performance of a wide range of earth-abundant transition metals (V, Fe, Mo, and Ta) as SAC for CO oxidation on two types of graphene surface defects (N0, N1) has been evaluated. Further, by calculating the activation energy barriers of CO oxidation reactions facilitated by these stabilized SAC through a modified Eley-Rideal pathway, we found that all four metals have energy barriers <1 eV on both defect types and significantly the pyridinic N dopant accesses energy barriers below 0.8 eV for all metals. Compared to our previous work modelling the same reaction with single atom Pt for a Langmuir-Hinshelwood pathway, V on N1 is comparable to the performance of a Pt surface[70] and is the most competitive with SAC Pt catalysts[17,71] with an activation energy of 0.55 eV. The spin polarized projected density of states shows that greater spin state asymmetry in atomic and molecular orbital peaks near the Fermi level is associated with lower activation energy barriers, where associated decreases in activation barrier energies of CO oxidation of 44% and 27% were observed for V and Ta, respectively. Our work both extends the range of earth-abundant choices for SAC and reveals the importance of molecular coordination affecting the magnetic moment and in turn binding energies and activation energy barriers. This provides further means for improving the chemical activity of earth-abundant transition metals. Parsing the large parameter space composed of TM elements and surface defects will aid in the design of earth abundant and

sustainable catalysts. These results can guide selection of materials for investigations using techniques such as high-angle annular dark-field-scanning transmission electron microscopy (HAADF-STEM) and spin-resolved electron energy loss spectroscopy (EELS) to probe chemical bonding and local electronic structure alongside with *in situ* catalytic reactions. Relationships between molecular coordination, local magnetic moment, and catalytic activity gleaned from experiments can further elucidate how spin state can provide an additional knob for tuning chemical activity. A promising future avenue is to explore the effect of spin on other molecular coordinations of TM SAC on graphene in order to identify systems that may meet or exceed the performance of PGM.

1.5 References

(1) Bai, J.; Zhu, Q.; Lv, Z.; Dong, H.; Yu, J.; Dong, L. Nitrogen-Doped Graphene as Catalysts and Catalyst Supports for Oxygen Reduction in Both Acidic and Alkaline Solutions. *International Journal of Hydrogen Energy* **2013**, *38* (3), 1413–1418. https://doi.org/10.1016/j.ijhydene.2012.11.039.

(2) Qu, L.; Liu, Y.; Baek, J.-B.; Dai, L. Nitrogen-Doped Graphene as Efficient Metal-Free Electrocatalyst for Oxygen Reduction in Fuel Cells. *ACS Nano* **2010**, *4* (3), 1321–1326. https://doi.org/10.1021/nn901850u.

(3) Gasteiger, H. A.; Kocha, S. S.; Sompalli, B.; Wagner, F. T. Activity Benchmarks and Requirements for Pt, Pt-Alloy, and Non-Pt Oxygen Reduction Catalysts for PEMFCs. *Applied Catalysis B: Environmental* **2005**, *56* (1), 9–35. https://doi.org/10.1016/j.apcatb.2004.06.021.

(4) Cheng, N.; Stambula, S.; Wang, D.; Banis, M. N.; Liu, J.; Riese, A.; Xiao, B.; Li, R.; Sham, T.-K.; Liu, L.-M.; Botton, G. A.; Sun, X. Platinum Single-Atom and Cluster Catalysis of the Hydrogen Evolution Reaction. *Nat Commun* **2016**, *7* (1), 13638. https://doi.org/10.1038/ncomms13638.

(5) Rivera-Cárcamo, C.; Serp, P. Single Atom Catalysts on Carbon-Based Materials. *ChemCatChem* **2018**, *10* (22), 5058–5091. https://doi.org/10.1002/cctc.201801174.

(6) Yoo, E.; Okata, T.; Akita, T.; Kohyama, M.; Nakamura, J.; Honma, I. Enhanced Electrocatalytic Activity of Pt Subnanoclusters on Graphene Nanosheet Surface. *Nano Lett.* **2009**, *9* (6), 2255–2259. https://doi.org/10.1021/nl900397t.

(7) Jiang, K.; Back, S.; Akey, A. J.; Xia, C.; Hu, Y.; Liang, W.; Schaak, D.; Stavitski, E.; Nørskov, J. K.; Siahrostami, S.; Wang, H. Highly Selective Oxygen Reduction to Hydrogen Peroxide on Transition Metal Single Atom Coordination. *Nat Commun* **2019**, *10* (1), 3997. https://doi.org/10.1038/s41467-019-11992-2.

(8) Yang, S.; Tak, Y. J.; Kim, J.; Soon, A.; Lee, H. Support Effects in Single-Atom Platinum Catalysts for Electrochemical Oxygen Reduction. *ACS Catal.* **2017**, *7* (2), 1301–1307. https://doi.org/10.1021/acscatal.6b02899.

(9) Wang, A.; Li, J.; Zhang, T. Heterogeneous Single-Atom Catalysis. *Nat Rev Chem* **2018**, *2* (6), 65–81. https://doi.org/10.1038/s41570-018-0010-1.

(10) Lu, J.; Serna, P.; Aydin, C.; Browning, N. D.; Gates, B. C. Supported Molecular Iridium Catalysts: Resolving Effects of Metal Nuclearity and Supports as Ligands. *J. Am. Chem. Soc.* **2011**, *133* (40), 16186–16195. https://doi.org/10.1021/ja206486j.

(11) Getsoian, A. "Bean"; Das, U.; Camacho-Bunquin, J.; Zhang, G.; Gallagher, J. R.; Hu, B.; Cheah, S.; Schaidle, J. A.; Ruddy, D. A.; Hensley, J. E.; Krause, T. R.; Curtiss, L. A.; Miller, J. T.; Hock, A. S. Organometallic Model Complexes Elucidate the Active Gallium Species in Alkane Dehydrogenation Catalysts Based on Ligand Effects in Ga K-Edge XANES. *Catal. Sci. Technol.* **2016**, *6* (16), 6339–6353. https://doi.org/10.1039/C6CY00698A.

(12) Qiao, B.; Wang, A.; Yang, X.; Allard, L. F.; Jiang, Z.; Cui, Y.; Liu, J.; Li, J.; Zhang, T. Single-Atom Catalysis of CO Oxidation Using Pt1/FeOx. *Nature Chem* **2011**, *3* (8), 634–641. https://doi.org/10.1038/nchem.1095.

(13) Yang, X.-F.; Wang, A.; Qiao, B.; Li, J.; Liu, J.; Zhang, T. Single-Atom Catalysts: A New Frontier in Heterogeneous Catalysis. *Acc. Chem. Res.* **2013**, *46* (8), 1740–1748. https://doi.org/10.1021/ar300361m.

(14) Yan, D.; Li, Y.; Huo, J.; Chen, R.; Dai, L.; Wang, S. Defect Chemistry of Nonprecious-Metal Electrocatalysts for Oxygen Reactions. *Adv. Mater.* **2017**, *29* (48), 1606459. https://doi.org/10.1002/adma.201606459.

(15) Li, L.; Chang, X.; Lin, X.; Zhao, Z.-J.; Gong, J. Theoretical Insights into Single-Atom Catalysts. *Chem. Soc. Rev.* **2020**, *49* (22), 8156–8178. https://doi.org/10.1039/D0CS00795A.

(16) Zhang, H.; Li, J.; Xi, S.; Du, Y.; Hai, X.; Wang, J.; Xu, H.; Wu, G.; Zhang, J.; Lu, J.; Wang, J. A Graphene-Supported Single-Atom FeN_5 Catalytic Site for Efficient Electrochemical CO_2 Reduction. *Angew. Chem. Int. Ed.* **2019**, *58* (42), 14871–14876. https://doi.org/10.1002/anie.201906079.

(17) Wang, C. S.; Wang, H.; Wu, R.; Ragan, R. Evaluating the Stability of Single-Atom Catalysts with High Chemical Activity. *The Journal of Physical Chemistry C* **2018**, *122* (38), 21919–21926. https://doi.org/10.1021/acs.jpcc.8b06621.

(18) Esrafili, M. D.; Heydari, S. CO Oxidation Catalyzed by a Single Ti Atom Supported on Divacancy Defective Graphene: A Dispersion-Corrected DFT Study. *ChemistrySelect* **2018**, *3* (16), 4471–4479. https://doi.org/10.1002/slct.201800573.

(19) Song, M.; Song, Y.; Sha, W.; Xu, B.; Guo, J.; Wu, Y. Recent Advances in Non-Precious Transition Metal/Nitrogen-Doped Carbon for Oxygen Reduction Electrocatalysts in PEMFCs. *Catalysts* **2020**, *10* (1), 141. https://doi.org/10.3390/catal10010141.

(20) Seabourne, C. R.; Scott, A. J.; Brydson, R.; Nicholls, R. J. A Systematic Approach to Choosing

Parameters for Modelling Fine Structure in Electron Energy-Loss Spectroscopy. *Ultramicroscopy* **2009**, *109* (11), 1374–1388. https://doi.org/10.1016/j.ultramic.2009.07.002.

(21) Idrobo, J. C.; Rusz, J.; Spiegelberg, J.; McGuire, M. A.; Symons, C. T.; Vatsavai, R. R.; Cantoni, C.; Lupini, A. R. Detecting Magnetic Ordering with Atomic Size Electron Probes. *Adv Struct Chem Imag* **2016**, *2* (1), 5. https://doi.org/10.1186/s40679-016-0019-9.

(22) Negi, D.; Zeiger, P. M.; Jones, L.; Idrobo, J.-C.; van Aken, P. A.; Rusz, J. Prospect for Detecting Magnetism of a Single Impurity Atom Using Electron Magnetic Chiral Dichroism. *Phys. Rev. B* **2019**, *100* (10), 104434. https://doi.org/10.1103/PhysRevB.100.104434.

(23) Witt, J. A.; Mumm, D. R.; Mohraz, A. Microstructural Tunability of Co-Continuous Bijel-Derived Electrodes to Provide High Energy and Power Densities. *J. Mater. Chem. A* **2016**, *4* (3), 1000–1007. https://doi.org/10.1039/C5TA06260H.

(24) Garcia, A. E.; Wang, C. S.; Sanderson, R. N.; McDevitt, K. M.; Zhang, Y.; Valdevit, L.; Mumm, D. R.; Mohraz, A.; Ragan, R. Scalable Synthesis of Gyroid-Inspired Freestanding Three-Dimensional Graphene Architectures. *Nanoscale Adv.* **2019**, *1* (10), 3870–3882. https://doi.org/10.1039/C9NA00358D.

(25) Torquato, S.; Hyun, S.; Donev, A. Multifunctional Composites: Optimizing Microstructures for Simultaneous Transport of Heat and Electricity. *Phys. Rev. Lett.* **2002**, *89* (26), 266601. https://doi.org/10.1103/PhysRevLett.89.266601.

(26) Chen, H.-Y.; Kwon, Y.; Thornton, K. Multifunctionality of Three-Dimensional Self-Assembled Composite Structure. *Scripta Materialia* **2009**, *61* (1), 52–55. https://doi.org/10.1016/j.scriptamat.2009.03.006.

(27) Yang, B.; Gagliardi, L.; Truhlar, D. G. Transition States of Spin-Forbidden Reactions. *Phys. Chem. Chem. Phys.* **2018**, *20* (6), 4129–4136. https://doi.org/10.1039/C7CP07227A.

(28) Pichugina, D. A.; Polynskaya, Y. G.; Kuz'menko, N. E. Spin and Structural Features of Oxygen Dissociation on Tetrahedral Ag_{20} and $Ag_{19}Au$ Clusters. *Phys. Chem. Chem. Phys.* **2016**, *18* (27), 18033–18044. https://doi.org/10.1039/C6CP01630H.

(29) Orellana, W. Catalytic Properties of Transition Metal–N_4 Moieties in Graphene for the Oxygen Reduction Reaction: Evidence of Spin-Dependent Mechanisms. *J. Phys. Chem. C* **2013**, *117* (19), 9812–9818. https://doi.org/10.1021/jp4002115.

(30) Soliman, N. K. Factors Affecting CO Oxidation Reaction over Nanosized Materials: A Review. *Journal of Materials Research and Technology* **2019**, *8* (2), 2395–2407. https://doi.org/10.1016/j.jmrt.2018.12.012.

(31) Kresse, G.; Furthmüller, J. Efficiency of Ab-Initio Total Energy Calculations for Metals and Semiconductors Using a Plane-Wave Basis Set. *Computational Materials Science* **1996**, *6* (1), 15–50. https://doi.org/10.1016/0927-0256(96)00008-0.

(32) Kresse, G.; Furthmüller, J. Efficient Iterative Schemes for Ab Initio Total-Energy Calculations Using a Plane-Wave Basis Set. *Phys. Rev. B* **1996**, *54* (16), 11169–11186. https://doi.org/10.1103/PhysRevB.54.11169.

(33) Kresse, G.; Joubert, D. From Ultrasoft Pseudopotentials to the Projector Augmented-Wave Method. *Phys. Rev. B* **1999**, *59* (3), 1758–1775. https://doi.org/10.1103/PhysRevB.59.1758.

(34) Blöchl, P. E. Projector Augmented-Wave Method. *Phys. Rev. B* **1994**, *50* (24), 17953–17979. https://doi.org/10.1103/PhysRevB.50.17953.

(35) Perdew, J. P.; Burke, K.; Ernzerhof, M. Generalized Gradient Approximation Made Simple. *Phys. Rev. Lett.* **1996**, *77* (18), 3865–3868. https://doi.org/10.1103/PhysRevLett.77.3865.

(36) Dudarev, S. L.; Botton, G. A.; Savrasov, S. Y.; Humphreys, C. J.; Sutton, A. P. Electron-Energy-Loss Spectra and the Structural Stability of Nickel Oxide: An LSDA+U Study. *Phys. Rev. B* **1998**, *57* (3), 1505–1509. https://doi.org/10.1103/PhysRevB.57.1505.

(37) Sun, J.; Ruzsinszky, A.; Perdew, J. P. Strongly Constrained and Appropriately Normed Semilocal Density Functional. *Phys. Rev. Lett.* **2015**, *115* (3), 036402. https://doi.org/10.1103/PhysRevLett.115.036402.

(38) Calderon, C. E.; Plata, J. J.; Toher, C.; Oses, C.; Levy, O.; Fornari, M.; Natan, A.; Mehl, M. J.; Hart, G.; Buongiorno Nardelli, M.; Curtarolo, S. The AFLOW Standard for High-Throughput Materials Science Calculations. *Computational Materials Science* **2015**, *108*, 233–238. https://doi.org/10.1016/j.commatsci.2015.07.019.

(39) Sun, J.; Remsing, R. C.; Zhang, Y.; Sun, Z.; Ruzsinszky, A.; Peng, H.; Yang, Z.; Paul, A.; Waghmare, U.; Wu, X.; Klein, M. L.; Perdew, J. P. Accurate First-Principles Structures and Energies of Diversely Bonded Systems from an Efficient Density Functional. *Nature Chem* **2016**, *8* (9), 831–836. https://doi.org/10.1038/nchem.2535.

(40) Monkhorst, H. J.; Pack, J. D. Special Points for Brillouin-Zone Integrations. *Phys. Rev. B* **1976**, *13* (12), 5188–5192. https://doi.org/10.1103/PhysRevB.13.5188.

(41) Bader, R. F. W. *Atoms in Molecules—A Quantum Theory*; Oxford University Press: Oxford, 1990.

(42) Tang, W.; Sanville, E.; Henkelman, G. A Grid-Based Bader Analysis Algorithm without Lattice Bias. *J. Phys.: Condens. Matter* **2009**, *21* (8), 084204. https://doi.org/10.1088/0953-8984/21/8/084204.

(43) Henkelman, G.; Uberuaga, B. P.; Jónsson, H. A Climbing Image Nudged Elastic Band Method for Finding Saddle Points and Minimum Energy Paths. *J. Chem. Phys.* **2000**, *113* (22), 9901–9904. https://doi.org/10.1063/1.1329672.

(44) Henkelman, G.; Jónsson, H. A Dimer Method for Finding Saddle Points on High Dimensional Potential Surfaces Using Only First Derivatives. *J. Chem. Phys.* **1999**, *111* (15), 7010–7022. https://doi.org/10.1063/1.480097.

(45) Krasheninnikov, A. V.; Lehtinen, P. O.; Foster, A. S.; Pyykkö, P.; Nieminen, R. M. Embedding Transition-Metal Atoms in Graphene: Structure, Bonding, and Magnetism. *Physical Review Letters* **2009**, *102* (12). https://doi.org/10.1103/PhysRevLett.102.126807.

(46) Guo, X.; Huang, S. Tuning Nitrogen Reduction Reaction Activity via Controllable Fe Magnetic Moment: A Computational Study of Single Fe Atom Supported on Defective Graphene. *Electrochimica Acta* **2018**, *284*, 392–399. https://doi.org/10.1016/j.electacta.2018.07.168.

(47) Kropp, T.; Mavrikakis, M. Transition Metal Atoms Embedded in Graphene: How Nitrogen Doping Increases CO Oxidation Activity. *ACS Catal.* **2019**, *9* (8), 6864–6868. https://doi.org/10.1021/acscatal.9b01944.

(48) Kattel, S.; Atanassov, P.; Kiefer, B. Stability, Electronic and Magnetic Properties of In-Plane

Defects in Graphene: A First-Principles Study. *J. Phys. Chem. C* **2012**, *116* (14), 8161–8166. https://doi.org/10.1021/jp2121609.

(49) Yazyev, O. V. Emergence of Magnetism in Graphene Materials and Nanostructures. *Rep. Prog. Phys.* **2010**, *73* (5), 056501. https://doi.org/10.1088/0034-4885/73/5/056501.

(50) Ma, C.; Liao, Q.; Sun, H.; Lei, S.; Zheng, Y.; Yin, R.; Zhao, A.; Li, Q.; Wang, B. Tuning the Doping Types in Graphene Sheets by N Monoelement. *Nano Lett.* **2018**, *18* (1), 386–394. https://doi.org/10.1021/acs.nanolett.7b04249.

(51) Tison, Y.; Lagoute, J.; Repain, V.; Chacon, C.; Girard, Y.; Rousset, S.; Joucken, F.; Sharma, D.; Henrard, L.; Amara, H.; Ghedjatti, A.; Ducastelle, F. Electronic Interaction between Nitrogen Atoms in Doped Graphene. *ACS Nano* **2015**, *9* (1), 670–678. https://doi.org/10.1021/nn506074u.

(52) Wu, M.; Cao, C.; Jiang, J. Z. Light Non-Metallic Atom (B, N, O and F)-Doped Graphene: A First-Principles Study. *Nanotechnology* **2010**, *21* (50), 505202. https://doi.org/10.1088/0957-4484/21/50/505202.

(53) Zhang, Y.-H.; Chen, Y.-B.; Zhou, K.-G.; Liu, C.-H.; Zeng, J.; Zhang, H.-L.; Peng, Y. Improving Gas Sensing Properties of Graphene by Introducing Dopants and Defects: A First-Principles Study. *Nanotechnology* **2009**, *20* (18), 185504. https://doi.org/10.1088/0957-4484/20/18/185504.

(54) Ghosh, D.; K. Pati, S. Trapping of Gaseous Pollutants on Defective N-Doped Graphene. *Physical Chemistry Chemical Physics* **2017**, *19* (1), 636–643. https://doi.org/10.1039/C6CP06247D.

(55) Nørskov, J. K.; Rossmeisl, J.; Logadottir, A.; Lindqvist, L.; Kitchin, J. R.; Bligaard, T.; Jónsson, H. Origin of the Overpotential for Oxygen Reduction at a Fuel-Cell Cathode. *J. Phys. Chem. B* **2004**, *108* (46), 17886–17892. https://doi.org/10.1021/jp047349j.

(56) Kattel, S.; Atanassov, P.; Kiefer, B. Density Functional Theory Study of Ni–N_x/C Electrocatalyst for Oxygen Reduction in Alkaline and Acidic Media. *J. Phys. Chem. C* **2012**, *116* (33), 17378–17383. https://doi.org/10.1021/jp3044708.

(57) Liu, J.; Lucci, F. R.; Yang, M.; Lee, S.; Marcinkowski, M. D.; Therrien, A. J.; Williams, C. T.; Sykes, E. C. H.; Flytzani-Stephanopoulos, M. Tackling CO Poisoning with Single-Atom Alloy Catalysts. *J. Am. Chem. Soc.* **2016**, *138* (20), 6396–6399. https://doi.org/10.1021/jacs.6b03339.

(58) Wu, L.; Cao, X.; Hu, W.; Ji, Y.; Zhu, Z.-Z.; Li, X.-F. Improving the Oxygen Reduction Reaction Activity of FeN_4–Graphene via Tuning Electronic Characteristics. *ACS Appl. Energy Mater.* **2019**, *2* (9), 6634–6641. https://doi.org/10.1021/acsaem.9b01164.

(59) Calle-Vallejo, F.; Martínez, J. I.; Rossmeisl, J. Density Functional Studies of Functionalized Graphitic Materials with Late Transition Metals for Oxygen Reduction Reactions. *Phys. Chem. Chem. Phys.* **2011**, *13* (34), 15639. https://doi.org/10.1039/c1cp21228a.

(60) Liang, W.; Chen, J.; Liu, Y.; Chen, S. Density-Functional-Theory Calculation Analysis of Active Sites for Four-Electron Reduction of O_2 on Fe/N-Doped Graphene. *ACS Catal.* **2014**, *4* (11), 4170–4177. https://doi.org/10.1021/cs501170a.

(61) Tang, J.-Y.; Shen, J.-S.; Chen, L.; Jiang, J.-W.; Lu, J.; Zhao, X.; Dai, G.-L. Investigation of Carbon Monoxide Catalytic Oxidation on Vanadium-Embedded Graphene. *Monatsh Chem* **2018**, *149* (8), 1349–1356. https://doi.org/10.1007/s00706-018-2181-3.

(62) Li, Y.; Zhou, Z.; Yu, G.; Chen, W.; Chen, Z. CO Catalytic Oxidation on Iron-Embedded Graphene: Computational Quest for Low-Cost Nanocatalysts. *J. Phys. Chem. C* **2010**, *114* (14), 6250–6254. https://doi.org/10.1021/jp911535v.

(63) Xu, X.-Y.; Xu, H.; Guo, H.; Zhao, C. Mechanism Investigations on CO Oxidation Catalyzed by Fe-Doped Graphene: A Theoretical Study. *Applied Surface Science* **2020**, *523*, 146496. https://doi.org/10.1016/j.apsusc.2020.146496.

(64) Deng, Q.; Zhao, L.; Gao, X.; Zhang, M.; Luo, Y.; Zhao, Y. Single Layer of Polymeric Cobalt Phthalocyanine: Promising Low-Cost and High-Activity Nanocatalysts for CO Oxidation. *Small* **2013**, *9* (20), 3506–3513. https://doi.org/10.1002/smll.201300652.

(65) Li, F.; Li, Y.; Zeng, X. C.; Chen, Z. Exploration of High-Performance Single-Atom Catalysts on Support M1/FeOx for CO Oxidation via Computational Study. *ACS Catal.* **2015**, *5* (2), 544–552. https://doi.org/10.1021/cs501790v.

(66) Luo, M.; Liang, Z.; Liu, C.; Liu, M.; Qi, X.; Chen, M.; Yang, H.; Liang, T. Theoretical Calculation of Different Reaction Mechanisms for CO Oxidation on MnN3-Doped Graphene. *ACS Omega* **2020**, *5* (33), 21203–21210. https://doi.org/10.1021/acsomega.0c02930.

(67) Wang, M.; Wang, Z. Single Ni Atom Incorporated with Pyridinic Nitrogen Graphene as an Efficient Catalyst for CO Oxidation: First-Principles Investigation. *RSC Adv.* **2017**, *7* (77), 48819–48824. https://doi.org/10.1039/C7RA06591D.

(68) Liu, J.; Jiao, M.; Lu, L.; Barkholtz, H. M.; Li, Y.; Wang, Y.; Jiang, L.; Wu, Z.; Liu, D.; Zhuang, L.; Ma, C.; Zeng, J.; Zhang, B.; Su, D.; Song, P.; Xing, W.; Xu, W.; Wang, Y.; Jiang, Z.; Sun, G. High Performance Platinum Single Atom Electrocatalyst for Oxygen Reduction Reaction. *Nat Commun* **2017**, *8* (1), 15938. https://doi.org/10.1038/ncomms15938.

(69) Fu, Z.; Yang, B.; Wu, R. Understanding the Activity of Single-Atom Catalysis from Frontier Orbitals. *Phys. Rev. Lett.* **2020**, *125* (15), 156001. https://doi.org/10.1103/PhysRevLett.125.156001.

(70) Farkas, A.; Zalewska-Wierzbicka, K.; Bachmann, C.; Goritzka, J.; Langsdorf, D.; Balmes, O.; Janek, J.; Over, H. High Pressure Carbon Monoxide Oxidation over Platinum (111). *J. Phys. Chem. C* **2013**, *117* (19), 9932–9942. https://doi.org/10.1021/jp401867g.

(71) Tang, Y.; Yang, Z.; Dai, X. A Theoretical Simulation on the Catalytic Oxidation of CO on Pt/Graphene. *Phys. Chem. Chem. Phys.* **2012**, *14* (48), 16566. https://doi.org/10.1039/c2cp41441d.

CHAPTER 2: TAILORING PLASMONIC NANOGAP CHEMISTRY TOWARDS FOLLOWING CHEMICAL REACTIONS IN REAL TIME

2.1 Introduction

Control of nanogap spacing and surface chemistry in plasmonic hotspots between NP has numerous applications including sensors, non-linear optics,[1] and photocatalysis.[2,3] For example, tuning interactions between analytes and plasmonic hot spots for (bio)molecular sensors can be achieved with surface chemistry.[4] The varying strength of interactions as well as altered geometric configurations between the nanogap molecule and analytes has been shown to shift otherwise overlapping vibrational modes in spectra, allowing for high-dimensionality discrimination of complex biological samples.[4] Furthermore, the reproducibility of the vibrational fingerprint of surface enhanced Raman scattering (SERS) surfaces depends on nanoparticle morphology, nanogap distance and surface chemistry. Few systems such as DNA-tethered NP [5,6] and NP on mirror cavities[7] achieve control of nanogap chemistry and gap spacing in sub-nanometer regime that are both needed to simultaneously achieve low detection limits and reproducible signals for accurate quantification.[8]

Here we present an experimental platform to facilitate interactions between plasmonic NP in colloidal solution to define versatile chemistry in plasmonic nanogaps, thereby controlling nanogap spacing and subsequent chemical reactivity to form *plasmonic nanoreactors*. As colloidal NP are typically stabilized via electrostatic repulsion, chemical crosslinking in solution will normally lead to aggregation. Electrohydrodynamic (EHD) flow, an electro-osmotic driving force, provides a transient attractive force that is confined

to a working electrode surface and thus mitigates uncontrolled aggregation in bulk solution. We have previously demonstrated that EHD drives chemical reactions between NP and produces controlled nanogap spacing[9,10] by forming an acetic anhydride bond between NP.[10] In the absence of EHD flow, we do not experimentally observe anhydride bond formation.[9,10] Nudged elastic band calculations show the activation energy barrier does not vary when distances between NP is varied and thus the effect of close proximity between NPs during EHD flow allows ligands to sample configurational space in the presence of electrical stimuli, thus reactions are governed by entropic effects.[10] This system provides a unique platform to study local chemical reactions using *in situ* SERS spectral imaging as it allows for sub-nanometer gaps that provide maximal enhancement factors before quantum tunneling leads to collapse of field enhancements.[11]

The reactions studied here include carbodiimide coupling chemistry between lipoic acid ligands and between (3,4)mercaptobenzoic acid ligands to investigate the role of electronic structure and steric effects on reactions between NP under EHD driving forces. These three ligands are specifically chosen to represent a range of aromaticity and electron delocalization. Additionally, the chemistry investigated here offers a high degree of versatility for additional reactions; anhydrides undergo hydrolysis to form carboxylic acids,[12] react with alcohols to form esters,[13,14] and react with amines to form amides.[15]

2.2 Materials and Methods

Hydrofluoric acid (HF) was purchased from VWR International. Sodium Hydroxide (NaOH) (50% w/w), toluene, isopropyl alcohol (IPA), and potassium carbonate were purchased from Fisher Scientific. 2-(N-Morpholino)ethanesulfonic acid (MES) 0.1 M buffer,

1-ethyl-3-[3-(dimethylamino)propyl]carbodiimide hydrochloride (EDC), N-hydroxysulfosuccinimide (s-NHS), ethylenediamine, dimethyl sulfoxide (DMSO), lipoic acid, 4-mercaptobenzoic acid (4MBA), 3-mercaptobenzoic acid (3MBA), and benzenethiol (BZT) were purchased from Sigma-Aldrich. Ethanol was purchased from Gold Shield Distributors, Inc.. Nanopure deionized (DI) water (18.2 MΩ cm-1) was obtained from a Milli-Q Millipore System.

Electrode Materials. The working electrode is composed of P-type, boron doped, (100) silicon wafers (University Wafer) with resistivity of 0.001-0.005 ohm-cm. Si wafers are cleaned in a 20 % v/v HF aqueous solution and then coated with random copolymer poly(styrene-co-methyl methacrylate)-alpha-hydroxyl-omega-tempo moiety (PS-r-PMMA) (Mn = 7400, 59.6% PS) and diblock copolymer poly(styrene-block- methyl methacrylate) (PS-b-PMMA) (Mn = 170-b-144 kg mol-1), which were purchased from Polymer Source, Inc. *HF has serious potential to cause severe injury which mandates extreme care during treatment.* First, 1 wt% PS-r-PMMA in toluene was spin-coated onto Si wafers at 3000 rpm for 45 s, annealed under vacuum at 170 °C for 48 hr, and then rinsed with toluene to leave a brush layer. Next, PS-b-PMMA is spin coated at 5000 rpm for 45 s and then annealed for 72 hr at 170 °C. PMMA domains on PS-b-PMMA/Si are functionalized with amine groups for coupling to Au NP by immersing in DMSO for 5 min and then 5 % vol % ethylenediamine in DMSO for 5 min, without rinsing in between steps. The functionalized electrodes are then rinsed with IPA for 1 min and dried under nitrogen gas for immediate use.

Gold Nanoparticle Surface Functionalization. Citrate stabilized and lipoic acid functionalized Au NP with a diameter of 40 nm diameter were purchased from

Nanocomposix. Citrate stabilized Au NP are functionalized with 4MBA (Au-4MBA) as follows: First, 10 mL of citrate stabilized Au NP is mixed with K_2CO_3 in a 1.5 mL:2 uL ratio and centrifuged for 30 min at 1.7 rcf and the original solvent is removed - how. The solution is resuspended in a basic solution of NaOH diluted in DI water to have a pH of 11.7 and 0.01 M 4MBA in ethanol was added to the Au NP solution to produce 10 uM 4MBA in Au NP solution (1:1000 v/v). The solution was continuously stirred overnight. Finally, the obtained solution was centrifuged for 30 min at 1.7 rcf to remove the excess of 4MBA and was dispersed in DI water. Citrate stabilized Au NP are functionalized with 3-MBA (Au-3MBA) following the same procedure as above: the basic solution of Au NP was mixed with 0.01 M 3-MBA in ethanol to produce 10 uM 3-MBA in Au NP solution (1:1000 v/v).

Nanoreactor Fabrication. Functionalized Au NPs P solution (0.1 mg/mL, 3 mL) is added to a clean 10 mL glass beaker; s-NHS (20 mM) in MES (0.1 M) buffer (24 μL) is added and swirled; and EDC (8 mM) in MES (0.1 M) buffer (24 μL) is added and swirled. 25 μL of the solution is dropped on an ITO counter electrode and assembled in a capacitor architecture using a 90 μm spacer layer (9816L, 3M) with a recently prepared copolymer-coated Si electrode on top. An AC potential with an amplitude of 5 V is applied across the liquid cell at a frequency of 100 Hz for 2 min to deposit predominantly isolated Au NP. The electrodes are disassembled and rinsed with IPA, dried under nitrogen, rinsed with DI water, and dried under nitrogen. The same Au NP solution is assembled in the cell in the same manner now with Au seeds on the working electrode. An AC potential of the same amplitude as the first step is applied but with a frequency of 500 Hz to drive EHD flow due to perturbation of Au seeds.

Surface Enhanced Raman Scattering (SERS) Characterization. SERS spectra were collected with 1s integration time using a portable i-Raman Plus spectrometer (BWTEK) with excitation wavelength of 785 nm and spectral resolution of 4.5 cm^{-1}. The laser spot size at the focal plane is 80 microns; thus spectral data will include ensemble averages. Select chemical reactions in confined geometries were monitored using an inVia confocal Raman microscope (Renishaw) which enables faster integration time and the ability to monitor reactions on a single cluster.

SERS spectra are pre-processed in three steps: (1) smoothing, (2) baseline correction, and (3) normalization, all done using the Python 3.3 programming language. Smoothing was done with the Savitzky–Golay method[29] as implemented in Scikit-Learn using an 11 pixel window and polynomial order 3. Baseline correction was done with the asymmetric least-squares method[30] and was implemented in NumPy with $\lambda = 10000$, $p = 0.001$. In order to normalize the data, the vibrational band of silicon at 520 cm^{-1} is used as an internal standard and set to 1.

Photoinduced Force Microscopy (PiFM) Characterization. Silicon wafers were purchased from University Wafer. EPO-TEK H21D, two-component epoxy glue, was purchased from Epoxy Technology, Inc., and was used for fabricating template stripped Au (TS-Au) surfaces. Samples for PiFM characterization were produced by drop casting solutions of Au-4MBA, Au-3MBA NP on TS-Au, fabricated following a previously published procedure.[31] Briefly, TS-Au was prepared by gluing gold surfaces with EPO-TEK H21D to silicon substrates, forming a sandwich structure, and cured at 150 °C for 30 mins. After cooling, silicon templates were detached from silicon substrates to expose a TS-Au film

with a root-mean-square roughness less than 0.3 nm over 1 μm × 1 μm as evaluated by AFM. TS-Au films used as substrates for PiFM were used immediately after stripping to maintain a pristine surface for sample deposition. Prepared samples were air-dried and then within minutes were scanned in non-contact mode with a commercial VistaScope atomic force microscope (MolecularVista Inc). The system includes vibration isolation equipment, an acoustic enclosure, and is connected to a clean dry air system to minimize water vapor for IR measurements. A quantum cascade laser system (Block Engineering) with a tuning range from 780 to 1900 cm^{-1} provided IR excitation with a wavenumber resolution of 1 cm^{-1}. The cantilever type was NCH-Au from MolecularVista with a nominal tip radius of 20 nm and 300 kHz resonance. The cantilever was excited at its second resonance around 1.69 MHz for surface-sensitive PiFM sideband difference mode measurements.

***Ab initio* Spectral Simulations.** Density functional theory (DFT) calculations of Raman spectra were carried out in atomic orbital basis sets with Gaussian16[32] while plane-wave calculations utilized the Vienna ab-initio Software Package (VASP).[33,34] In Gaussian16 Au cluster simulations, the geometry optimizations and vibrational frequency calculations were performed with a generalized gradient approximation (GGA) using the PW91 exchange correlation functional.[35] Light atoms, namely H, N, C, O, S, were defined with the 6-311+G(2d,p) basis set while Au utilized the LANL2DZ basis set and effective core potential.[36] These mixed basis sets combined with the PW91 functional have been shown in previous work to accurately model Raman spectra of similar organic molecules adsorbed to gold.[37,38]

Plane-wave DFT calculations of Au surfaces performed using VASP used the projector augmented wave pseudopotentials and the Perdew–Burke–Ernzerhof gradient approximation with an energy cutoff of 400 eV. Structural relaxations were performed with energy convergences of 10^{-9} eV and tight force convergences of 0.0005 eV/Å. Reciprocal space was sampled at the gamma point with a Gaussian smearing of 0.02 eV. Polarizability tensors for each mass-weighted vibrational mode in the forward and reverse directions will be calculated with density functional perturbation theory.[39] Raman scattering activities were found via the derivative of each polarizability tensor with respect to its corresponding vibrational mode, as implemented in the raman-sc package on GitHub.[40] This code was extended to handle frozen atoms as well as Cartesian decomposition of Raman spectra in VASP and will be made publicly available.

2.3 Results and Discussion

2.3.1 Fabrication of controlled surface chemistry in plasmonic nanogaps

Electrohydrodynamic (EHD) flow resulting from an applied AC potential is an electrokinetic phenomenon that can drive lateral assembly of nanoparticles (NP) in response to a perturbation that produces an electric field gradient on an electrode-liquid interface.[9,10,16–18] Here the perturbation consists of Au NP, illustrated in Fig. 2.1A, which are deposited using an AC potential applied across a liquid cell sandwiched between a Si working electrode, which has a thin film of polystyrene-b-poly(methyl methacrylate) (PS-b-PMMA), and ITO coated glass slide. Au NP are deposited at an amplitude of 5 V and frequency of 100 Hz. In this frequency regime, electrophoresis[19] drives Au NP to the Si electrode surface. Au NP are functionalized with ligands having carboxylic functional

groups, where EDC/s-NHS is used for carbodiimide coupling to between carboxylic acid functional groups on ligands and amine-functionalized PMMA lamellar domains[20] as depicted in Fig. 2.1B. As a result, the surface is decorated with isolated Au NP serving as seeds for EHD flow (Fig. 2.2). After the deposition of Au NP seeds, a second deposition step is conducted at a frequency of 500 Hz. The presence of perturbations on Si electrode surface generates an electric field gradient activating EHD driven lateral assembly of NP, as shown schematically in Fig. 2.1C and experimentally in Fig. 2.2. Au NP in solution entrained in parallel EHD flow fields near NP seeds experience increased proximity with Au NP seeds anchored on the surface, thereby increasing the probability of cross-linking reactions between Au NP in solution and Au seeds on the surface as shown in Fig. 2.1D.

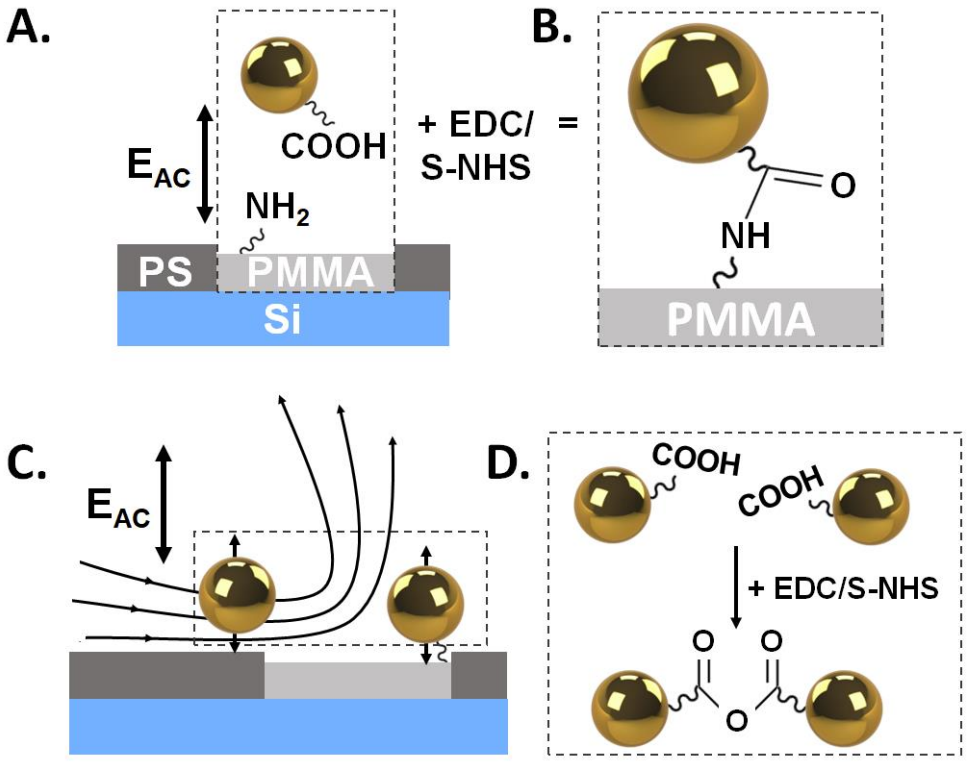

Figure 2.1. Schematic outlining fabrication of plasmonic nanoreactors. A) First, electrophoretic deposition of Au-LA NP seeds on electrodes composed of PS-b-PMMA thin films on Si. B) Carbodiimide crosslinking via EDC and S-NHS between carboxylic acid functional groups on ligands and on PMMA domains treated with ethylenediamine C) In the second deposition step, EHD flow produces a lateral driving force between NP in solution and Au seeds. D) The increased proximity between Au NP on the working electrode surface drives chemical reactions between Au NP in solution and Au seeds.

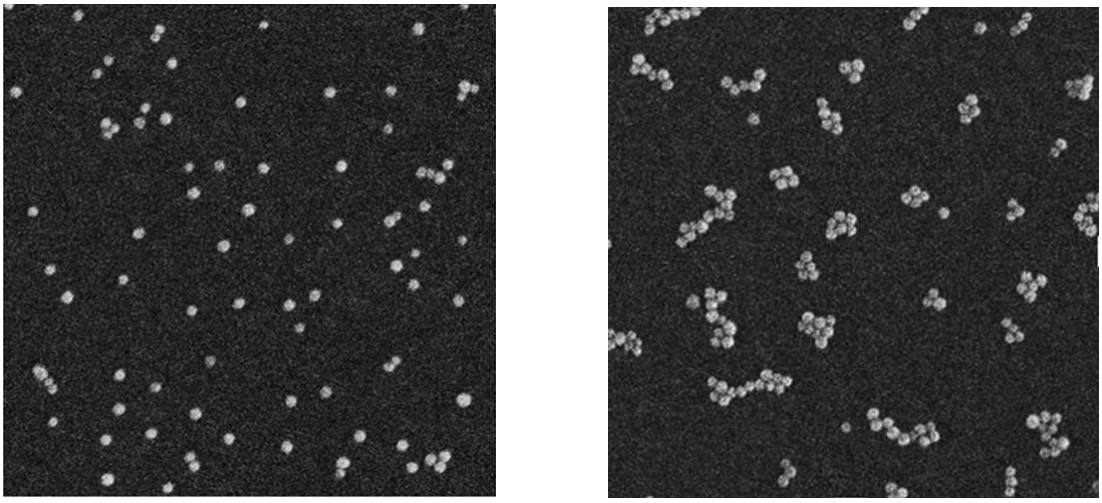

Figure 2.2. Left: SEM micrograph of 1st deposition step: Au-LA seeds electrophoretically deposited on PS-b-PMMA diblock copolymer surface. Right: SEM micrograph of 2nd deposition step: Au-LA NP laterally assembled into oligomer clusters via EHD flow.

In order to vary chemistry in plasmonic nanoreactors, we functionalized Au NP with mercaptobenzoic acid (MBA) ligands with carboxylic acid groups on different regions of the aromatic ring, 4MBA and 3MBA. The hydrolysis of benzoic anhydrides is over 3 orders of magnitude slower compared to that of acetic anhydrides,[21,22] providing a platform to probe how electronic structure of molecules affects reactivity. Charge delocalization due to aromatic rings in benzoic anhydride have been attributed to the stability.[23,24] The surface chemistry of Au NP was measured after functionalization with 4MBA and 3MBA using

photo-induced force microscopy (PiFM). PiFM is a recently developed scanning probe technique that measures localized dipole forces exerted on a nanoscale probe when molecules are excited by an IR excitation source which correlates to infrared absorption.[25] This technique is capable of simultaneously measuring sample topography and vibrational spectra with a spatial resolution below 6 nm on time scales of seconds.[26] PiFM also benefits from electromagnetic signal enhancements; even modest enhancements improve high signal to noise in PiFM as IR has an inherently high cross-section. At the junction of the Au tip and the Au sample surface, electromagnetic fields may be enhanced by factors between 50 and 130 due to the lightning rod effect and multi reflection process.[27,28] PiFM signal is proportional to the square of the electric field, allowing for monolayer detection sensitivity on Au substrates.[28] After functionalization, 10 μL of aqueous NP solution was dropcast on freshly prepared template stripped gold (TS-Au) and allowed to air-dry. The PiFM spectra taken from the Au NP surfaces (average of 10 points) is shown for Au-4MBA and Au-3MBA in Fig. 2.2A and 2.2C, respectively. Examination of the peaks in the spectral data shows they are consistent with IR resonances of the surface chemistry of NP surfaces and the Au coated AFM tip (Table 2.1, 2.2). Additionally, Fig. 2.2B and 2.2D show the average PiFM intensity from 3 line scans across NP with the IR excitation source fixed at specific wavenumbers of 1090 cm^{-1} and 1020 cm^{-1} for Au-4MBA and Au-3MBA, respectively. Both modes correspond to single bonded C-O stretching resonances from the carboxylate end groups. The dashed lines in Fig. 2.2A and 2.2C highlight the region between the two white asterisks in the inset. PiFM intensity clearly increases with respect to the background across the NP with variations likely attributed to the tip-sample distance and molecular

coverage. Overall, the increased signal on NP surfaces confirms functionalization of Au-4MBA and Au-3MBA.

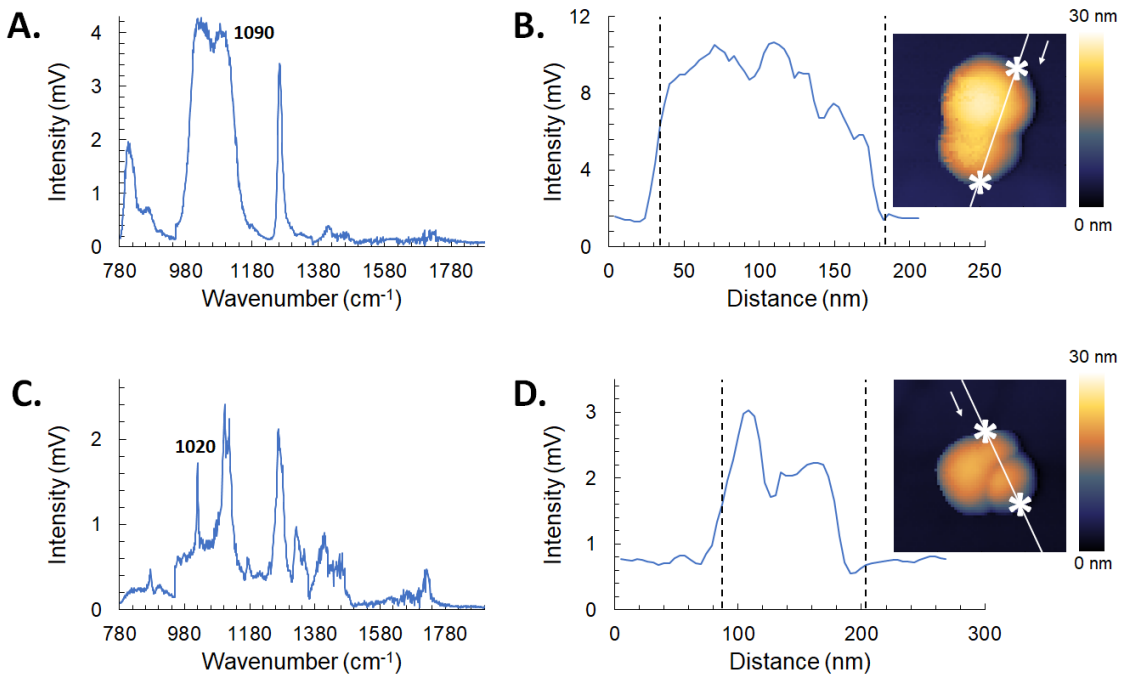

Figure 2.2. Average PiFM spectra (n=10) collected across the surface of A) Au-4MBA and C) Au-3MBA. Average PiFM spectral intensity (n=3) and across B) Au-4MBA at 1090 cm^{-1} and D) Au-3MBA at 1020 cm^{-1}. Insets show topography with a window size of 200 nm and height legend. The edges of the NP clusters are marked by white asterisks in insets and are represented by vertical dashed lines in B and D.

Table 2.1. Spectral Data and Vibrational Assignment of 4MBA

IR Frequency (cm^{-1})	4MBA Vibrational Assignment
875	Out-of plane C-O-H bend
1020	C-O stretch
1107	C-O stretch
1117	C-O stretch
1176	C-O stretch
1270	C-O stretch
1324	Aromatic C-C stretch
1410	In-plane C-O-H bend
1463	Aromatic ring stretch
1725	C=O stretch

Table 2.2. Spectral Data and Vibrational Assignment of 3MBA

IR Frequency (cm^{-1})	3MBA Vibrational Assignment
810	Out-of plane ring bend
875	Out-of plane C-O-H bend
1020	C-O stretch
1107	C-O stretch
1117	C-O stretch
1176	C-O stretch
1270	C-O stretch
1324	Aromatic C-C stretch
1410	In-plane C-O-H bend
1725	C=O stretch

During PiFM imaging, the mechanical forces exerted on the AFM tip are primarily sensitive to dipoles excited perpendicular to the surface. Analysis of the PiFM spectra of Fig. 2.2A and 2.2C shows that vibrational modes at 810 cm^{-1} are visible. These modes correlate to out-of-plane ring bending resonances of the benzene group, suggesting that the ligands have a relatively flat orientation against the Au surface. This is further supported by the lack of sharp peaks between 1350 and 1600 cm^{-1}, which typically belong to in-plane benzene ring modes. Single C-O stretching resonances are present in both Au-4MBA and Au-3MBA at 1265 cm^{-1}, while the region of the spectra between 1000 and 1100 cm^{-1} hosts contributions from C-O resonances as well. Typically, C=O stretching modes appear at high wavenumbers between 1700 and 1800 cm^{-1}. There are small peaks present in both spectra

in that region, suggesting that there are few C=O bonds. It is possible that carboxylic acid groups, which have C=O bonds, instead remain deprotonated as carboxylate anions. Carboxylate anions have C-O bonds that are stabilized by electron delocalization and are seen in experimental PiFM spectra.

2.3.2 Parsing molecular orientation in nanoreactors with DFT

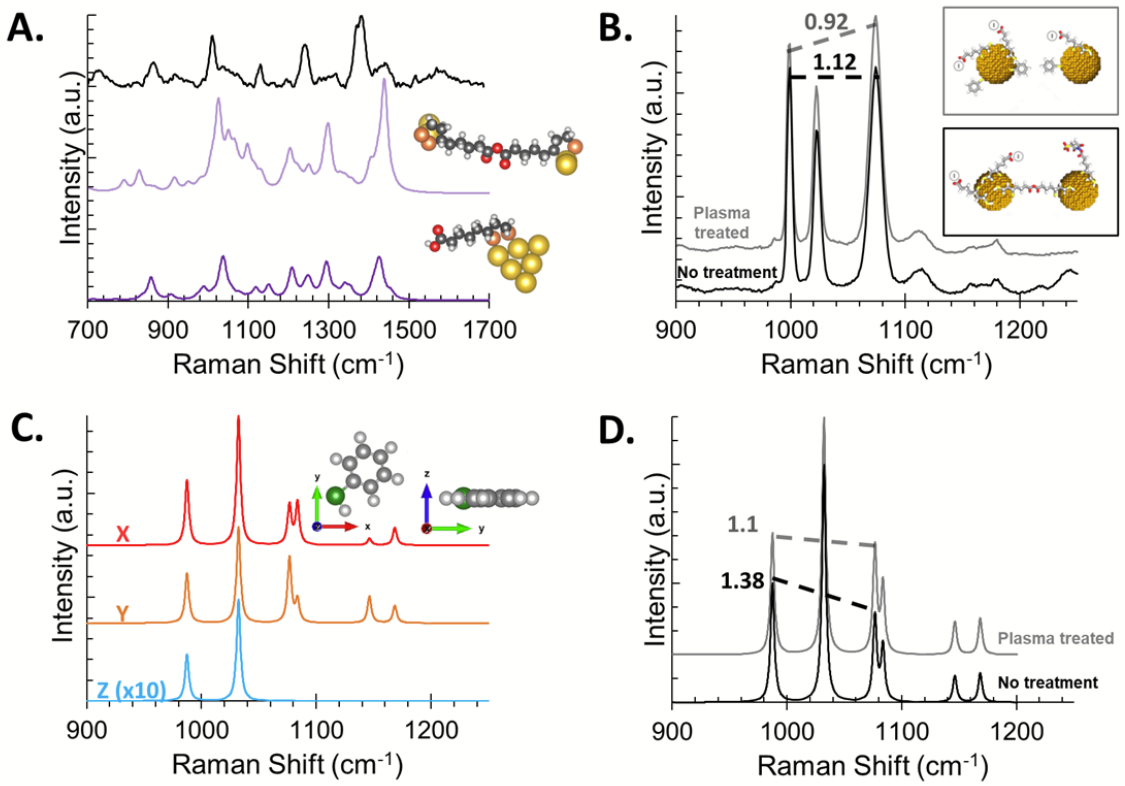

Figure 2.3. SERS spectra and electric-field induced nanogap reaction simulation. A) Experimental SERS spectra (black) of Au-LA nanoreactors. DFT simulated Raman spectra of unbonded LA ligands (dark purple) and ligands with acetic anhydride bond (light purple). Insets show relaxed geometries. B) Experimental SERS spectra of Au-LA assembled with EHD soaked overnight in 0.5 mM benzenethiol (BZT) in ethanol without (black, inset bottom) and with O_2 plasma treated to remove ligands (dashed gray, inset top). C) Plane-wave DFT calculations of gas-phase BZT with Cartesian X, Y, Z (red, orange, blue, respectively) components decomposed. As expected, the X and Y components (red, orange) are similar due to symmetry and the out of plane, Z component (blue, multiplied by 10) shows fewer modes.

Molecular orientation effects in nanogaps can be observed experimentally from EHD assemblies of nanoreactors. In Fig. 2.3A, simulations of crosslinked (light purple) and unbonded (dark purple) LA ligands are compared to experimental SERS spectra of Au-LA nanoreactors. A closer match to experimental SERS spectra is seen from the crosslinked LA simulation, agreeing with previous experimental and computational results that see the formation of an acetic anhydride bond using EDC carbodiimide coupling chemistry. Specifically, the peak at 1097 cm^{-1} (light purple) corresponds to the experimental peak at 1129 cm^{-1} (black), a coupled carbonyl bending mode resonance only present in the acetic anhydride compared to the unbonded lipoic acid (dark purple). As an alkane chain, Au-LA has a low Raman cross section, and yet has a clear SERS signal from the nanoreactors. Additionally, DFT simulations do not include the diblock copolymer electrode surface, which are too far outside the hotspot regions of the nanoreactors to significantly contribute to the background of SERS measurements. Au-LA nanogaps are treated with benzenethiol (BZT), a common Raman reporter, before and after O_2 plasma treatment to remove anhydride ligands in order to assess the effects of steric hindrance and molecular orientation in nanogaps. The peak ratio between the modes at 1000 cm^{-1} and 1075 cm^{-1} in Fig. 2.3B for samples with and without plasma treatment is 0.92 (dashed gray line) and 1.12 (black line), respectively. When comparing the spectral data with DFT simulated spectra of BZT, Fig. 2.3C, we gain information on molecular orientation. The increased intensity at 1075 cm^{-1} (not present in the z-component of the DFT calculations) after O_2 plasma treatment indicates BZT XY orientation more fully aligns with electric field polarization in nanogaps since the acetic anhydride bridge is removed during plasma treatment. This result confirms we can observe orientation effects in nanogaps even in

ensemble averages as we hypothesize the confined geometry and intense electromagnetic fields will influence orientation.

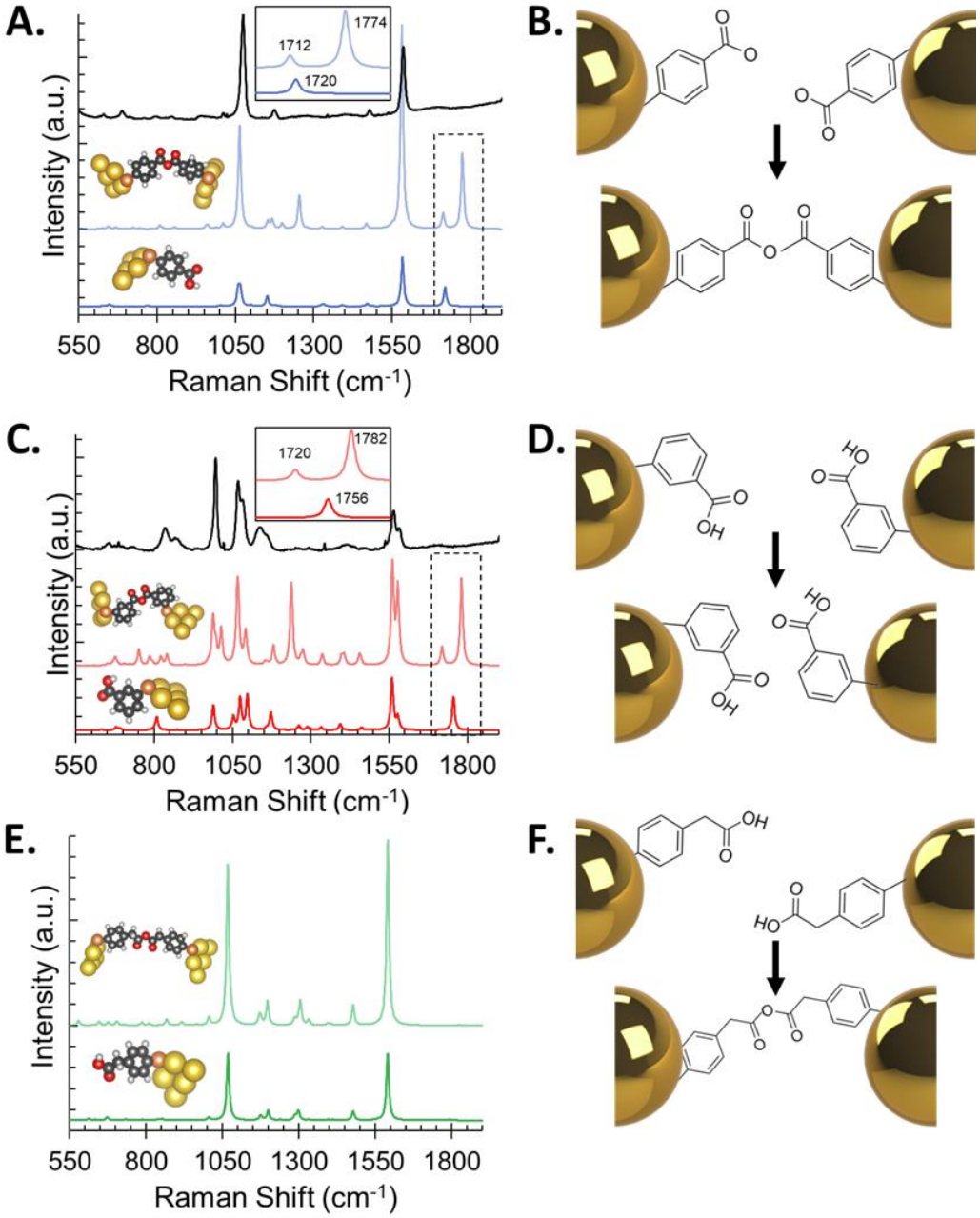

Figure 2.4. Experimental SERS spectra (black) of A) Au-4MBA and C) Au-3MBA coordinated to small Au clusters. DFT simulated spectra of unbonded (4MBA, 3MBA, MPAA) ligands (dark blue, dark red, dark green) and ligands with benzoic anhydride bond (light blue, light red, light green). Insets show an enlarged region of peaks highlighted by dashed boxes. Nanogap chemistry after EHD assembly: B) Au-4MBA and F) Au-MPAA hypothesized to form a benzoic anhydride and acetic anhydride bond, respectively. D) Schematic of hypothesis that Au-3-MBA are sterically hindered from forming benzoic anhydride.

After PiFM confirmed the successful functionalization of Au-4MBA and Au-3MBA, nanoreactors were assembled with EDC carbodiimide crosslinking chemistry for both mercaptobenzoic acid ligands. The nanogap chemistry of each nanoreactor was measured with surface enhanced Raman scattering (SERS) and compared to density functional theory (DFT) simulations of Raman spectra to probe the formation of anhydrides. DFT simulations are performed on the neutral benzoic acids. Au-4MBA and Au-3MBA have much higher signal-to-noise ratios in Fig. 2.4A and 2.4C, respectively, compared to Au-LA in Fig. 2.3A, due to the presence of benzene rings having a higher Raman cross section. In both cases, the simulated and experimental spectra correlate to a lack of anhydride bonds formed by Au-4MBA and Au-3MBA. The peak at 1720 cm^{-1} and 1756 cm^{-1}in the unbonded spectra of Au-4MBA and Au-3MBA (dark blue and dark red in Fig. 2.4A and 2.4C, respectively) belongs to a C=O stretching resonance. This mode is only present in neutral carboxylic acid groups. Since it is not visible in experimental spectra, this suggests that ligands on Au surfaces remain deprotonated as carboxylate anions after deposition. The Raman peaks at 1712 and 1774 cm^{-1} (light blue, Fig. 2.4A) and at 1720 and 1782 cm^{-1} (light red, Fig. 2.4C) are anhydride bending modes. Their absence in corresponding experimental spectra point to a lack of EDC carbodiimide crosslinking in the nanogap for Au-4MBA and Au-3MBA. In

the case of Au-3MBA, it is hypothesized that steric hindrance precludes the formation of a benzoic anhydride bond.

Having developed first principles methods for modeling Raman spectra of molecules on Au NP, additional calculations were carried out for another candidate ligand, mercaptophenylacetic acid (MPAA), to guide future experimental endeavors. Structurally, this ligand has an additional carbon atom between the benzene ring and the carboxylic acid group. In the event of successful crosslinking, the Au-MPAA anhydride bond formed would be longer and more acetic in character compared to the benzoic anhydrides of Au-4MBA and Au-3MBA, allowing for the investigation of steric hindrance and charge transfer on self-assembly behavior. Simulations of crosslinked (light green) and unbonded (dark green) LA ligands are compared to each other in Fig. 2.4E and found to be quite similar, with subtle differences at lower wavenumbers. There are several small anhydride resonance mode peaks between 550 and 1000 cm^{-1} that are not present in the unbonded MPAA spectra. As expected given their structural similarity, the simulated spectra of unbonded Au-MPAA (dark green) strongly resembles the experimental spectra of Au-4MBA in Fig. 2.4A (black). It is interesting to note that there is no peak in the 1720-1750 cm^{-1} wavenumber region for MPAA, while those peaks correspond to the C=O stretching resonance of the carboxylate group for 3MBA and 4MBA. This finding suggests the importance of proximity to the benzene ring on resonant mode frequencies. Computational methods developed here allow for the analysis of candidate ligands and identification of successful crosslinking signatures in experimental SERS spectra.

2.4 Conclusion

We have presented a versatile platform for the investigation of interfacial chemical reactions in self-assembled nanoreactors. The functionalization of Au NP with ligands chosen to have carboxylic acid end groups with varying chain lengths, aromaticity, and molecular orientation was confirmed with localized PiFM chemical mapping. Subsequent deposition of Au NP on patterned surfaces with EHD flow resulted in the formation of acetic anhydrides from Au-LA nanoreactors as confirmed by SERS and DFT calculations. Detailed molecular orientation of molecules in confined geometries can be deduced by DFT analysis of SERS spectra. Au-LA nanoreactors treated with common Raman reporter BZT that then underwent plasma cleaning to remove LA ligands show an intriguing shift in SERS peak ratios. Decomposing the Raman spectra of BZT along Cartesian coordinate directions demonstrates that contributions to these peak ratios originate from x-y planar benzene ring mode resonances. This suggests that as O_2 plasma cleaning removes LA ligands, BZT molecules have greater access to the nanoreactor gap. The strongly directional electromagnetic field in the gap coerces the planar benzene rings to be parallel in alignment. Linear combinations of Cartesian-decomposed Raman components selected to have greater contributions from x and y modes captures the peak ratio shift seen in experiment. The weighting of the z component correlates to a 54^o angle shift of BZT relative to the Au NP surface. Intriguingly, neither Au-4MBA nor Au-3MBA formed anhydride bridges, despite the propensity of benzoic acids to form anhydride bridges in solution.[12,22] Raman DFT calculations confirmed the lack of anhydride bonding and will guide selection of candidate ligands to investigate, such as MPAA. Future work will investigate the effects of steric hindrance and charge transfer on anhydride bond formation in mercaptobenzoic

acid ligands. Altogether, the EHD driven self-assembly of nanoreactors with tunable surface chemistry and the development of DFT simulation methods to interpret SERS spectra is greatly extensible for the nanoscale investigation of other interfacial chemical systems.

2.5 References

(1) Panoiu, N. C.; Sha, W. E. I.; Lei, D. Y.; Li, G.-C. Nonlinear Optics in Plasmonic Nanostructures. *J. Opt.* **2018**, *20* (8), 083001. https://doi.org/10.1088/2040-8986/aac8ed.

(2) Brongersma, M. L.; Halas, N. J.; Nordlander, P. Plasmon-Induced Hot Carrier Science and Technology. *Nat. Nanotechnol.* **2015**, *10* (1), 25–34. https://doi.org/10.1038/nnano.2014.311.

(3) Gargiulo, J.; Berté, R.; Li, Y.; Maier, S. A.; Cortés, E. From Optical to Chemical Hot Spots in Plasmonics. *Acc. Chem. Res.* **2019**, *52* (9), 2525–2535. https://doi.org/10.1021/acs.accounts.9b00234.

(4) Kim, N.; Thomas, M. R.; Bergholt, M. S.; Pence, I. J.; Seong, H.; Charchar, P.; Todorova, N.; Nagelkerke, A.; Belessiotis-Richards, A.; Payne, D. J.; Gelmi, A.; Yarovsky, I.; Stevens, M. M. Surface Enhanced Raman Scattering Artificial Nose for High Dimensionality Fingerprinting. *Nat. Commun.* **2020**, *11* (1), 207. https://doi.org/10.1038/s41467-019-13615-2.

(5) Nam, J.-M.; Oh, J.-W.; Lee, H.; Suh, Y. D. Plasmonic Nanogap-Enhanced Raman Scattering with Nanoparticles. *Acc. Chem. Res.* **2016**, *49* (12), 2746–2755. https://doi.org/10.1021/acs.accounts.6b00409.

(6) Lee, J.-H.; Nam, J.-M.; Jeon, K.-S.; Lim, D.-K.; Kim, H.; Kwon, S.; Lee, H.; Suh, Y. D. Tuning and Maximizing the Single-Molecule Surface-Enhanced Raman Scattering from DNA-Tethered Nanodumbbells. *ACS Nano* **2012**, *6* (11), 9574–9584. https://doi.org/10.1021/nn3028216.

(7) de Nijs, B.; Benz, F.; Barrow, S. J.; Sigle, D. O.; Chikkaraddy, R.; Palma, A.; Carnegie, C.; Kamp, M.; Sundararaman, R.; Narang, P.; Scherman, O. A.; Baumberg, J. J. Plasmonic Tunnel Junctions for Single-Molecule Redox Chemistry. *Nat. Commun.* **2017**, *8* (1), 994. https://doi.org/10.1038/s41467-017-00819-7.

(8) Thrift, W. J.; Ragan, R. Quantification of Analyte Concentration in the Single Molecule Regime Using Convolutional Neural Networks. *Anal. Chem.* **2019**, *91* (21), 13337–13342. https://doi.org/10.1021/acs.analchem.9b03599.

(9) Adams, S. M.; Campione, S.; Capolino, F.; Ragan, R. Directing Cluster Formation of Au Nanoparticles from Colloidal Solution. *Langmuir* **2013**, *29* (13), 4242–4251. https://doi.org/10.1021/la3051719.

(10) Thrift, W. J.; Nguyen, C. Q.; Darvishzadeh-Varcheie, M.; Zare, S.; Sharac, N.; Sanderson, R. N.; Dupper, T. J.; Hochbaum, A. I.; Capolino, F.; Abdolhosseini Qomi, M. J.; Ragan, R. Driving Chemical Reactions in Plasmonic Nanogaps with Electrohydrodynamic Flow. *ACS Nano* **2017**, *11* (11), 11317–11329. https://doi.org/10.1021/acsnano.7b05815.

(11) Esteban, R.; Borisov, A. G.; Nordlander, P.; Aizpurua, J. Bridging Quantum and Classical Plasmonics with a Quantum-Corrected Model. *Nat. Commun.* **2012**, *3* (1), 825. https://doi.org/10.1038/ncomms1806.

(12) Kariyawasam, L. S.; Hartley, C. S. Dissipative Assembly of Aqueous Carboxylic Acid Anhydrides Fueled by Carbodiimides. *J. Am. Chem. Soc.* **2017**, *139* (34), 11949–11955. https://doi.org/10.1021/jacs.7b06099.

(13) Lomant, A. J.; Fairbanks, G. Chemical Probes of Extended Biological Structures: Synthesis and Properties of the Cleavable Protein Cross-Linking Reagent [35S]Dithiobis(Succinimidyl Propionate). *J. Mol. Biol.* **1976**, *104* (1), 243–261. https://doi.org/10.1016/0022-2836(76)90011-5.

(14) Borsley, S.; Leigh, D. A.; Roberts, B. M. W. A Doubly Kinetically-Gated Information Ratchet Autonomously Driven by Carbodiimide Hydration. *J. Am. Chem. Soc.* **2021**, *143* (11), 4414–4420. https://doi.org/10.1021/jacs.1c01172.

(15) Nie, Y.; Wang, P.; Du, H.; Meng, W.; Yang, J. An Efficient Strategy for Achieving Controlled Ring-Opening Polymerization of O -Carboxyanhydrides via Amine Initiation in Collaboration with Metal-Alkoxide Catalysis. *Polym. Chem.* **2018**, *9* (40), 5014–5023. https://doi.org/10.1039/C8PY01090K.

(16) Trau, M.; Saville, D. A.; Aksay, I. A. Assembly of Colloidal Crystals at Electrode Interfaces. *Langmuir* **1997**, *13* (24), 6375–6381. https://doi.org/10.1021/la970568u.

(17) Ristenpart, W. D.; Aksay, I. A.; Saville, D. A. Assembly of Colloidal Aggregates by Electrohydrodynamic Flow: Kinetic Experiments and Scaling Analysis. *Phys. Rev. E* **2004**, *69* (2). https://doi.org/10.1103/PhysRevE.69.021405.

(18) Goel, M.; Singh, A.; Bhola, A.; Gupta, S. Size-Tunable Assembly of Gold Nanoparticles Using Competitive AC Electrokinetics. *Langmuir* **2019**, *35* (24). https://doi.org/10.1021/acs.langmuir.8b03963.

(19) Ferrick, A.; Wang, M.; Woehl, T. J. Direct Visualization of Planar Assembly of Plasmonic Nanoparticles Adjacent to Electrodes in Oscillatory Electric Fields. *Langmuir* **2018**, *34* (21), 6237–6248. https://doi.org/10.1021/acs.langmuir.8b00992.

(20) Choi, J. H.; Adams, S. M.; Ragan, R. Design of a Versatile Chemical Assembly Method for Patterning Colloidal Nanoparticles. *Nanotechnology* **2009**, *20* (6), 065301. https://doi.org/10.1088/0957-4484/20/6/065301.

(21) Bunton, C. A.; Fuller, N. A.; Perry, S. G.; Shiner, V. J. 542. The Hydrolysis of Carboxylic Anhydrides. Part III. Reactions in Initially Neutral Solution. *J. Chem. Soc. Resumed* **1963**, No. 0, 2918–2926. https://doi.org/10.1039/JR9630002918.

(22) Kariyawasam, L. S.; Kron, J. C.; Jiang, R.; Sommer, A. J.; Hartley, C. S. Structure–Property Effects in the Generation of Transient Aqueous Benzoic Acid Anhydrides by Carbodiimide Fuels. *J. Org. Chem.* **2020**, *85* (2), 682–690. https://doi.org/10.1021/acs.joc.9b02746.

(23) Bunton, C. A.; Fendler, J. H. The Hydrolysis of Carboxylic Anhydrides. VII.1,2 Electrolyte Effects on the Acid Hydrolysis. *J. Org. Chem.* **1966**, *31* (11), 3764–3771. https://doi.org/10.1021/jo01349a064.

(24) Shiina, I.; Kubota, M.; Oshiumi, H.; Hashizume, M. An Effective Use of Benzoic Anhydride and Its Derivatives for the Synthesis of Carboxylic Esters and Lactones: A Powerful and Convenient Mixed Anhydride Method Promoted by Basic Catalysts. *J. Org. Chem.* **2004**, *69* (6), 1822–1830. https://doi.org/10.1021/jo030367x.

(25) Nowak, D.; Morrison, W.; Wickramasinghe, H. K.; Jahng, J.; Potma, E.; Wan, L.; Ruiz, R.; Albrecht, T. R.; Schmidt, K.; Frommer, J.; Sanders, D. P.; Park, S. Nanoscale Chemical Imaging by Photoinduced Force Microscopy. *Sci. Adv.* **2016**, *2* (3), e1501571. https://doi.org/10.1126/sciadv.1501571.

(26) Almajhadi, M. A.; Uddin, S. M. A.; Wickramasinghe, H. K. Observation of Nanoscale Opto-Mechanical Molecular Damping as the Origin of Spectroscopic Contrast in Photo Induced Force Microscopy. *Nat. Commun.* **2020**, *11* (1), 5691. https://doi.org/10.1038/s41467-020-19067-3.

(27) Roth, R. M.; Panoiu, N. C.; Adams, M. M.; Osgood, R. M.; Neacsu, C. C.; Raschke, M. B. Resonant-Plasmon Field Enhancement from Asymmetrically Illuminated Conical Metallic-Probe Tips. *Opt. Express* **2006**, *14* (7), 2921–2931. https://doi.org/10.1364/OE.14.002921.

(28) Li, J.; Jahng, J.; Pang, J.; Morrison, W.; Li, J.; Lee, E. S.; Xu, J.-J.; Chen, H.-Y.; Xia, X.-H. Tip-Enhanced Infrared Imaging with Sub-10 Nm Resolution and Hypersensitivity. *J. Phys. Chem. Lett.* **2020**, *11* (5), 1697–1701. https://doi.org/10.1021/acs.jpclett.0c00129.

(29) Savitzky, Abraham.; Golay, M. J. E. Smoothing and Differentiation of Data by Simplified Least Squares Procedures. *Anal. Chem.* **1964**, *36* (8), 1627–1639. https://doi.org/10.1021/ac60214a047.

(30) Eilers, P.; Boelens, H. Baseline Correction with Asymmetric Least Squares Smoothing., 2005.

(31) Wang, X.; Shindel, M. M.; Wang, S.-W.; Ragan, R. A Facile Approach for Assembling Lipid Bilayer Membranes on Template-Stripped Gold. *Langmuir* **2010**, *26* (23), 18239–18245. https://doi.org/10.1021/la102774n.

(32) M. J. Frisch, G. W. Trucks, H. B. Schlegel, G. E. Scuseria, M. A. Robb, J. R. Cheeseman, G. Scalmani, V. Barone, G. A. Petersson, H. Nakatsuji, X. Li, M. Caricato, A. V. Marenich, J. Bloino, B. G. Janesko, R. Gomperts, B. Mennucci, H. P. Hratchian, J. V. Ortiz, A. F. Izmaylov, J. L. Sonnenberg, D. Williams-Young, F. Ding, F. Lipparini, F. Egidi, J. Goings, B. Peng, A. Petrone, T. Henderson, D. Ranasinghe, V. G. Zakrzewski, J. Gao, N. Rega, G. Zheng, W. Liang, M. Hada, M. Ehara, K. Toyota, R. Fukuda, J. Hasegawa, M. Ishida, T. Nakajima, Y. Honda, O. Kitao, H. Nakai, T. Vreven, K. Throssell, J. A. Montgomery, Jr., J. E. Peralta, F. Ogliaro, M. J. Bearpark, J. J. Heyd, E. N. Brothers, K. N. Kudin, V. N. Staroverov, T. A. Keith, R. Kobayashi, J. Normand, K. Raghavachari, A. P. Rendell, J. C. Burant, S. S. Iyengar, J. Tomasi, M. Cossi, J. M. Millam, M. Klene, C. Adamo, R. Cammi, J. W. Ochterski, R. L. Martin, K. Morokuma, O. Farkas, J. B. Foresman, D. J. Fox. Gaussian 16, 2016.

(33) Kresse, G.; Furthmüller, J. Efficiency of Ab-Initio Total Energy Calculations for Metals and Semiconductors Using a Plane-Wave Basis Set. *Comput. Mater. Sci.* **1996**, *6* (1), 15–50. https://doi.org/10.1016/0927-0256(96)00008-0.

(34) Kresse, G.; Furthmüller, J. Efficient Iterative Schemes for Ab Initio Total-Energy Calculations Using a Plane-Wave Basis Set. *Phys. Rev. B* **1996**, *54* (16), 11169–11186. https://doi.org/10.1103/PhysRevB.54.11169.

(35) Perdew, J. P.; Burke, K.; Wang, Y. Generalized Gradient Approximation for the Exchange-Correlation Hole of a Many-Electron System. *Phys. Rev. B* **1996**, *54* (23), 16533–16539. https://doi.org/10.1103/PhysRevB.54.16533.

(36) Hay, P. J.; Wadt, W. R. Ab Initio Effective Core Potentials for Molecular Calculations. Potentials for the Transition Metal Atoms Sc to Hg. *J. Chem. Phys.* **1985**, *82* (1), 270–283. https://doi.org/10.1063/1.448799.

(37) Merlen, A.; Chaigneau, M.; Coussan, S. Vibrational Modes of Aminothiophenol: A TERS and DFT Study. *Phys. Chem. Chem. Phys.* **2015**, *17* (29), 19134–19138. https://doi.org/10.1039/C5CP01579K.

(38) Sun, M.; Huang, Y.; Xia, L.; Chen, X.; Xu, H. The PH-Controlled Plasmon-Assisted Surface Photocatalysis Reaction of 4-Aminothiophenol to p,P′-Dimercaptoazobenzene on Au, Ag, and Cu Colloids. *J. Phys. Chem. C* **2011**, *115* (19), 9629–9636. https://doi.org/10.1021/jp201002v.

(39) Gajdoš, M.; Hummer, K.; Kresse, G.; Furthmüller, J.; Bechstedt, F. Linear Optical Properties in the Projector-Augmented Wave Methodology. *Phys. Rev. B* **2006**, *73* (4), 045112. https://doi.org/10.1103/PhysRevB.73.045112.

(40) Vasp_raman.Py, 2022. https://github.com/raman-sc/VASP (accessed 2022-12-15).

(41) Boekhoven, J.; Hendriksen, W. E.; Koper, G. J. M.; Eelkema, R.; van Esch, J. H. Transient Assembly of Active Materials Fueled by a Chemical Reaction. *Science* **2015**, *349* (6252), 1075–1079. https://doi.org/10.1126/science.aac6103.

(42) Tena-Solsona, M.; Rieß, B.; Grötsch, R. K.; Löhrer, F. C.; Wanzke, C.; Käsdorf, B.; Bausch, A. R.; Müller-Buschbaum, P.; Lieleg, O.; Boekhoven, J. Non-Equilibrium Dissipative Supramolecular Materials with a Tunable Lifetime. *Nat. Commun.* **2017**, *8* (1), 15895. https://doi.org/10.1038/ncomms15895.

CHAPTER 3: CHARGE TRANSFER AND ELECTROMAGNETIC FIELDS AT NANOPARTICLE-LIGAND INTERFACES

3.1 Introduction

The ability to fabricate nanoscale metallic structures with feature sizes far below the diffraction limit of visible light has ushered in the ability to concentrate and manipulate optical signals for a wide range of applications including optoelectronics,[1] photocatalysis,[2,3] and biological sensing.[4,5] The efficiency of these nonlinear optical processes depends strongly on the degree of confinement[6] and proximity of molecules in the local environment. Efforts to probe chemical behavior spectroscopically are challenging due to the sensitivity between molecular orientation, charge transfer, and electromagnetic fields in confined geometries leading to complex variations in vibrational spectroscopic signals. Synergistic experimental and first principles computational approaches are necessary to provide understanding of the dynamic responses of chemical reactions in confined geometries.

Scanning probe techniques are capable of high spatial resolution and recent innovations have led to the development of simultaneous topographic and local chemical mapping through coupling between scanning probe tip and sample surface through an external excitation source. Tip-enhanced Raman spectroscopy (TERS) and scattering-type scanning near-field optical microscopy (s-SNOM) are capable of <10 nm resolution in ambient conditions; both methodologies rely on scattered optical signals collected by a spectrometer, which can introduce significant background signal from far-field scattered photons.[7] Photo-induced force microscopy (PiFM), a recently developed technique,[8] detects mechanical deflections arising from dipole-

dipole interactions between an optically driven molecule and its mirror image dipole in the gold coated AFM tip. By utilizing both near-field excitation and near-field detection, PiFM is not susceptible to far-field background.[8] Additionally, PiFM is capable of simultaneously measuring topography and chemical signals with a spatial resolution below 6 nm on time scales of seconds.[9] Analysis of self-assembled monolayers on gold surfaces with PiFM show correlation with infrared spectral data.[10] However, the experimentally collected PiFM spectra does not directly map with IR spectra. Thus correlating with molecular structure is challenging with less well-ordered surfaces and necessitates computational simulations to interpret, considering that the AFM probe is more sensitive to vibrations perpendicular to the scanning surface and signatures of strong light-matter interactions may manifest in tip-sample junctions.[11]

In this work, we investigate experimental PiFM measurements of benzenedithiol (BDT) on Au NP surfaces and compare with density functional theory simulations of IR spectra to understand how PiFM data can inform on the influence of molecular orientation and the local electromagnetic environment in nanoconfined geometries. Electric fields alone are not sufficient to explain enhancement of PiFM spectra. We show that electric fields acting jointly with significant charge transfer provided by Au surfaces are capable of driving the diffusion of Au atoms, rotation of functional groups, and large shifts in bonding angle that are all reflected in PiFM spectra. Additionally, in the case of Au atom diffusion that leads to the creation of a local tip-like perturbation, large enhancements are seen in PiFM spectra.

3.2 Materials and Methods

Materials. 40 nm diameter gold nanospheres were purchased from Nanocomposix. Ge(111) wafers with a resistivity of >50 Ω·cm were purchased from University Wafer Inc (South Boston, MA). Isopropyl alcohol (IPA), sodium bicarbonate, and sodium carbonate were purchased from Fisher Scientific. Ethanol was purchased from Gold Shield Distributors, Inc. 1,4-Benzenedithiol (BDT) was purchased from Tokyo Chemical Industry. 2,2'-Dithiodipyridine (DTDP) was purchased from Chem-Implex International Inc. Dithiothreitol (DTT) was purchased from PanReac AppliChem ITW Reagents Nanopure deionized (DI) water (18.2 MΩ cm-1) was obtained from a Milli-Q Millipore System.

Gold Nanoparticle Surface Functionalization. To modify the AuNPs with BDT (Au@BDT), 25 mL of the 40 nm AuNPs (2 mM sodium citrate) stock solution (0.05 mg/mL) was centrifuged for 30 min at 1.7 rcf and the original solvent was removed. The solution was resuspended in 25 mL of the (1 mM, pH 10.6) sodium bicarbonate buffer (95%) and ethanol (5%) (23.75 mL of buffer to 1.25 mL of ethanol) with 4.5 mg of BDT to produce 25 mL BDT in AuNPs solution (100:1 molecules/surface gold atoms). The solution was kept overnight at room temperature in the dark. Finally, the obtained solution was centrifuged 3x for 30 min at 1.7 rcf to remove the excess of BDT and was dispersed in 2.5 mL of 1mM buffer-ethanol solution to produce 10x concentrated Au@BDT.

Photoinduced Force Microscopy (PiFM) Characterization. Silicon wafers were purchased from University Wafer. EPO-TEK H21D, two-component epoxy glue, was purchased from Epoxy Technology, Inc., and was used for fabricating template stripped Au (TS-Au) surfaces. Samples

for PiFM characterization were produced by drop casting solutions of Au-BDT NP on TS-Au, fabricated following a previously published procedure.[16] Briefly, TS-Au was prepared by gluing gold surfaces with EPO-TEK H21D to silicon substrates, forming a sandwich structure, and cured at 150 °C for 30 mins. After cooling, silicon templates were detached from silicon substrates to expose a TS-Au film with a root-mean-square roughness less than 0.3 nm over 1 μm × 1 μm as evaluated by AFM. TS-Au films used as substrates for PiFM were used immediately after stripping to maintain a pristine surface for sample deposition. Prepared samples were air-dried and then within minutes were scanned in non-contact mode with a commercial VistaScope atomic force microscope (MolecularVista Inc). The system includes vibration isolation equipment, an acoustic enclosure, and is connected to a clean dry air system to minimize water vapor for IR measurements. A quantum cascade laser system (Block Engineering) with a tuning range from 780 to 1900 cm^{-1} provided IR excitation with a wavenumber resolution of 1 cm^{-1}. The cantilever type was NCH-Au from MolecularVista with a nominal tip radius of 20 nm and 300 kHz resonance. The cantilever was excited at its second resonance around 1.69 MHz for surface-sensitive PiFM sideband difference mode measurements.

IR/Raman Spectral Simulations. Density functional theory (DFT) calculations of Raman spectra were carried out in atomic orbital basis sets with Gaussian16[17] while plane-wave calculations utilized the Vienna ab-initio Software Package (VASP).[18,19] Gaussian16 cluster geometry optimizations and vibrational frequency calculations of Au-BDT were performed with a generalized gradient approximation (GGA), specifically the PW91 exchange correlation functional.[20] All atoms were defined with the 6-311+G(2d,p) basis set except for Au, which utilized the LANL2DZ basis set and effective core potential.[21] These mixed basis sets combined

with the PW91 functional have been shown in previous works to accurately model the Raman spectra of similar organic molecules adsorbed to gold.[22,23]

Plane-wave DFT calculations of Au surfaces were performed using VASP and used the projector augmented wave pseudopotentials and the Perdew–Burke–Ernzerhof gradient approximation with an energy cutoff of 400 eV. Gold(111) surface slabs were constructed with four layers in a 3 x √3 unit cell and 25Å vacuum spacing. Long-range dispersion interactions were included with Grimme's DFT-D3 method with Becke-Johnson damping.[24] Structural relaxations were performed with energy convergences of 10^{-9} eV and tight force convergences of 0.0005 eV/Å. For structural relaxations, the bottom two layers were fixed while the top two layers were allowed to fully relax. Reciprocal space was sampled with a 9 × 4 × 1 gamma centered Monkhorst–Pack grid[25] and a Gaussian smearing of 0.1 eV. Polarizability tensors for each mass-weighted vibrational mode in the forward and reverse directions will be calculated with density functional perturbation theory.[26] Raman scattering activities were found via the derivative of each polarizability tensor with respect to its corresponding vibrational mode, as implemented in the raman-sc package on GitHub.[27] This code was extended to handle frozen atoms as well as Cartesian decomposition of Raman spectra in VASP and will be made publicly available.

3.3 Results and Discussion

3.3.1 Localized chemical mapping of BDT functionalized Au NP

The PiFM experimental setup is summarized in Fig. 3.1a where we form a near-field optical cavity between the scanning probe microscope (SPM) tip and Au NP surface. Samples are prepared by drop casting 10 µL of aqueous Au NP functionalized with BDT (Au-BDT) on

freshly prepared template stripped gold (TS-Au) and allowed to air-dry. A continuous wave IR laser is used as the excitation source, optically driving a dipole response in BDT molecules between the Au coated SPM tip and Au NP surface. Only resonance modes of BDT that have a component perpendicular to the surface (defined here as z) cause mechanical deflections in the SPM cantilever that can be detected with PiFM. PiFM benefits from electromagnetic signal enhancements when using a Au coated SPM tip and a plasmonic surface. Specifically, at the junction of the Au tip and the Au sample surface, electromagnetic fields can be enhanced by factors between 50 and 130 due to the lightning rod effect and multi-reflection process.[10,12] While IR has an inherently high cross-section, these electromagnetic signal enhancements improve signal to noise in PiFM when examining monolayers and sub-monolayer coverage of molecules. PiFM signal is proportional to the square of the electric field, and has previously reported monolayer detection sensitivity on Au substrates.[10] With first principles modeling, complementary information on molecular structure and electric field effects in PiFM are elucidated for the first time. The ability for localized chemical mapping of Au-BDT NP with PiFM is demonstrated in Fig. 3.1b, which shows the average PiFM intensity from 3 line scans across NP with the IR excitation source fixed at 1470 cm^{-1}, which corresponds to an aromatic C-C stretching mode. The dashed lines in Fig. 3.1b correspond to regions between the two white asterisks in the inset. PiFM intensity clearly increases with respect to the background across the NP with variations likely attributed to the tip-sample distance, molecular coverage, and nanoparticle surface geometry. Overall, the increased signal on NP surfaces confirms functionalization of Au-BDT.

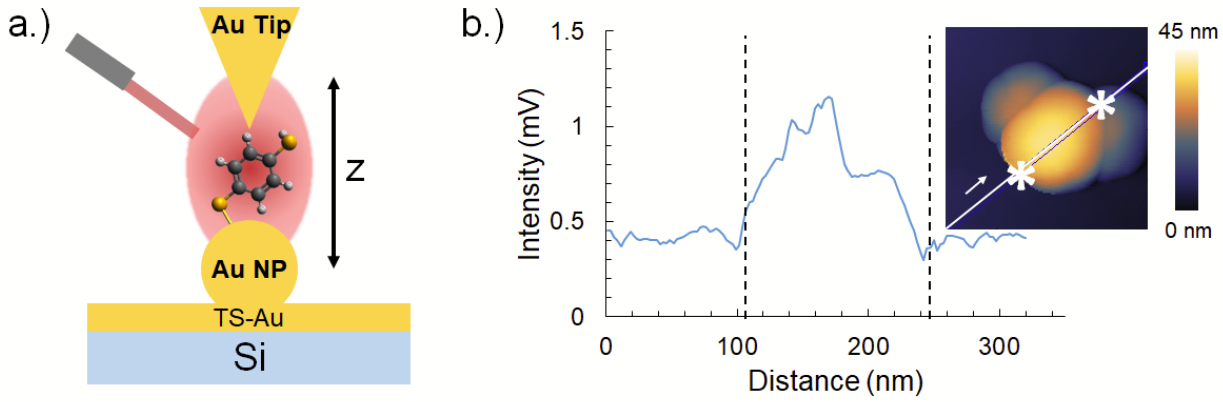

Figure 3.1. a) Schematic of tip-sample junction in PiFM experiments and excited with IR light source. Solutions of Au-BDT are deposited on freshly prepared TS-Au surfaces by drop casting. b) Average PiFM spectral intensity (n=3) across Au-BDT at 1470 cm^{-1}. Inset shows topography with height legend with a window size of 200 nm. The edges of the NP clusters are marked by white asterisks in insets and are represented by vertical dashed lines in B. White arrow indicates the line scan direction from low to high.

Experimental PiFM spectra collected from the surface of Au-BDT NP are compared with DFT simulations in Fig. 3.2. As the samples are allowed to dry in air over several minutes, it is first necessary to perform IR simulations of different potential thiolate oxidation states, shown in Fig. 2a for five possible states. All BDT molecules are coordinated to 5 Au atoms in these simulations. The oxidation states of SOH (light blue), SOO (dark blue), and SOOH (light purple) do not correlate well to experiment (black). The best overall match is seen between SH (light green) and experiment (black). These oxidation states are also more likely since sequential oxidation of thiol groups takes place in time periods over 24 hours.[13] The sharp peak at 1010 cm^{-1} in experimental spectra is missing from SH, but is likely an SO stretching resonance which is captured in simulations (dark green). This suggests that most BDT molecules contain a thiol end

group, with some oxidizing to a sulfoxide during sample preparation and subsequent PiFM measurement in ambient conditions.

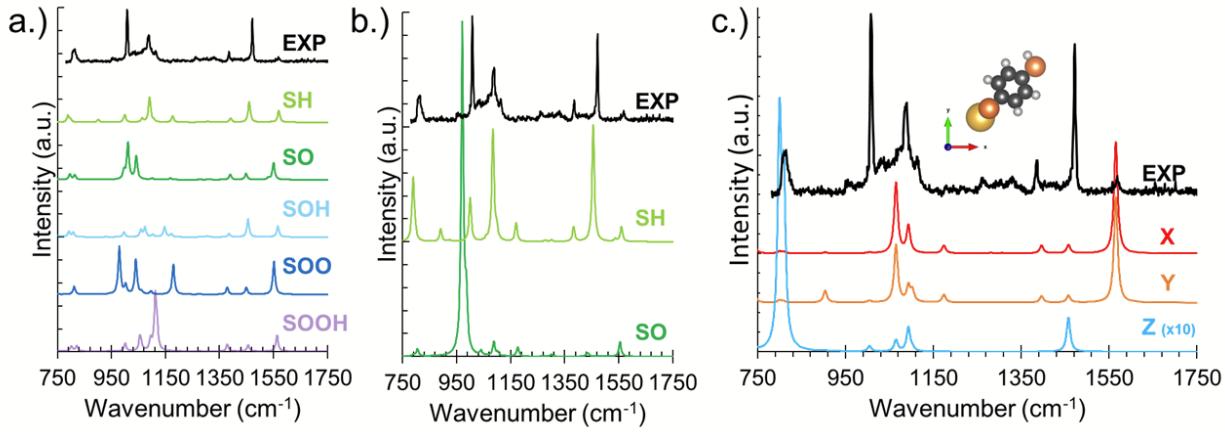

Figure 2. Average PiFM spectra (n=10) collected across the surface of Au-BDT (black) compared with simulated IR spectra of a) varying oxidation states of BDT coordinated to 5 Au atoms (Au_5-BDT), b) SH and SO oxidation states of Au_{20}-BDT with an applied electric field of +0.005 au, and c) plane wave DFT calculations of Au_1-BDT with Cartesian X, Y, Z (red, orange, blue, respectively) components of IR spectra decomposed. Z component is multiplied by a factor of 10 to aid visibility. Inset shows relaxed geometry.

Having identified the two most likely oxidation states, further calculations are performed with the SH end group on larger Au_{20}-BDT with an applied electric field of +0.005 au in the z direction, defined to be perpendicular to the cluster surface, which is constructed to be Au(111). In atomic units, 1 au = 51.4 V/Å. In order to better simulate the experimental system, Au_{20} clusters are utilized to understand charge transfer and electromagnetic field contributions to spectral data. The bottom two layers in Au_{20}-BDT are fixed in place to prevent rotation of the Au cluster from applied electric fields. By simulating BDT coordinated to a larger cluster, the interactions of bonding with a surface are reflected in calculated IR spectra of BDT with SH

(light green) and SO (dark green) end groups, shown in Fig. 3.2b. In turn, the applied electric field along the z axis selectively enhances resonance modes in correspondence with experiment. The SO stretching resonance is so strong in this regime that it dominates the calculated spectra of this oxidation state (dark green) and is likely the source of the sharp 1010 cm^{-1} peak in experimental spectra (black), further corroboration of the hypothesis that most BDT molecules have SH end groups with contributions from SO. Additionally, the three sharp peaks between 1350 and 1550 cm^{-1} are in-plane benzene ring stretching modes. There is excellent correspondence between these modes in experimental spectra (black) and SH simulated IR spectra (light green).

Two extraneous peaks seen in SH spectra that are not visible in experimental spectra prompted additional calculations. The two modes are shown in Fig. 3.2b: an SH bending mode at 893 cm^{-1} and an aromatic CH bending mode at 1171 cm^{-1} (light green). Plane-wave DFT calculations of Au_1-BDT with no applied electric field were carried out in VASP. The IR spectra of Au_1-BDT was decomposed along Cartesian coordinate axes as defined by the inset of Fig. 3.2c, where the x and y axes align with the plane of the benzene ring. The SH and aromatic CH bending modes are not present in the z oriented IR simulation (blue), suggesting that while these resonance modes are not hindered by the Au surface, they are not detected by the PiFM cantilever which is only sensitive to perpendicular perturbations. Such selectivity allows us to discern molecular orientation and further quantify the effects of electric fields and charge transfer on light-matter interactions.

3.3.2 First principles approach to probe effects of molecular orientation, electric field, and charge transfer on IR spectra

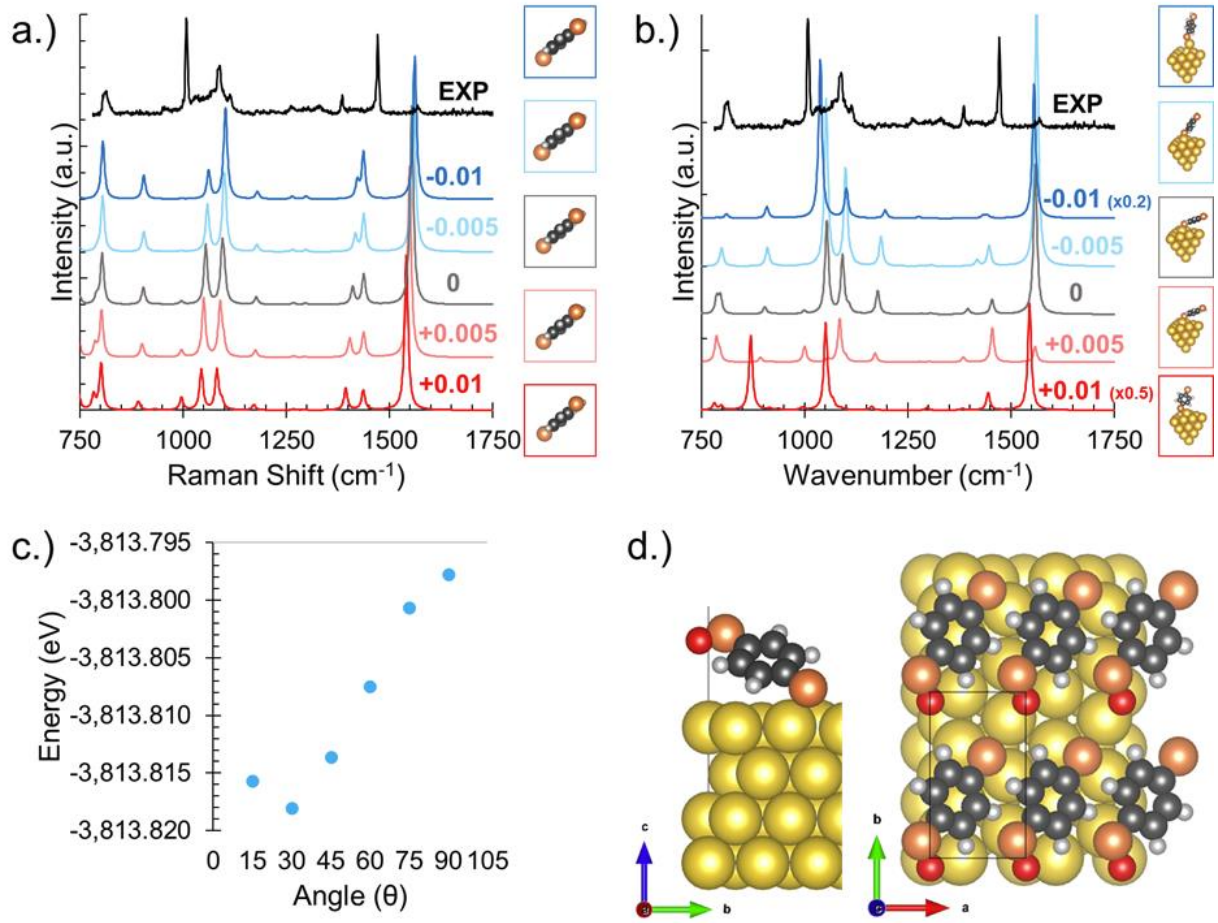

Figure 3.3. Average PiFM spectra (n=10) collected across the surface of Au-BDT (black) compared with simulated IR spectra of varying applied electric field strengths applied to a) uncoordinated BDT and b) Au_{20}-BDT. Oxidation state is SH. Insets show relaxed geometries where border color corresponds to each applied field strength. c) Single point DFT energy calculations of Au_{20}-BDT as a function of varying bond angle. d) Relaxed geometry of plane wave DFT calculations of Au-BDT on a Au(111) surface. Bonding angle is 29°.

In the interest of deconvolving the effects of molecular orientation, charge transfer, and electromagnetic fields, experimental PiFM spectra of Au-BDT is compared to DFT calculated IR spectra of an uncoordinated BDT molecule simulated in vacuum in Fig. 3.3a and Au_{20}-BDT in Fig. 3.3b with insets showing relaxed geometries. Varying electric field strengths are applied in the positive or negative z direction, ranging from +0.01 to -0.01 au. With no gold atoms to contribute charge, the orientation of BDT is largely unchanged, with only subtle shifts to molecular structure that are challenging to distinguish by eye in the insets of Fig. 3.3a. Wavenumber shifts are gradual, such as the blue shift of the 1394 cm^{-1} peak at +0.01 au (dark red) to 1428 cm^{-1} at -0.01 au (dark blue). Intensity changes in peak heights are similarly mild, such as the increase in intensity of the SH bending mode at 894 cm^{-1} from +0.01 au to -0.01 au. In contrast, Fig. 3.3b shows PiFM spectra compared to DFT IR spectra of Au_{20}-BDT. Including a larger Au cluster introduces significant charge transfer to the system. Consequently, the effects of applied electric fields on simulated IR spectra are highly non-linear. For example, at -0.01 au a vacancy is created in the Au(111) surface. The mobile Au-BDT complex reorients on the edge of the cluster facet. This causes the spectral intensity to be significantly enhanced, needing to be scaled by a factor of 0.2 for visualization purposes (light blue). At +0.01 au, the spectrum is similarly scaled by 0.5. At this field strength, the BDT molecule reorients to be nearly perpendicular to the surface. Additionally, the thiol group rotates from an in-plane to an out-of-plane bonding orientation. With less steric hindrance, the SH bending mode redshifts to 894 cm^{-1} with a large enhancement compared to every other field strength. These results demonstrate that strong electric fields in concert with charge transfer from conductive surfaces

are capable of driving structural changes such as adatom diffusion, bonding angle, and rotational shifts that can be interpreted spectroscopically with *ab initio* approaches.

IR calculations require fully relaxed ground states for accurate results. Geometries far from energy minima will result in imaginary frequencies that are not physical. Hence, Fig. 3.3c shows single point DFT energy calculations for Au_{20}-BDT with varying bonding angles rather than IR spectra. The minima is found to be at a 30° bonding angle from the Au(111) surface, a reasonable match to experimental findings for structurally similar molecules.[14] The total system energy changes less than 30 meV across all bonding angles, comparable to energy fluctuations at room temperature (where k_BT = 25 meV). Thus, orientational effects, such as the bonding angle of BDT with the Au surface normal, without electric fields or charge transfer are unlikely to have major effects on IR spectra. Finally, Fig. 3.3d shows a top down and side view of BDT on a Au(111) surface as modeled with periodic boundary conditions in VASP. The unit cell is defined as (3 x √3). As observed in STM experiments,[15] Au-BDT forms linear domains, likely via π-π stacking of neighboring benzene rings. The bonding angle in plane-wave geometry relaxations is found to be 29°. This agrees with both the minima identified by single point energy calculations in Fig. 3.3c as well as the best match to experimental PiFM spectra, Au_{20}-BDT with a bonding angle of 25° at +0.005 au.

3.4 Conclusion

In this work, we present first principles approaches to model IR spectra of BDT ligands on nanoparticle surfaces with comparison to experimental PiFM force spectra. The proximity of

the Au PiFM tip to the Au NP surface creates a confined geometry with non-resonant electromagnetic enhancement of optical fields in the junction, enabling localized chemical mapping of BDT on 40 nm Au NP. First principles DFT simulations aid in the identification of oxidation states. The majority of Au-BDT likely contain thiol end groups, with contributions from few but strong sulfoxide resonances. Decomposing IR spectra along Cartesian axes further illuminates the origin of extraneous peaks in Au-BDT thiol oxidation state simulations arising from x-y planar modes that are not detectable by the PiFM cantilever. Approaches developed here will greatly aid in interpretation of PiFM spectra with nanoscale inhomogeneities, i.e. facets and mobile Au atoms on a NP surface that complicate direct comparison to ensemble FTIR spectral measurements. DFT simulations further illuminate fundamental contributions to spectra from charge transfer compared to applied electric fields. Orientation effects alone are not found to be energetically significant and hence unlikely to affect spectra. Without the gold surface to provide delocalized electrons, there is negligible charge transfer, resulting in gradual peak intensity and wavenumber shifts due to applied electric fields. Including the gold surface results in significant charge transfer driven by electric fields that lead to a multitude of non linear effects, including reorientation of Au-BDT bonding angles, coercing diffusion of surface Au atoms, and rotation of functional groups, all of which are reflected in large intensity enhancements and peak shifts that can be interpreted by simulation. These results demonstrate the capability of PiFM and DFT to illuminate detailed chemical behavior on the nanoscale, encouraging further understanding of light matter interactions relevant to optoelectronics, biosensing, and photocatalysis.

3.5 References

(1) Eppenberger, M.; Messner, A.; Bitachon, B. I.; Heni, W.; Blatter, T.; Habegger, P.; Destraz, M.; De Leo, E.; Meier, N.; Del Medico, N.; Hoessbacher, C.; Baeuerle, B.; Leuthold, J. Resonant Plasmonic Micro-Racetrack Modulators with High Bandwidth and High Temperature Tolerance. *Nat. Photonics* **2023**, 1–8. https://doi.org/10.1038/s41566-023-01161-9.

(2) Hu, H.; Weber, T.; Bienek, O.; Wester, A.; Hüttenhofer, L.; Sharp, I. D.; Maier, S. A.; Tittl, A.; Cortés, E. Catalytic Metasurfaces Empowered by Bound States in the Continuum. *ACS Nano* **2022**, *16* (8), 13057–13068. https://doi.org/10.1021/acsnano.2c05680.

(3) Kim, M.; Lin, M.; Son, J.; Xu, H.; Nam, J.-M. Hot-Electron-Mediated Photochemical Reactions: Principles, Recent Advances, and Challenges. *Adv. Opt. Mater.* **2017**, *5* (15), 1700004. https://doi.org/10.1002/adom.201700004.

(4) Thrift, W. J.; Nguyen, C. Q.; Darvishzadeh-Varcheie, M.; Zare, S.; Sharac, N.; Sanderson, R. N.; Dupper, T. J.; Hochbaum, A. I.; Capolino, F.; Abdolhosseini Qomi, M. J.; Ragan, R. Driving Chemical Reactions in Plasmonic Nanogaps with Electrohydrodynamic Flow. *ACS Nano* **2017**, *11* (11), 11317–11329. https://doi.org/10.1021/acsnano.7b05815.

(5) Thrift, W. J.; Ragan, R. Quantification of Analyte Concentration in the Single Molecule Regime Using Convolutional Neural Networks. *Anal. Chem.* **2019**, *91* (21), 13337–13342. https://doi.org/10.1021/acs.analchem.9b03599.

(6) Esteban, R.; Borisov, A. G.; Nordlander, P.; Aizpurua, J. Bridging Quantum and Classical Plasmonics with a Quantum-Corrected Model. *Nat. Commun.* **2012**, *3* (1), 825. https://doi.org/10.1038/ncomms1806.

(7) Schmid, T.; Opilik, L.; Blum, C.; Zenobi, R. Nanoscale Chemical Imaging Using Tip-Enhanced Raman Spectroscopy: A Critical Review. *Angew. Chem. Int. Ed.* **2013**, *52* (23), 5940–5954. https://doi.org/10.1002/anie.201203849.

(8) Nowak, D.; Morrison, W.; Wickramasinghe, H. K.; Jahng, J.; Potma, E.; Wan, L.; Ruiz, R.; Albrecht, T. R.; Schmidt, K.; Frommer, J.; Sanders, D. P.; Park, S. Nanoscale Chemical Imaging by Photoinduced Force Microscopy. *Sci. Adv.* **2016**, *2* (3), e1501571. https://doi.org/10.1126/sciadv.1501571.

(9) Almajhadi, M. A.; Uddin, S. M. A.; Wickramasinghe, H. K. Observation of Nanoscale Opto-Mechanical Molecular Damping as the Origin of Spectroscopic Contrast in Photo Induced Force Microscopy. *Nat. Commun.* **2020**, *11* (1), 5691. https://doi.org/10.1038/s41467-020-19067-3.

(10) Li, J.; Jahng, J.; Pang, J.; Morrison, W.; Li, J.; Lee, E. S.; Xu, J.-J.; Chen, H.-Y.; Xia, X.-H. Tip-Enhanced Infrared Imaging with Sub-10 Nm Resolution and Hypersensitivity. *J. Phys. Chem. Lett.* **2020**, *11* (5), 1697–1701. https://doi.org/10.1021/acs.jpclett.0c00129.

(11) Yoo, D.; de León-Pérez, F.; Pelton, M.; Lee, I.-H.; Mohr, D. A.; Raschke, M. B.; Caldwell, J. D.; Martín-Moreno, L.; Oh, S.-H. Ultrastrong Plasmon–Phonon Coupling via Epsilon-near-Zero Nanocavities. *Nat. Photonics* **2021**, *15* (2), 125–130. https://doi.org/10.1038/s41566-020-00731-5.

(12) Roth, R. M.; Panoiu, N. C.; Adams, M. M.; Osgood, R. M.; Neacsu, C. C.; Raschke, M. B. Resonant-Plasmon Field Enhancement from Asymmetrically Illuminated Conical Metallic-Probe Tips. *Opt. Express* **2006**, *14* (7), 2921–2931. https://doi.org/10.1364/OE.14.002921.

(13) Chauvin, J.-P. R.; Pratt, D. A. On the Reactions of Thiols, Sulfenic Acids, and Sulfinic Acids with Hydrogen Peroxide. *Angew. Chem. Int. Ed.* **2017**, *56* (22), 6255–6259. https://doi.org/10.1002/anie.201610402.

(14) Tour, J. M.; Jones, L. I.; Pearson, D. L.; Lamba, J. J. S.; Burgin, T. P.; Whitesides, G. M.; Allara, D. L.; Parikh, A. N.; Atre, S. Self-Assembled Monolayers and Multilayers of Conjugated Thiols, .Alpha.,.Omega.-Dithiols, and Thioacetyl-Containing Adsorbates. Understanding Attachments between Potential Molecular Wires and Gold Surfaces. *J. Am. Chem. Soc.* **1995**, *117* (37), 9529–9534. https://doi.org/10.1021/ja00142a021.

(15) Stammer, X.; Tonigold, K.; Bashir, A.; Käfer, D.; Shekhah, O.; Hülsbusch, C.; Kind, M.; Groß, A.; Wöll, C. A Highly Ordered, Aromatic Bidentate Self-Assembled Monolayer on Au(111): A Combined Experimental and Theoretical Study. *Phys. Chem. Chem. Phys.* **2010**, *12* (24), 6445–6454. https://doi.org/10.1039/C002215M.

(16) Wang, X.; Shindel, M. M.; Wang, S.-W.; Ragan, R. A Facile Approach for Assembling Lipid Bilayer Membranes on Template-Stripped Gold. *Langmuir* **2010**, *26* (23), 18239–18245. https://doi.org/10.1021/la102774n.

(17) M. J. Frisch, G. W. Trucks, H. B. Schlegel, G. E. Scuseria, M. A. Robb, J. R. Cheeseman, G. Scalmani, V. Barone, G. A. Petersson, H. Nakatsuji, X. Li, M. Caricato, A. V. Marenich, J. Bloino, B. G. Janesko, R. Gomperts, B. Mennucci, H. P. Hratchian, J. V. Ortiz, A. F. Izmaylov, J. L. Sonnenberg, D. Williams-Young, F. Ding, F. Lipparini, F. Egidi, J. Goings, B. Peng, A. Petrone, T. Henderson, D. Ranasinghe, V. G. Zakrzewski, J. Gao, N. Rega, G. Zheng, W. Liang, M. Hada, M. Ehara, K. Toyota, R. Fukuda, J. Hasegawa, M. Ishida, T. Nakajima, Y. Honda, O. Kitao, H. Nakai, T. Vreven, K. Throssell, J. A. Montgomery, Jr., J. E. Peralta, F. Ogliaro, M. J. Bearpark, J. J. Heyd, E. N. Brothers, K. N. Kudin, V. N. Staroverov, T. A. Keith, R. Kobayashi, J. Normand, K. Raghavachari, A. P. Rendell, J. C. Burant, S. S. Iyengar, J. Tomasi, M. Cossi, J. M. Millam, M. Klene, C. Adamo, R. Cammi, J. W. Ochterski, R. L. Martin, K. Morokuma, O. Farkas, J. B. Foresman, D. J. Fox. Gaussian 16, 2016.

(18) Kresse, G.; Furthmüller, J. Efficiency of Ab-Initio Total Energy Calculations for Metals and Semiconductors Using a Plane-Wave Basis Set. *Comput. Mater. Sci.* **1996**, *6* (1), 15–50. https://doi.org/10.1016/0927-0256(96)00008-0.

(19) Kresse, G.; Furthmüller, J. Efficient Iterative Schemes for Ab Initio Total-Energy Calculations Using a Plane-Wave Basis Set. *Phys. Rev. B* **1996**, *54* (16), 11169–11186. https://doi.org/10.1103/PhysRevB.54.11169.

(20) Perdew, J. P.; Burke, K.; Wang, Y. Generalized Gradient Approximation for the Exchange-Correlation Hole of a Many-Electron System. *Phys. Rev. B* **1996**, *54* (23), 16533–16539. https://doi.org/10.1103/PhysRevB.54.16533.

(21) Hay, P. J.; Wadt, W. R. Ab Initio Effective Core Potentials for Molecular Calculations. Potentials for the Transition Metal Atoms Sc to Hg. *J. Chem. Phys.* **1985**, *82* (1), 270–283. https://doi.org/10.1063/1.448799.

(22) Merlen, A.; Chaigneau, M.; Coussan, S. Vibrational Modes of Aminothiophenol: A TERS and DFT Study. *Phys. Chem. Chem. Phys.* **2015**, *17* (29), 19134–19138. https://doi.org/10.1039/C5CP01579K.

(23) Sun, M.; Huang, Y.; Xia, L.; Chen, X.; Xu, H. The PH-Controlled Plasmon-Assisted Surface Photocatalysis Reaction of 4-Aminothiophenol to p,P′-Dimercaptoazobenzene on Au, Ag, and Cu Colloids. *J. Phys. Chem. C* **2011**, *115* (19), 9629–9636. https://doi.org/10.1021/jp201002v.

(24) Grimme, S. Semiempirical GGA-type density functional constructed with a long-range dispersion correction. *J. Comput. Chem.* **2006**, *27* (15), 1787–1799. https://doi.org/10.1002/jcc.20495.

(25) Monkhorst, H. J.; Pack, J. D. Special Points for Brillouin-Zone Integrations. *Phys. Rev. B* **1976**, *13* (12), 5188–5192. https://doi.org/10.1103/PhysRevB.13.5188.

(26) Gajdoš, M.; Hummer, K.; Kresse, G.; Furthmüller, J.; Bechstedt, F. Linear Optical Properties in the Projector-Augmented Wave Methodology. *Phys. Rev. B* **2006**, *73* (4), 045112. https://doi.org/10.1103/PhysRevB.73.045112.

(27) Vasp_raman.Py, 2022. https://github.com/raman-sc/VASP (accessed 2022-12-15).

CONCLUSION

Through density functional theory simulations, we surveyed the single atom stability of a range of earth abundant transition metals that span the 3, 4, and 5d rows of the periodic table and found that all four were resistant to aggregation on two types of graphene surface defects. By calculating the activation energy barriers of carbon monoxide oxidation reactions on these single atoms, we found that spin unambiguously contributes to enhanced catalytic activity in at least one case, tantalum coordinated to one pyridinic N functional group. By expanding the number of pyridinic N-dopants and calculating activation energy barriers for a simpler chemical process (dissociation of O_2), we will clearly identify the role of spin on catalytic performance of pyridinic N-doped graphene surface defects. We expect that the parity of the pyridinic N atoms coordinated to the defect, which is seldom discussed in the literature, will strongly affect the spin behavior and is a likely source of some conflicting results regarding the catalytic activity of pyridinic N dopants. Additionally, it is already known that the approximate distance between defects as well as surface coverage heavily affects magnetic behavior and could be another contributor to conflicting results. This work will also extend the range of appropriate transition metal atoms for SAC and motivate additional experimental work to further tailor the spin properties of carbonaceous materials for SAC that can exceed the performance of platinum. We have demonstrated first principles methods for discerning molecular orientation from vibrational spectra, including Cartesian decomposition of spectra, identifying the presence of chemical crosslinking and molecular reorientation in near field optical cavities with intense electromagnetic fields. Our contributions will further the understanding of energy transfer between molecules in plasmonic nanogaps and non-

resonant confined geometries, of great interest to fields as broad as photocatalysis, optoelectronics, and nonlinear optics. By mapping the local electromagnetic fields of plasmonic nanogaps and non-resonant tip-sample junctions and how they are perturbed by different molecular crosslinkers will contribute to fundamental understanding of molecular orientation, geometry, and charge transfer on vibrational spectra. We anticipate incorporating findings to further enhance multiplexing performance of our SERS biosensors in complex biological samples.